

On the response of tidal rivers to deepening and narrowing

Risks for a regime shift towards hyper-turbid conditions.

J.C. Winterwerp

March 2013

DISCLAIMER:

This is the report as it was delivered in January 2013 to the clients. After discussions on all the results of the research program 'LTV Safety and Accessibility' with various stakeholders in the Flemish-Dutch Scheldt Committee a final version of the report is made

Table of contents

1. Introduction
2. Tidal evolution in a converging estuary with intertidal area
 - 2.1 Derivation of the relevant equations
 - 2.2 The response of an estuary to deepening and narrowing
3. Fine sediment transport in narrow estuaries
 - 3.1 Transport components
 - 3.2 Reduction in effective hydraulic drag
 - 3,3 Hyper-concentrated conditions
 - 3,4 A qualitative description of the regime shift in the Ems estuary
4. Comparison of various estuaries
 - 4.1 The Ems River
 - 4.2 The Loire River
 - 4.3 The Elbe River
 - 4,4 The Weser Estuary
 - 4.5 The Upper Sea Scheldt
5. Summary and conclusions
6. Recommendations
 - Acknowledgments
 - References
 - Notation

1. Introduction

Fig. 1.1 depicts the evolution of the tidal range over roughly the last century in five European ports, which are all situated more than 50 km from the mouth of fairly small and narrow estuaries. It is generally accepted that this large tidal amplification is caused by the ongoing deepening and canalization of these rivers, accommodating ever-larger ships; though the precise mechanisms behind are not yet understood. Of course, the increases in high water levels, and decreases in low water levels form serious problems by themselves, e.g. enhanced flood levels, salinity intrusion, and lowering of ground water table. However, it becomes more and more evident that such deepening and narrowing induce large environmental problems as well. Infamous are the Ems (Germany) and Loire (France) Rivers. Today, both rivers can be characterized as hyper-turbid, with suspended sediment (SPM) concentrations of several 10 g/l, and large-scale occurrences of fluid mud. Strong vertical stratification causes serious water quality problems, and in the Loire the enhanced salinity intrusion yields problems with fresh water intake for industry and agriculture. The causes of the evolution of Loire and Ems to these hyper-turbid states are not yet fully understood (Talke et al, 2008 & 2009; Chernetsky, 2010; Winterwerp, 2011), though there is consensus that the large amplification of the tidal range must have played an important role.

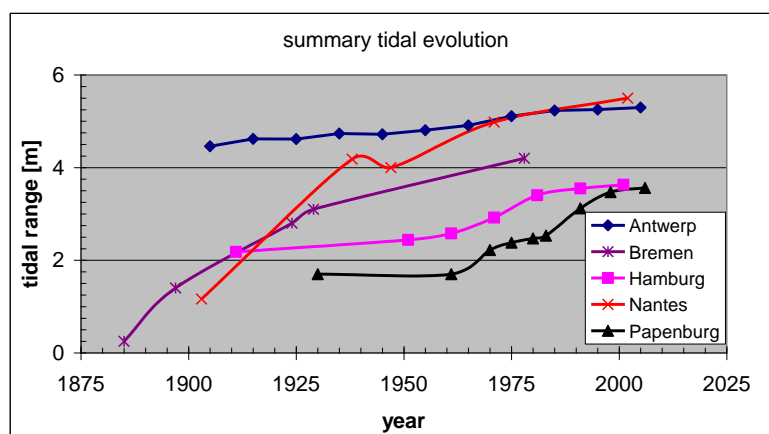


Fig. 1.1: Tidal evolution in five European ports (Antwerp along Scheldt, Belgium; Bremen along Weser, Germany; Hamburg along Elbe, Germany; Nantes along Loire, France; and Papenburg along Ems, Germany).

Also the Scheldt-estuary is renowned for its long lasting human interventions, such as deepening, narrowing by embankments (land reclamations, and loss of intertidal area), sand mining and large-scale sediment displacements by dredging and dumping. As authorities fear an evolution such as in the Ems and Loire Rivers, the Flemish Department of Maritime Access initiated the current study, which is carried out in the framework of a larger research program on the Scheldt estuary.

This study is based on a comparison of the analysis of historical tidal data of four rivers, e.g. Elbe, Ems, Loire and Scheldt. This analysis is carried out with a simple analytical model, which describes the solution of the linearized shallow water movement equations. The derivation of this model is presented in Chapter 2, together with a conceptual analysis of the response of a tidal river to deepening and narrowing (loss of intertidal area). Chapter 3 describes the interaction of fine suspended sediment with the turbulent water movement, which may result in a considerable reduction in effective hydraulic drag. Also we introduce the conditions which may lead to a secondary turbidity maximum, and arguments that hyper-turbid conditions are favorable from an

energetic point of view. The actual analysis of the historical tidal data is carried out in Chapter 4, where we establish the evolution of the tidal damping in the rivers as a function of changes in the river's geometry and bathymetry, discussing the role of tidal reflection and reductions in effective hydraulic drag. The results of the individual rivers are compared in Chapter 5, presenting a conceptual diagram on the evolution of a tidal river towards hyper-turbid conditions in response to human interventions.

2. Tidal evolution in a converging estuary with intertidal area

2.1 Derivation of the relevant equations

the equations

In this section, we derive the dispersion equation for tidal propagation in a converging estuary with a compound cross section, e.g. Fig. 2.1.

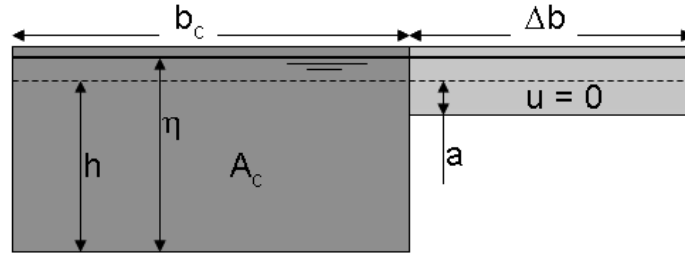


Fig. 2.1: Compound channel and definitions.

We follow Friedrichs (2010) and Dronkers (2005), but make no a priori assumptions on the contribution of the various terms in the equations, except for a linearization of the friction term, and we neglect the advection term in the momentum equation:

$$(b_c + \Delta b) \frac{\partial \eta}{\partial t} + \frac{\partial A_c u}{\partial x} = 0 \quad (1)$$

$$\frac{\partial u}{\partial t} + g \frac{\partial \eta}{\partial x} + \frac{ru}{h} = 0$$

We refer to Dronkers (1964) for a complete analysis of these equations in a straight channel. Here we focus on a converging estuary, as almost all natural, alluvial estuaries are characterized by a so-called trumpet shaped plan form (e.g. Prandle, 2004). If we assume $A_c \approx hb_c$, equ. (1) can be re-written as:

$$\frac{\partial \eta}{\partial t} + \frac{A_c}{b_c + \Delta b} \frac{\partial u}{\partial x} + \left[\frac{1}{b_c} \frac{\partial b_c}{\partial x} + \frac{1}{h} \frac{\partial h}{\partial x} \right] \frac{A_c}{b_c + \Delta b} u = 0 \quad (2a)$$

$$\frac{\partial u}{\partial t} + g \frac{\partial \eta}{\partial x} + \frac{ru}{h} = 0 \quad (2b)$$

where η = instantaneous water level, u = cross-sectionally averaged flow velocity, h = tidal-mean water depth, b_c = width flow-carrying cross section, Δb = width intertidal area (over which the flow velocity is zero), A_c = surface area flow-carrying cross section ($A_c \approx hb_c$), assuming $\eta \ll h$, r = linear friction term $r = 8c_D U / 3\pi$ [m/s], c_D = drag coefficient, U = characteristic (maximal) velocity, and x and t are longitudinal co-ordinate and time ($x = 0$ at the estuaries mouth, and $x > 0$ up-estuary). We focus on exponentially converging estuaries, e.g. $b_c = b_0 \exp\{-x/L_b\}$, where b_0 = width flow-carrying cross section in the mouth of the estuary

and L_b = convergence length (typical values between ~20 and ~40 km). The drag coefficient c_D attains values of 0.001 to 0.003 m/s (corresponding Chézy values of 100 – 60 $\text{m}^{1/2}/\text{s}$, as $r \approx gU/C^2$), hence r also varies from around 0.001 to 0.003. In the following, we assume that the river flow is so small that its effects can be neglected. Finally, further to our linear approach, we also assume that parameters may vary along the estuary, such as the tidal amplitude, but that these variations are relatively small, and that the tidal amplitude is small compared to the water depth.

If we neglect longitudinal gradients in tidal-mean water depth ($\partial h/\partial x$), the continuity and mass balance equation read¹⁾:

$$\frac{\partial \eta}{\partial t} + \frac{A_c}{b_c + \Delta b} \frac{\partial u}{\partial x} - \frac{A_c}{b_c + \Delta b} \frac{u}{L_b} = 0 \quad (3a)$$

$$\frac{\partial u}{\partial t} + g \frac{\partial \eta}{\partial x} + \frac{ru}{h} = 0 \quad (3b)$$

the dispersion relation and wave numbers

We assume that the solution to (3) follows a harmonic function:

$$\eta(x, t) = h + a_0 \exp\{i(\omega t - kx)\} \quad \text{and} \quad u(x, t) = U_0 \exp\{i(\omega t - kx - \phi)\} \quad (4a)$$

where a_0 = tidal amplitude at $x = 0$, U_0 = amplitude flow velocity at $x = 0$, ω = tidal frequency; $\omega = 2\pi/T$; T = tidal period, k = complex wave number; $k = k_r + ik_i$, k_r = real wave number ($k_r = 2\pi/\lambda$), λ = tidal wave length, k_i = imaginary wave number, and ϕ = phase angle between tide and velocity. Note that the three unknowns a_0 , U_0 and ϕ are real. Next, we substitute (4a) into (3a) and (3b):

$$i\omega a_0 - \left(\frac{A_c}{b_c + \Delta b} ik + \frac{A_c}{b_c + \Delta b} \frac{1}{L_b} \right) U_0 \exp\{-i\phi\} = 0 \quad (5a)$$

$$igka_0 - \left(i\omega + \frac{r}{h} \right) U_0 \exp\{-i\phi\} = 0 \quad (5b)$$

From equ. (5b) we can derive the velocity amplitude U_0 as a function of a_0 :

$$U_0 = \text{mod} \left[\frac{igka_0}{(i + r_*) \omega \exp\{-i\phi\}} \right] = \frac{ga_0}{\omega} \sqrt{\frac{k_r^2 + k_i^2}{r_*^2 + 1}} \quad (5c)$$

¹⁾ Note that a more general derivation is obtained by assuming an exponentially converging cross section; however, it is difficult to account for spatially varying water depth. To account for longitudinal variations in water depth as good as possible, the rivers are sub-divided into sub-sections with constant depth in our analyses below (see f.i. Jay, 1991).

equ's (5a) and (5b) can be written in matrix form:

$$\begin{bmatrix} i\omega & -\left(\frac{A_c}{b_c + \Delta b} ik + \frac{A_c}{b_c + \Delta b} \frac{1}{L_b}\right) \exp\{-\phi i\} \\ igk & -\left(i\omega + \frac{r}{h}\right) \exp\{-\phi i\} \end{bmatrix} \begin{bmatrix} a_0 \\ U_0 \end{bmatrix} = 0 \quad (6)$$

Requiring the existence of non-trivial solutions yields a dispersion equation implicit in the wave number k :

$$-i\omega \left(i\omega + \frac{r}{h}\right) + igk \left(\frac{A_c}{b_c + \Delta b} ik + \frac{A_c}{b_c + \Delta b} \frac{1}{L_b}\right) = 0 \quad \text{or } \kappa^2 - 2i\kappa - \Lambda_e (1 - ir_*) = 0 \quad (7)$$

$$L_b k^2 - ik - \frac{b_c + \Delta b}{ghb_c} L_b \omega^2 \left(1 - i \frac{r}{\omega h}\right) = 0$$

in which the following dimensionless parameters have been defined:

$$\begin{aligned} \kappa &= \kappa_r + i\kappa_i = 2(k_r + ik_i) L_b = 2kL_b \\ L_* &= \frac{2L_b \omega}{\sqrt{gh}} = \frac{2L_b}{L_g}, \quad \text{where } L_g \equiv \frac{\sqrt{gh}}{\omega} \\ r_* &= \frac{r}{\omega h} = \frac{gU}{\omega h C^2} \\ b_* &= \frac{b_c + \Delta b}{b_c} \\ \Lambda_e &= b_* L_*^2 = \frac{b_c + \Delta b}{b_c} \frac{4L_b^2 \omega^2}{gh} = \frac{4L_b^2 \omega^2}{gA_c / b_{tot}} \end{aligned} \quad (8)$$

Here we introduce the estuarine convergence number Λ_e , through which all geometrical and bathymetrical features of the rivers are accounted for. Note that Λ_e decreases with increasing water depth, increasing convergence of the river's plan form, and decreasing intertidal area. Next, from (7) k is resolved:

$$k_{1,2} = i \frac{1 \pm \sqrt{1 - 4 \frac{b_c + \Delta b}{gA_c} L_b^2 \omega^2 + 4 \frac{b_c + \Delta b}{gA_c} L_b^2 i \omega \frac{r}{h}}}{2L_b} = i \frac{1 \pm \sqrt{1 - \Lambda_e + i\Lambda_e r_*}}{2L_b} \quad (9)$$

Using MAPLE, the real and imaginary part of (9) are determined:

$$k_r = \pm \frac{1}{4L_b} \left[2\sqrt{\left(4(1+\Delta b/b_c)\frac{L_b^2\omega^2}{gh} - 1\right)^2 + \left(4(1+\Delta b/b_c)\frac{L_b^2\omega^2}{gh}\right)^2 \left(\frac{r}{\omega h}\right)^2} + 2\left|4(1+\Delta b/b_c)\frac{L_b^2\omega^2}{gh} - 1\right| \right]^{1/2} \quad (10a)$$

$$k_i = \frac{1}{2L_b} \mp \frac{1}{4L_b} \left[2\sqrt{\left(4(1+\Delta b/b_c)\frac{L_b^2\omega^2}{gh} - 1\right)^2 + \left(4(1+\Delta b/b_c)\frac{L_b^2\omega^2}{gh}\right)^2 \left(\frac{r}{\omega h}\right)^2} - 2\left|4(1+\Delta b/b_c)\frac{L_b^2\omega^2}{gh} - 1\right| \right]^{1/2} \quad (10b)$$

The positive and negative real wave numbers represent the up-estuary propagating tidal wave, and its reflection, if any. We note that the imaginary wave number for the up-estuary propagating wave differs from its reflection, which is to be attributed to the funnel shape of the estuary. This explains why κ_i^- is always positive, i.e. the reflected tidal wave is always damped. Indeed, when $L_b = \infty$, as in the case of a straight, prismatic channel, all wave numbers become symmetric again.

For a non-converging ($L_b = \infty$), frictionless channel ($r = 0$), equ. (10) converges to the well-known relations $k_r = \omega\sqrt{(b_c + \Delta b)/b_c gh}$ and $k_i = 0$. For a non-converging channel with friction, we obtain:

$$k_r = \pm \sqrt{\frac{b_*\omega^2}{2gh}} \left[\sqrt{1+r_*^2} + 1 \right]^{1/2} \quad \text{and} \quad k_i = \mp \sqrt{\frac{b_*\omega^2}{2gh}} \left[\sqrt{1+r_*^2} - 1 \right]^{1/2} \quad (10c)$$

In dimensionless form, the wave numbers (10) for the up-estuary propagating wave, and its reflection, represented by the superscripts \blacksquare^+ and \blacksquare^- , respectively, read:

$$\kappa_r^+ = \frac{1}{2} \left[2\sqrt{(\Lambda_e - 1)^2 + (\Lambda_e r_*)^2} + 2|\Lambda_e - 1| \right]^{1/2} \quad \text{and} \quad (11a)$$

$$\kappa_r^- = -\frac{1}{2} \left[2\sqrt{(\Lambda_e - 1)^2 + (\Lambda_e r_*)^2} + 2|\Lambda_e - 1| \right]^{1/2}$$

$$\kappa_i^+ = 1 - \frac{1}{2} \left[2\sqrt{(\Lambda_e - 1)^2 + (\Lambda_e r_*)^2} - 2|\Lambda_e - 1| \right]^{1/2} \quad \text{and} \quad (11b)$$

$$\kappa_i^- = 1 + \frac{1}{2} \left[2\sqrt{(\Lambda_e - 1)^2 + (\Lambda_e r_*)^2} - 2|\Lambda_e - 1| \right]^{1/2}$$

In the remainder, we will work with both the dimensionless and non-dimensionless equations. However, we will use the dimensionless parameters of equ. (8) comparing the various estuaries in Section 4 of this report.

limiting values of the wave numbers

Let us analyze these solutions for a converging estuary with a rough, frictionally-dominated bed ($r = \infty$) and for an estuary with a very smooth bed, formed by fluid mud ($r \approx 0$). In the first case the friction term dominates the expression below the square root-sign, in the second case, friction can be neglected. The real and imaginary wave number for a frictionless system read (assuming shallow water, i.e. h not too large)

$$\kappa_r|_{r \downarrow 0} = \sqrt{|\Lambda_e - 1|} \quad \text{and} \quad \kappa_i|_{r \downarrow 0} = 1 \quad (12a)$$

Equ. (12) shows that for a smooth bed, the tidal wave is amplified with the convergence length L_b ; this is therefore the maximum amplification of the tide according to linear theory. In case of a rough bed ($r = \infty$), the real and imaginary wave number become:

$$k_r|_{r \uparrow \infty} = \frac{1}{4L_b} \sqrt{2\Lambda_e r_*} \quad \text{or} \quad \kappa_r|_{r \uparrow \infty} = \sqrt{\Lambda_e r_*}/2 \quad (12b)$$

$$k_i|_{r \uparrow \infty} = -\frac{1}{4L_b} \sqrt{2\Lambda_e r_*} \quad \text{or} \quad \kappa_i|_{r \uparrow \infty} = -\sqrt{\Lambda_e r_*}/2$$

The phase angle between tidal elevation and velocity follows from substitution of (4a) into (3a), elaborating the real part only:

$$i\omega a_0 - i \frac{A_c}{b_c + \Delta b} k U_0 \exp\{-i\phi\} - \frac{A_c}{b_c + \Delta b} \frac{1}{L_b} U_0 \exp\{-i\phi\} = 0 \quad (5a)$$

$$\tan\{\phi\} = \frac{L_b k_i - 1}{L_b k_r} = \frac{\kappa_i - 2}{\kappa_r} \quad (13a)$$

Substituting from (12) yields the phase angle for a smooth and friction dominated system:

$$\tan\{\phi\}|_{r \downarrow 0} = -\frac{1}{\sqrt{|\Lambda_e - 1|}} \quad \text{and} \quad \tan\{\phi\}|_{r \uparrow \infty} = -\frac{\sqrt{\Lambda_e r_*} + 8}{\sqrt{\Lambda_e r_*}} \approx -1 \quad (13b)$$

The celerity c of the tidal wave into the estuary is given by:

$$c = \frac{\omega}{k_r} = \frac{2\omega L_b}{\kappa_r} \quad (14a)$$

Substituting from (12) yields the celerity for a smooth and friction dominated system:

$$c|_{r \downarrow 0} = \frac{2\omega L_b}{\sqrt{|\Lambda_e - 1|}} \quad \text{and} \quad c|_{r \uparrow \infty} = \frac{8\omega L_b}{\sqrt{\Lambda_e r_*}} \quad (14b)$$

the general solution

Next, we study the propagation and amplification/damping of the tide in an infinitely long estuary and/or an estuary of finite length ℓ (for instance by a weir at $x = \ell$). In dimensionless form, the length of the estuary then measures $\lambda_r = \ell/2L_b$. At the mouth of the estuary we prescribe a simple cosine tide:

$$\eta(0, t) = h + a_0 \cos\{\omega t\} \quad (15)$$

in which a_0 = amplitude of the tide. Next, we introduce its complex equivalent $\tilde{\eta}(x, t)$ and require that $\text{Re}\{\tilde{\eta}(0, t)\} = a_0$. The harmonic solution to equ. (3) then reads:

$$\begin{aligned} \tilde{\eta}(x, t) &= h + a_0^+ \exp\{i(\omega t - k^+ x)\} + a_0^- \exp\{i(\omega t - k^- x)\} \quad \text{and} \\ \tilde{u}(x, t) &= U_0^+ \exp\{i(\omega t - k^+ x - \phi)\} + U_0^- \exp\{i(\omega t - k^- x - \phi)\} \end{aligned} \quad (16a)$$

in which a^+ and a^- are the amplitudes of the incoming and reflecting tidal wave. In case of an infinitely long river, equ. (16a) reduces to:

$$\begin{aligned} \tilde{\eta}(x, t) &= h + a_0 \exp\{i(\omega t - kx)\} \quad \text{and} \\ \tilde{u}(x, t) &= U_0 \exp\{i(\omega t - kx - \phi)\} \end{aligned} \quad (16b)$$

as in equ. (4a). The boundary conditions to the solution of equ.'s (3) and (16a) are given by:

- $x = 0$: $a_0^+ + a_0^- = a_0$,
- $x = \ell$: $U = 0$, hence $U^+ = -U^-$.

Further to equ. (3b), the latter implies that

- $x = \ell$: $\partial a^+ / \partial x = -\partial a^- / \partial x$, so that $a_0^+ k^+ \exp\{-ik^+ \ell\} + a_0^- k^- \exp\{-ik^- \ell\} = 0$.

Hence, we find for the two amplitudes a_0^+ and a_0^- from the modulus of a_0 :

$$a_0^+ = \frac{k^- \exp\{-ik^- \ell\}}{k^- \exp\{-ik^- \ell\} - k^+ \exp\{-ik^+ \ell\}} a_0; \quad a^+ = \frac{k^- \exp\{-ik^- \ell\} \exp\{-ik^+ x\}}{k^- \exp\{-ik^- \ell\} - k^+ \exp\{-ik^+ \ell\}} a_0 \quad (17a)$$

$$a_0^- = \frac{k^+ \exp\{-ik^+ \ell\}}{k^+ \exp\{-ik^+ \ell\} - k^- \exp\{-ik^- \ell\}} a_0; \quad a^- = \frac{k^- \exp\{-ik^+ \ell\} \exp\{-ik^- x\}}{k^+ \exp\{-ik^+ \ell\} - k^- \exp\{-ik^- \ell\}} a_0 \quad (17b)$$

resonance of the tidal wave

As $k^- = -k_r + ik_i^- = -k_r + i(p+q)$ and $k^+ = k_r + ik_i^+ = k_r + i(p-q)$, where p and q are dummy variables, we can re-write (17) as:

$$a_0^+ = \frac{k^- \exp\{ik_r \ell\}}{k^- \exp\{ik_r \ell\} - k^+ \exp\{-ik_r \ell\} \exp\{-2q\ell\}} a_0 \quad (18a)$$

$$a_0^- = \frac{k^+ \exp\{-ik_r \ell\} \exp\{-2q\ell\}}{k^+ \exp\{-ik_r \ell\} \exp\{-2q\ell\} - k^- \exp\{ik_r \ell\}} a_0 \quad (18b)$$

Hence, $\lim_{\ell \rightarrow \infty} \{a_0^+\} = a_0$ and $\lim_{\ell \rightarrow \infty} \{a_0^-\} = 0$, retrieving the simple propagating wave in an infinitely long converging estuary. Furthermore, equ. (17) shows that resonance can occur when:

$$\text{Re} \left[k^- \exp\{-ik^- \ell\} - k^+ \exp\{-ik^+ \ell\} \right] = 0 \quad , \text{i.e}$$

$$\tan \left\{ k_r \ell \pm n \frac{\pi}{2} \right\} = - \frac{k_r \exp\{k_i^- \ell\} + k_r \exp\{k_i^+ \ell\}}{k_i^- \exp\{k_i^- \ell\} + k_i^+ \exp\{k_i^+ \ell\}} \quad \text{or} \quad (19a)$$

$$\tan \left\{ \kappa_r \lambda_r \pm n \frac{\pi}{2} \right\} = - \frac{\kappa_r \exp\{\kappa_i^- \lambda_r\} + \kappa_r \exp\{\kappa_i^+ \lambda_r\}}{\kappa_i^- \exp\{\kappa_i^- \lambda_r\} + \kappa_i^+ \exp\{\kappa_i^+ \lambda_r\}}$$

As equ. (19) is implicit in ℓ , we cannot determine the conditions for resonance analytically. However, for a straight channel, $k_i^- = -k_i^+$ (e.g. equ. (11b)), $\tan\{k_r \ell\} = \infty$, which is the case if $\ell = \lambda/4$, where λ = wave length in a straight frictionless channel, e.g. Dronkers (1964). For a very strong converging channel, e.g. $\lim_{L_b \rightarrow 0} k_r = \lim_{L_b \rightarrow 0} k_i^+ = \lim_{L_b \rightarrow 0} k_i^- = 1$, $\tan\{k_r \ell\} = 1$, and $\ell = \lambda/8$. Of course, the wave length in a straight and very converging channel are very much different (in fact if $L_b = 0$, $\lambda = 0$).

The solution to equ. (19) is depicted graphically in Fig. 2.2. Note that typical values for A_e range from 1 to 2 (e.g. Chapter 4).

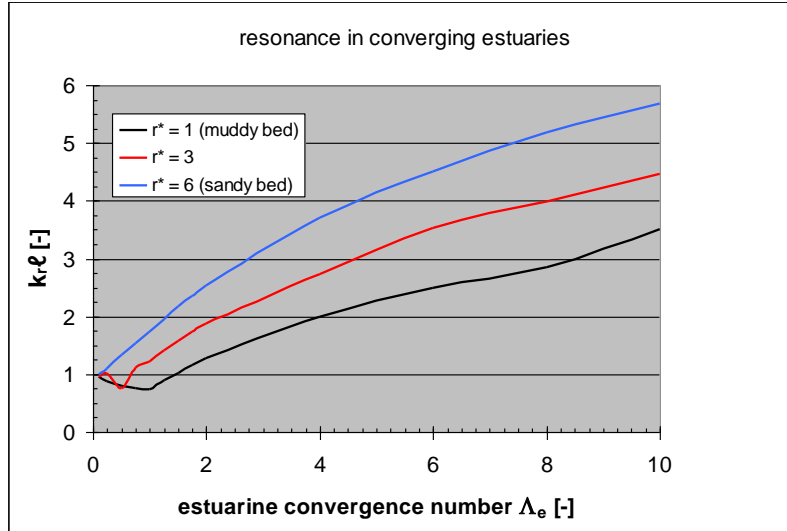


Fig. 2.2: Conditions for resonance (solution of equ. 19) for a converging estuary as a function of the estuarine convergence number.

Note that it is not really possible to re-write equ. (16a), in conjunction with equ. (17) in the form of a single, up-estuary progressing wave with real and imaginary wave numbers k_r and k_i :

$$\tilde{\eta}(x, t) = h + a_0^{\oplus} \exp\left\{i\left(\omega t - \left(k_r^{\oplus} + ik_i^{\oplus}\right)x\right)\right\} \quad (16c)$$

However, it is possible to determine the damping/amplification of the tide through an equivalent imaginary wave number from the ratio of the tidal amplitudes at two locations, using the definition $a_2 = a_1 \exp\{k_i^{\oplus} x\}$, where k_i^{\oplus} is the equivalent imaginary wave number – where relevant however, we have omitted the superscript. We will use this approach in Chapter 4 to establish the effect of reflections in the various estuaries.

tidal asymmetry

Next, we study the dependency of tidal asymmetry on the estuaries' bathymetry. Though we prescribe harmonic solutions (equ.'s (4) and (16) with one frequency only), we can derive a proxy for the internally generated tidal asymmetry by analyzing the celerity of the tidal wave. Further to Friedrichs (2010) and Dronkers (2005) we define an asymmetry parameter $\gamma = c_{HW}/c_{LW}$, where c_{HW} and c_{LW} are the celerity at high water (i.e. $h = h_0 + a$) and low water (i.e. $h = h_0 - a$), respectively:

$$\gamma = \frac{c_{HW}}{c_{LW}} = \frac{k_{r,LW}}{k_{r,HW}} = \left[\frac{\sqrt{(\Gamma_{LW} - 1)^2 + \Gamma_{LW}^2 \left(\frac{r}{\omega h(1-a/h)} \right)^2} + \Gamma_{LW} - 1}{\sqrt{(\Gamma_{HW} - 1)^2 + \Gamma_{HW}^2 \left(\frac{r}{\omega h(1+a/h)} \right)^2} + \Gamma_{HW} - 1} \right]^{1/2} \quad \text{with} \quad (20a)$$

$$\Gamma_{LW} = \frac{4}{gh(1-a/h)} L_b^2 \omega^2 = \frac{L_*^2}{(1-a/h)}$$

$$\Gamma_{HW} = 4 \frac{1 + \Delta b/b_c}{gh(1+a/h)} L_b^2 \omega^2 = \frac{b_* L_*^2}{(1+a/h)}$$

This proxi is relevant for progressive waves, and loses its meaning in case of a fully standing wave. Equ. (20a) can be written in dimensionless form:

$$\gamma = \frac{k_{r,LW}}{k_{r,HW}} = \left[\frac{\left[\frac{(1+a/h)}{(1-a/h)} \right]^{1/2} \left[\sqrt{(L_*^2 - (1-a/h))^2 + \left(\frac{L_*^2 r_*}{(1-a/h)} \right)^2} + L_*^2 - (1-a/h) \right]}{\left[\sqrt{(b_* L_*^2 - (1+a/h))^2 + \left(\frac{b_* L_*^2 r_*}{(1+a/h)} \right)^2} + b_* L_*^2 - (1+a/h) \right]} \right]^{1/2} \quad (20b)$$

Further, for a friction-dominated system we find:

$$\gamma|_{r=\infty} = \frac{k_{r,LW}}{k_{r,HW}} \Big|_{r=\infty} \approx \left[\frac{\frac{1}{(1-a/h)} \frac{1}{(1-a/h)}}{\frac{1 + \Delta b/b_c}{(1+a/h)} \frac{1}{(1+a/h)}} \right]^{1/2} = \frac{1+a/h}{1-a/h} \sqrt{\frac{1}{b_*}} \approx \frac{(1+a/h)^2}{\sqrt{b_*}} \quad (21a)$$

Note that this solution can be derived directly from the general formulation of wave celerity in a straight prismatic compound channel, e.g. $c = \sqrt{gA_c/b_t}$. For a frictionless system we find:

$$\gamma|_{r=0} = \frac{k_{r,LW}}{k_{r,HW}} \Big|_{r=0} = \left[\frac{\Gamma_{LW} - 1}{\Gamma_{HW} - 1} \right]^{1/2} \approx \left[\frac{(1+a/h)^2 \Lambda_e / b_* - (1+a/h)}{\Lambda_e - (1+a/h)} \right]^{1/2} \quad (21b)$$

In the next section, we study the behavior of these solutions graphically, analyzing the response of an estuary to deepening and narrowing (losing intertidal area).

The γ -proxi for tidal asymmetry has been defined for a single up-estuary propagating wave. As long as the effects of reflection are not too large, this proxi is still useful. However, in the asymptotic case of a truly standing wave, the tide is entirely symmetrical, though γ would always be larger than unity.

2.2 The response of an estuary to deepening and narrowing

In this section, we study the behavior of the tidal evolution in a converging estuary graphically. In particular, we analyze the response of the tide to deepening and narrowing of the estuary, where the latter implies reduction/loss of intertidal area. Moreover, we elaborate on the effect of bed friction as one implication of a regime shift towards hyper-concentrated conditions is a dramatic decrease in effective hydraulic drag in the estuary. In the Fig.'s 2.3 and 2.4, we assume a convergence length of $L_b = 25$ km.

First, we evaluate the behavior of the combined solution of equ. (17, e.g. incoming and reflecting wave), as that solution is not easy to interpret owing to its complex character. Fig. 2.3 indeed shows resonant behavior in a straight channel when a weir is placed at a quarter wave length when friction is small. If friction is large enough, damping is predicted. This behavior was presented earlier by e.g. Dronkers (1964) and our results match his results.

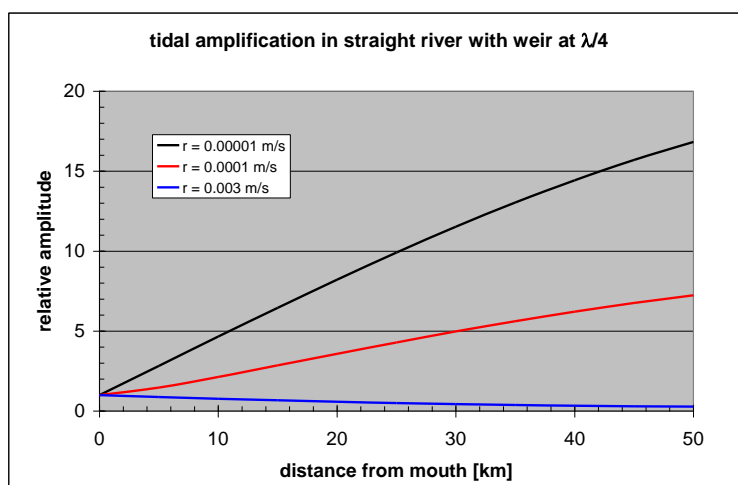


Fig. 2.3: Evolution of tidal wave in 5 m deep, straight estuary ($\lambda = 315$ km) and weir at 79 km; $r = 0.000001$ m/s yields $C \approx 1000$ $m^{1/2}/s$; $r = 0.0001$ m/s yields $C \approx 300$ $m^{1/2}/s$ and $r = 0.003$ yields $C \approx 60$ $m^{1/2}/s$ ($L_b = \infty$).

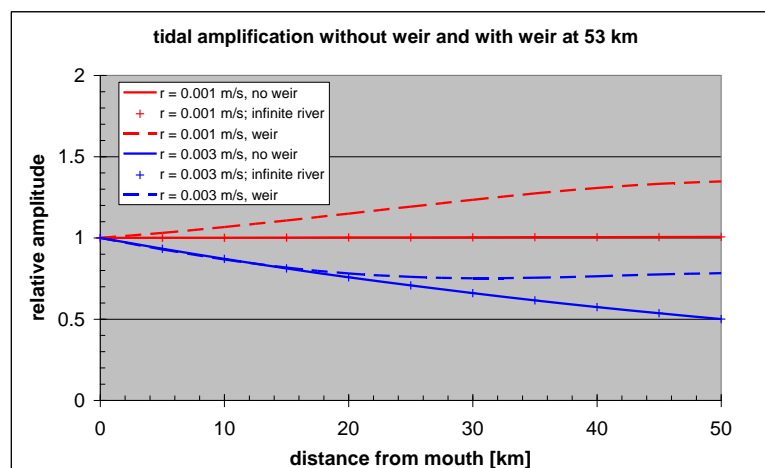


Fig. 2.4: Evolution of tidal wave in short converging estuary ($\ell = 53$ km, $L_b = 33$ km); $r = 0.00001$ m/s yields $C \approx 300$ $m^{1/2}/s$; $r = 0.001$ m/s yields $C \approx 100$ $m^{1/2}/s$; $r = 0.003$ yields $C \approx 60$ $m^{1/2}/s$.

Fig. 2.4 presents computed tidal amplitudes in a 5 m deep converging river ($L_b = 33$ km, e.g. Ems-conditions) with and without a weir for two values of the friction coefficient, the smaller representative for high-concentration conditions and the larger for a sandy bed. We have also plotted the tidal amplitude computed with k_i^+ for an infinitely long estuary, using the definition $a(x) = a_0 \exp\{k_i^+ x\}$ - these results overlap the solution based on equ. (17) exactly. Fig. 2.4 suggests that the impact of reflections on the tidal amplitude increases with decreasing effective hydraulic drag.

Next, we focus on infinitely long estuaries ($\ell = \infty$), and we study the tidal propagation into the estuary. Fig. 2.5 presents the phase difference between the flow velocity and tidal elevation ϕ (e.g. equ. 13a) as a function of depth, width of intertidal area, and bed friction.

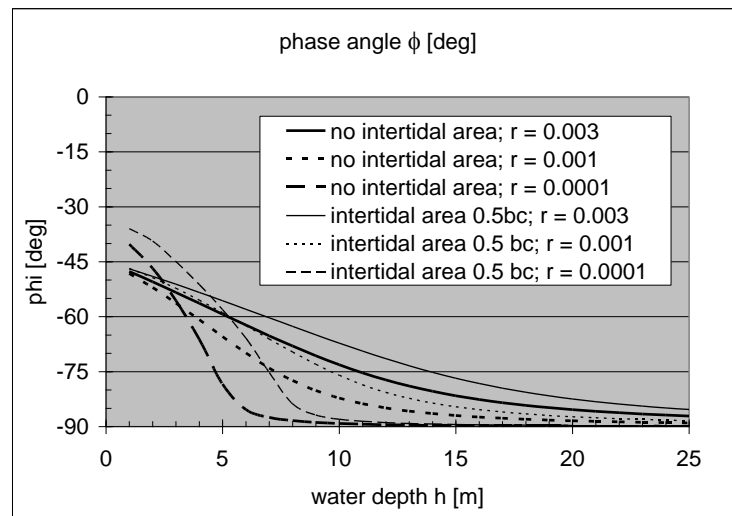


Fig.2.5: Phase angle ϕ between flow velocity and tidal elevation ($\ell = \infty$, $L_b = 33$ km).

Fig. 2.6 presents the celerity c of the tidal wave into the estuary, using equ. (14a). Because of the rapid increase in c with depth h and inverse friction $1/r$, we have used a logarithmic axis.

For $\phi = -90^\circ$ (e.g. Fig. 2.5), high water slack (HWS) occurs at high water (HW), as for standing waves. This condition is met at large water depths, but also at moderate water depths when the hydraulic drag becomes small – the tidal amplification is governed by convergence mainly. The latter is the case for instance in the presence of pronounced layers of fluid mud, as in the Ems and Loire Rivers. However, than the friction length increases, and the effects of reflections become more important. Fig. 2.6 shows that then c increases rapidly, and can become so large that high waters along the estuary occur almost simultaneously. For instance, for $h = 7$ m, and $r = 0.001$, we find $c = 100$ m/s (e.g. Fig. 2.6), and high water at 60 km from the river mouth would occur only 10 minutes after high water at that mouth. Note that a progressive wave approach ($c = \sqrt{gh}$) would yield a travel time of almost 2 hours.

From equ.'s (3a) and (4a) we observe that $\phi = -90^\circ$ occurs when $\partial u / \partial x = 0$ (see also Dronkers, 2005 and Friedrichs, 2010), and from equ. (13a), we conclude that $\phi = -90^\circ$ implies $k_r = \infty$. This explains the rapid increase in c . This also implies large flow velocities over the major part of the estuary. Then, owing to the harmonic solution prescribed (equ. 4a), also the tidal amplitude is

more or less constant over a large part of the estuary. An estuary with such conditions is called synchronous (e.g. Dronkers, 2005). Examples are the current conditions in the Ems and Loire River (e.g. Chapter 4).

Note that the evolution towards a synchronous estuary is delayed in case of (some) intertidal area, e.g. Fig. 2.5. However, the celerity is not too sensitive to the intertidal area, though decreases with $\Delta b/b_c$ (results not shown).

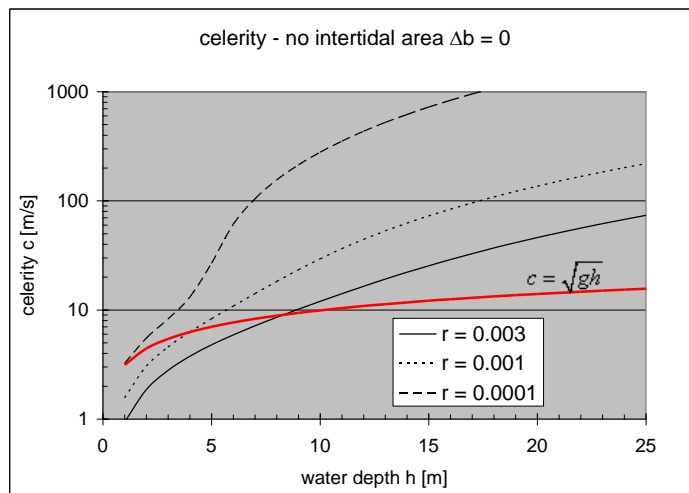


Fig. 2.6: Celerity of tidal wave ($\ell = \infty$, $L_b = 33$ km) with frictionless straight-channel value $c = \sqrt{gh}$ for reference.

At these resonant conditions for low hydraulic drag, amplification of the tide is governed solely by the convergence of the river's plan form (e.g. equ. 11b). This implies a local equilibrium between water movement and bathymetry. At such conditions, we may expect low sensitivity of the water movement to interventions in the river, in particular of interventions up-estuary. This has great implications for mitigating measures in estuaries at resonant conditions.

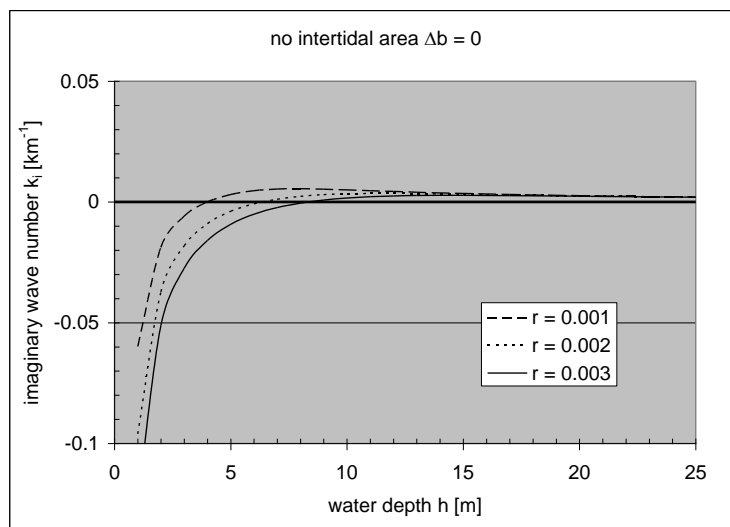


Fig. 2.7: Damping of tidal wave in converging estuary without intertidal area.

Next, we study the amplification of the tide along the estuary; note that $a(x)/a_0 = \exp\{k_i x\}$, e.g. $k_i > 0$ implies amplification of the tide into the estuary. Here we elaborate on the wave numbers directly, whereas in Chapter 5, we will present results in the form of tidal amplitudes facilitating discussion of the results. Fig.'s 2.7, 2.8 and 2.9 show the imaginary wave number as a function of water depth, for three values of the hydraulic roughness (from sandy to muddy conditions) and for three values of the intertidal area. These graphs suggest that a simultaneous deepening and canalization (loss of intertidal area) results in a very sensitive response of the tidal amplitude (e.g. Fig. 2.7). This is in particular the case at low hydraulic drag, which can be explained from the resonant character described above.

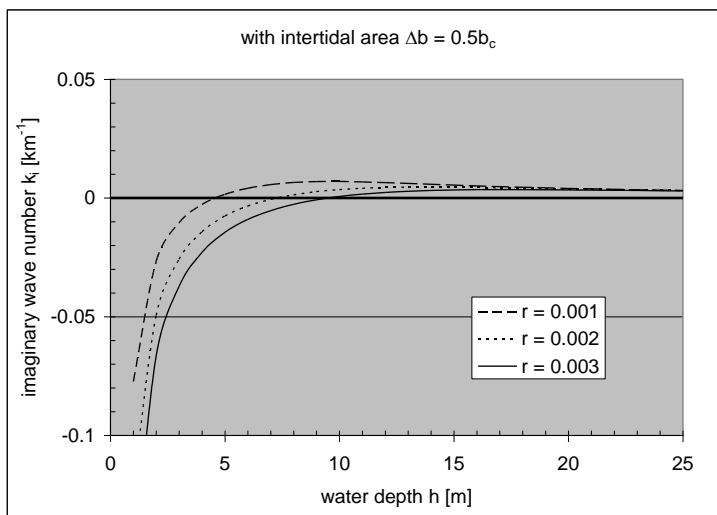


Fig. 2.8: Damping of tidal wave in converging estuary with small intertidal area.

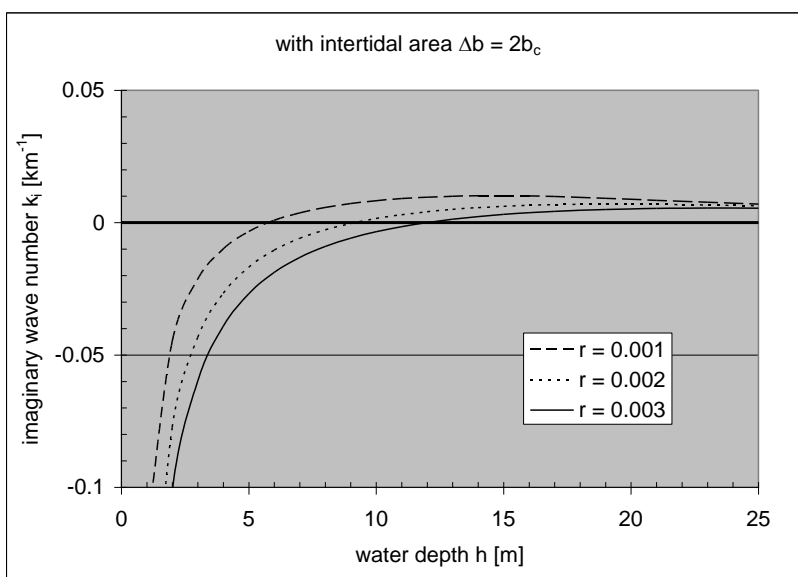


Fig. 2.9: Damping of tidal wave in converging estuary with large intertidal area.

Note that in case of more intertidal area, more water enters the estuary, implying higher water levels, i.e. apparent larger amplification with intertidal area. We conclude that loss of intertidal area has a major effect on the sensitivity of the estuary to further deepening and to a loss in

overall hydraulic drag. One may conclude that the resilience of the estuary to human interferences reduces rapidly with the loss of intertidal area.

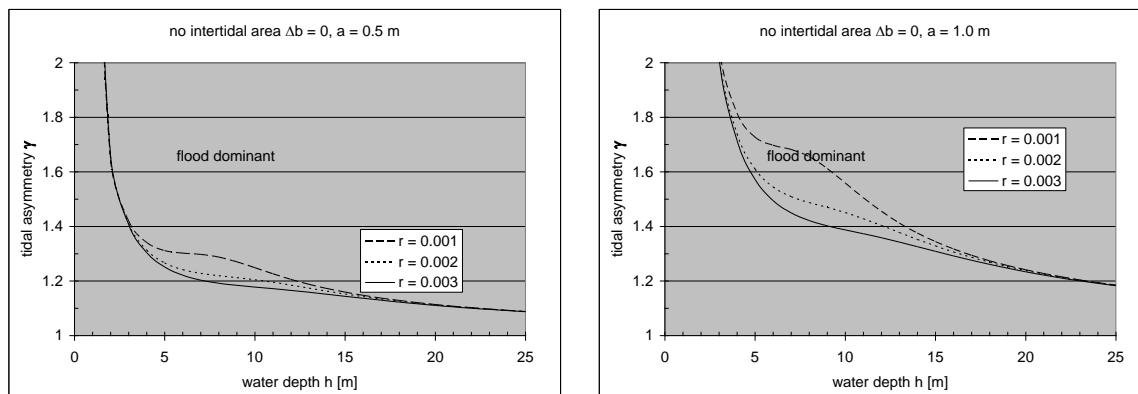


Fig. 2.10: Tidal asymmetry $\gamma (= c_{HW} / c_{LW})$ without intertidal area.

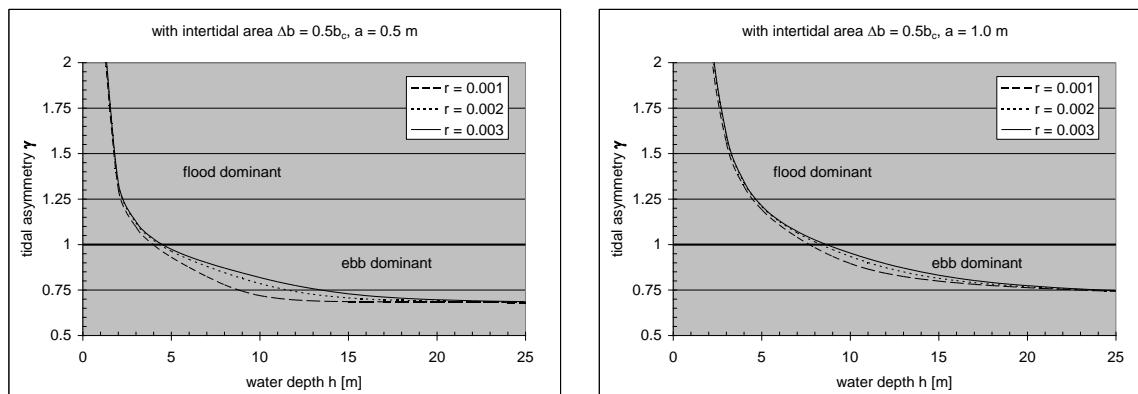


Fig. 2.11: Tidal asymmetry $\gamma (= c_{HW} / c_{LW})$ with some intertidal area.

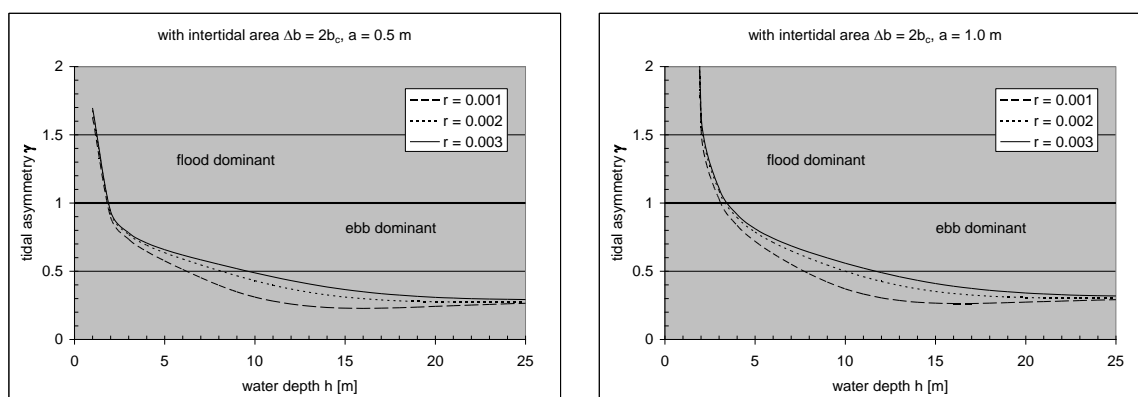


Fig. 2.12: Tidal asymmetry $\gamma (= c_{HW} / c_{LW})$ with large intertidal area.

Our linear analysis also allows for an assessment of tidal asymmetry, analyzing the celerity at high and low water, e.g. equ. (20). This analysis requires information on the tidal amplitude, and we present results for $a = 0.5$ m and $a = 1$ m (kept constant along the river), bearing in mind that

the amplitude should be small compared to water depth in our linear approach. The tidal asymmetry parameter γ is presented in the Fig.'s 2.10, 2.11 and 2.12 as a function of water depth for three values of hydraulic drag and three values of intertidal area. Remember that $\gamma > 1$ implies flood dominant conditions.

These graphs suggest a large sensitivity of the tidal asymmetry as a function of the size of the intertidal area. Without intertidal area, the estuary is always flood dominant. This dominance decreases with increasing depth and roughness, but is shown to increase rapidly with tidal amplitude. Small areas of intertidal area (represented by $\Delta b = 0.5b_c$) already have a major effect on the tidal asymmetry. However, Fig. 2.11 suggests that with increasing amplitude such transition can be obtained at larger depths only. Or, in other words, after deepening, restoration of the intertidal only is likely not sufficient to restore the original situation.

These results further suggest that in very shallow estuaries, with depths of a few meters only, flood dominant conditions will always prevail, even for very large intertidal areas.

Finally, the figures (especially Fig. 2.10) suggest a positive feed-back at high concentrations of fine sediment – at these conditions, the effective hydraulic drag reduces, and the system becomes even more flood-dominant, while at the same time the tidal amplification in the estuary increases.

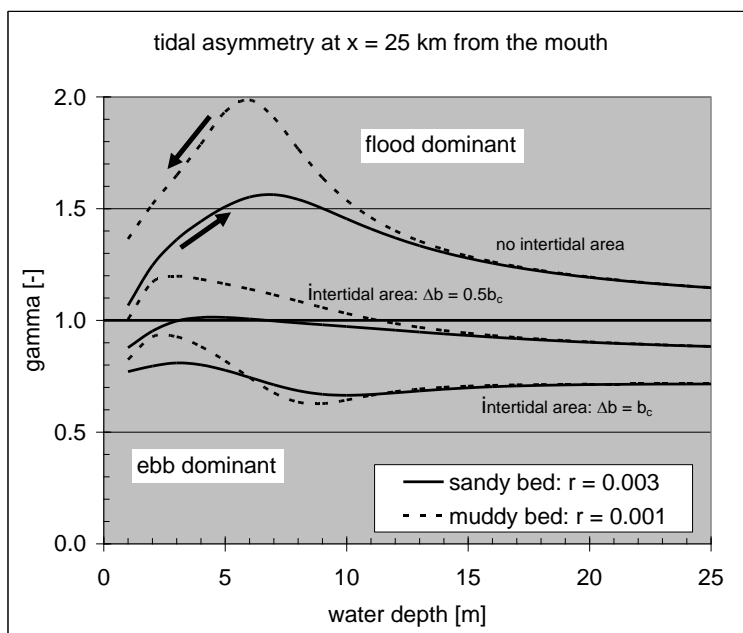


Fig. 2.13: Tidal asymmetry in converging tidal river as function of water depth and intertidal area ($\ell = \infty$, $L_b = 33$ km).

The results of the Fig.'s 2.7 – 2.9 and 2.10 – 2.12 are combined in Fig. 2.13, where we present the tidal asymmetry at $x = 25$ km, i.e. almost one converging length from the mouth. First, we have computed the tidal range at this location, accounting for tidal amplification as a function of water depth, hydraulic drag and intertidal area. The resulting amplitude was then substituted into equ. (20) computing the tidal asymmetry at $x = 25$ km.

Fig. 2.13 shows initially a rapid increase in tidal asymmetry with water depth at water depths between 3 and 7 m in the case without intertidal area. This is in particular true for cases of low hydraulic drag, as when fluid mud is present. This figure also suggests hysteresis in the response of a hyper-concentrated river in case of undeepeening.

For the case with some intertidal area ($\Delta b = 0.5b_c$) the tide is more or less symmetrical, except at low hydraulic drag. When the intertidal area is sufficiently large, ebb-dominant conditions always prevail, and the river is fairly resilient to deepening, as no feed-back occurs.

Fig. 2.13 suggests that in case of no or little intertidal area, deepening leads to progressive flood-dominant conditions, pumping mud into the estuary (or arresting river-borne sediments), as a result of which the hydraulic drag decreases and asymmetry increases further. This would yield a hysteresis in the response of the river to deepening – re-establishing the initial depth will not automatically lead to the pre-deepening conditions of the river.

3. Fine sediment transport in narrow estuaries

3.1 Transport components

In the previous section, we have discussed the development of the tide in a converging estuary. However, an assessment of the tidal evolution of the dynamics of fine sediment transport requires more information. In this section we derive the components for the transport of fine sediment in narrow estuaries, i.e. lateral gradients are small, and discuss components are affected by the tidal dynamics discussed in Chapter 2. We follow Uncles (1985), Fischer et al. (1979) and many others in the decomposition of fine sediments in narrow estuaries. The cross section of the estuary is schematized as before through the compound channel in Fig. 2.1, and we neglect all lateral variations in the flow-carrying cross section. Moreover, again we assume that the flow-carrying cross section A_c may be modeled as $A_c = hb_c$. The longitudinal transport of fine sediment is described with the advection-diffusion equation, in which the effects of exchange of fine sediment between main channel and intertidal area, and over the cross-section of the estuary are accounted for by a dispersion term D_x :

$$\frac{\partial(b_c + \Delta b)hc}{\partial t} + \frac{\partial b_c huc}{\partial x} - \frac{\partial}{\partial x} hb_c D_x \frac{\partial c}{\partial x} = [P(x,t) - S(x,t)](b_c + \Delta b) \quad (22a)$$

in which huc is the fine sediment flux $f(x,t)$ per unit width through the flow-carrying cross section, and P and S are production (f.i. from erosion) and sink terms (in particular sedimentation on intertidal areas) per unit width. In the case of a dynamic equilibrium, we may cancel erosion and deposition in the channel itself, and only the sink term in (22a) is maintained. If we further neglect longitudinal turbulent diffusion, we can simplify equ. (22a) into

$$\frac{\partial hc}{\partial t} + \frac{b_c}{b_c + \Delta b} \frac{\partial huc}{\partial x} - \frac{b_c}{b_c + \Delta b} \frac{1}{L_b} huc = -\frac{\Delta b}{b_c + \Delta b} S(x,t) \quad \text{or} \quad (22b)$$

$$\frac{\partial hc}{\partial t} + \frac{b_c}{b_c + \Delta b} \left(\frac{\partial f}{\partial x} - \frac{f}{L_b} \right) = -\frac{\Delta b}{b_c + \Delta b} S(x,t) \quad (22c)$$

Further to its effects on the tidal movement in a converging estuary, the loss of intertidal area will reduce accommodation for deposition of fine sediment ($S \rightarrow 0$), and the mass of sediment in the estuary per unit width hc increases.

Next, we elaborate on the flux f addressing the various contributions by estuarine circulation, tidal asymmetry, etc. Therefore, water depth h , flow velocity u and suspended sediment concentration c are decomposed in depth-mean values, their variation over depth, tide-mean values, and variation over time²⁾:

²⁾ Note that in our schematization b_c and Δb are not a function of time, though at low water, $b_{tot} = b_c$.

$$\begin{aligned}
h &= \langle h \rangle + \tilde{h}(t) \\
u &= \langle \bar{u} \rangle + \tilde{u}(t) + \langle u'(z) \rangle + \tilde{u}'(z, t) \\
c &= \langle \bar{c} \rangle + \tilde{c}(t) + \langle c'(z) \rangle + \tilde{c}'(z, t) \quad \text{with} \\
\langle \tilde{x} \rangle &= \frac{1}{T} \int_T \tilde{x} \, dt = 0, \quad \bar{x}' = \frac{1}{h} \int_h x' \, dz = 0
\end{aligned} \tag{23}$$

in which $\tilde{\square}$ and $\bar{\square}$ represent variation over time and depth, respectively, and triangular brackets and overbar averaging over the tidal period T and water depth h , respectively. Note that all parameters in equ. (23) are still a function of x . Substituting equ. (23) into the advection term of equ. (22a), yields for the longitudinal sediment flux per unit width F [kg/m], integrated over the depth first and next over the tidal period:

$$\begin{aligned}
F &= \int_T \left\{ \int_h (uc) \, dz \right\} dt = T \langle \bar{f} \rangle = T \langle h \bar{u} \bar{c} \rangle = \\
&= T \left[\langle h \rangle \langle \bar{u} \rangle \langle \bar{c} \rangle + \langle h \rangle \langle \tilde{u} \cdot \tilde{c} \rangle + \langle h \rangle \langle \bar{u}' \bar{c}' \rangle + \langle h \rangle \langle \tilde{u}' \tilde{c}' \rangle + \right. \\
&\quad \left. + \langle \tilde{h} \left(\langle \bar{u} \rangle \tilde{c} + \tilde{u} \langle \bar{c} \rangle + \tilde{u} \cdot \tilde{c} + \bar{u}' \bar{c}' + \langle \tilde{u}' \tilde{c}' \rangle + \langle \bar{u}' \bar{c}' \rangle + \langle \tilde{u}' \tilde{c}' \rangle \right) \right] = \\
&= T \left[\langle \bar{u} \rangle \langle h \cdot \bar{c} \rangle + \langle \tilde{h} \cdot \tilde{u} \rangle \langle \bar{c} \rangle + \langle h \cdot \tilde{u} \cdot \tilde{c} \rangle + \right. \\
&\quad \left. + \langle h \cdot \bar{u}' \bar{c}' \rangle + \langle h \cdot \tilde{u}' \tilde{c}' \rangle + \langle \tilde{h} \cdot \bar{u}' \bar{c}' \rangle + \langle \tilde{h} \cdot \tilde{u}' \tilde{c}' \rangle \right] \equiv F_r + F_S + F_p (= F_a) + F_g + F_v + F_l
\end{aligned} \tag{24}$$

Here we have defined the following six contributions to the longitudinal transport of fine sediment, ignoring the possible longitudinal transport by dispersion (D_x ; even though this transport can be large):

F_r Residual fine sediment transport as a result of net river flow and a net transport rectifying for Stokes drift, in which $\langle \bar{u} \rangle$ = residual flow velocity (river flow and rectifying Stokes drift). If the Stokes drift is zero, as for low-friction synchronous converging (short) estuaries, then $F_r = T q_{riv} \langle h \cdot \bar{c} \rangle / h$, where q_{riv} = specific river discharge, i.e. per unit width.

F_S This term is known as the Stokes drift. For a low-friction synchronous (short) estuary with exponentially converging river plan form. For fine sediments, which are reasonably well mixed over the water column, the Stokes drift F_S and its rectification are more or less equal, and we do not further discuss these terms.

F_p This term is generally known as tidal pumping. Note that this term represents the important asymmetries in peak velocity and in slack water velocity (scour and settling lag), and is responsible for the net transport of (fine) sediment by tidal asymmetry. We

will therefore refer to this term as F_a , highlighting the tidal asymmetry contributions. The tidal analysis discussed in Chapter 2 focuses on this term.

- F_g This term is generally referred to as the estuarine circulation, or gravitational circulation, induced by longitudinal salinity gradients – sometimes longitudinal gradients in temperature and/or suspended sediment may play a role as well, but these are not elaborated in this report.
- F_v This term represents asymmetries in vertical mixing, sometimes referred to as internal tidal asymmetry (Jay and Musiak, 1996). Note that these asymmetries can be induced by vertical salinity gradients, and/or by vertical gradients in suspended sediment.
- F_l The last two terms are triple correlations, and represent lag effects, such as around slack water, and settling and scour lag (e.g. Dronkers, 1986; Postma, 1961; and Van Straaten & Kuenen, 1957 & 1958). Note that these triple products are often ignored in literature on the decomposition of transport fluxes, though they can be very important, in particular for starved-bed conditions.

The decomposition of transport terms was first developed to study the salinity distribution in estuaries (e.g. Dyer, 1997 and Fischer et al., 1979). Later, for instance Uncles (1985) and others applied this technique analyzing sediment fluxes in estuaries. Note that different authors use various definitions for the transport components in equ. (24) – the various terms therefore may not always directly be compared with literature values.

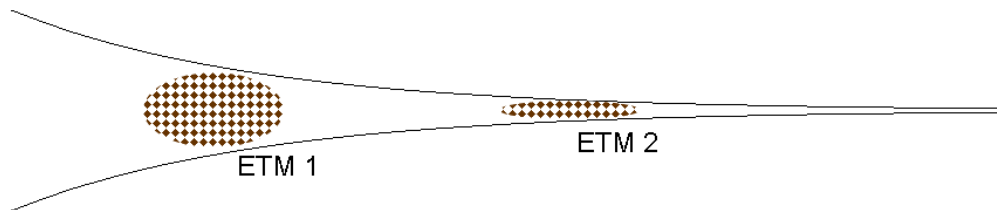


Fig. 3.1: Sketch of converging estuary with two ETM's (estuarine turbidity maximum).

The transport by asymmetries in tidal peak velocity (also referred to as tidal pumping) is important in particular for alluvial conditions, i.e. when abundant fine sediment is available. This is certainly the case in rivers such as the Ems River and Loire River, as explained below. When the river bed is predominantly sandy containing little fines (starved bed conditions), asymmetries in/around the slack water period are often more important.

In general, one finds a turbidity maximum near the mouth of the estuary near the head of salinity intrusion, referred to as ETM-1 in Fig. 3.1. Here, the sediment transport is governed by a balance between river-flow induced flushing, and import by estuarine circulation (possibly in conjunction with salinity-induced internal tidal asymmetry) and tidal asymmetry (slack water asymmetry) – the more important terms are given in bold:

$$\mathbf{F}_r + \mathbf{F}_a + \mathbf{F}_g + F_v + F_l = 0 \quad (25a)$$

It may be argued that as long as the river flow is large enough to flush the turbidity maximum out of the river at times (once a year?), no fine sediments can accumulate in the river forming hyper-concentrated conditions. Our linear model is unsuitable to analyze such conditions in more detail, though a qualitative description is given in Section 3.2.

When suspended sediment concentrations within the river, and/or when sediment loads from the river are large, a second turbidity maximum may be formed (ETM2 in Fig. 3.1) through a balance by river-induced flushing and tidal asymmetry (peak velocities and internal asymmetry):

$$F_r + F_a + F_v + F_t = 0 \quad (25b)$$

Again, the most important processes are given in bold. Such a second ETM is found for instance in the Ems River (Fig. 3.2) where high suspended sediment concentrations are found in the fresh water region, well beyond the head of salinity intrusion. However, Fig. 3.2 suggests that within the Ems no localized ETM is found, but a large patch of highly turbid water that moves to and from with the tidal excursion. We anticipate that this is due to the slow remobilization of sediment from the bed, inducing a longitudinal dispersion of the sediment over the tidal excursion.

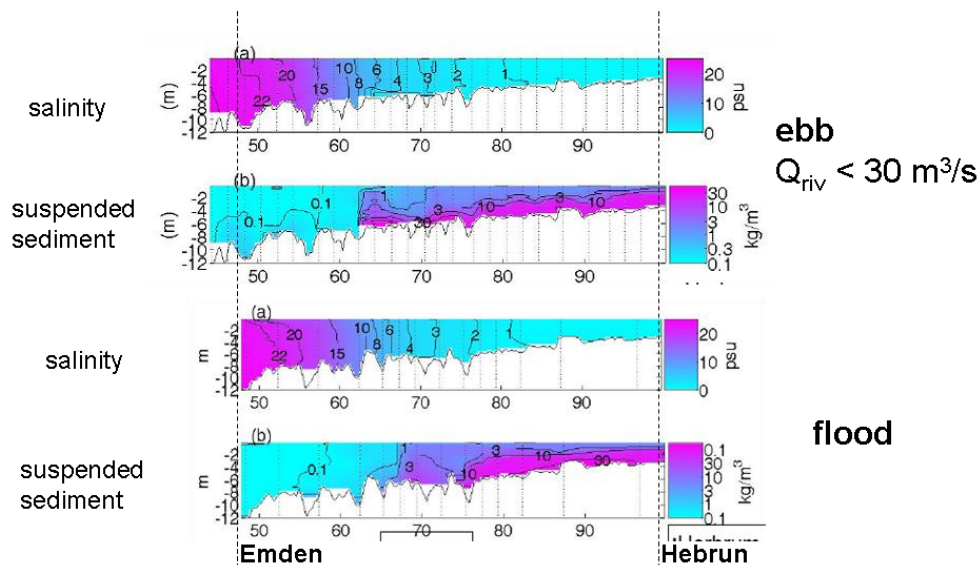


Fig. 3.2: Measured (August 2, 2006) salinity and SPM distributions in the Ems River during flood and ebb (after Talke et al., 2009) – note that the suspended sediment dynamics have become independent of the salinity dynamics.

In Section 3.4 we describe qualitatively the evolution from a “normal” estuary to a hyper-concentrated system, with the Ems River as an example. We argue that it is the change in dominant processes, e.g. from the balance of equ. (25a) to (25b) which characterizes this regime shift, and which is responsible for the persistence of this new regime with its second turbidity maximum (ETM 2).

3.2 Reduction in effective hydraulic drag

In Chapter 2 we have shown that the response of the tide in a converging estuary is sensitive to the effective hydraulic drag. In this section we present a simple formula to assess reductions in hydraulic drag as a function of suspended sediment concentration. Note that these formulae do not apply for very high concentrations, when fluid mud is formed (occasionally).

Winterwerp et al. (2009) derived a simple formula to quantify the reduction in hydraulic drag as a function of enhanced levels of suspended sediment concentration and longitudinal salinity gradients:

$$\frac{\bar{u}}{u_*} \equiv \frac{C_{eff}}{\sqrt{g}} = \frac{C_0}{\sqrt{g}} + \frac{C_{SPM}}{\sqrt{g}} = \frac{C_0}{\sqrt{g}} + 4 \frac{h}{h_{ref}} \mathbf{Ri}_* \beta \quad (26a)$$

or in terms of excess Chézy coefficient:

$$\frac{\Delta C_{eff}}{\sqrt{g}} = 4h \mathbf{Ri}_* \beta \quad (26b)$$

in which the Rouse number β and bulk Richardson number \mathbf{Ri}_* are defined as:

$$\mathbf{Ri}_* \equiv \frac{(\rho_b - \rho_w) gh}{\rho_b u_*^2} = \frac{\varepsilon_\rho c gh}{(\rho_w + \varepsilon_\rho c) u_*^2} \quad \text{and} \quad \beta \equiv \frac{\sigma_T W_s}{\kappa u_*} \quad (27)$$

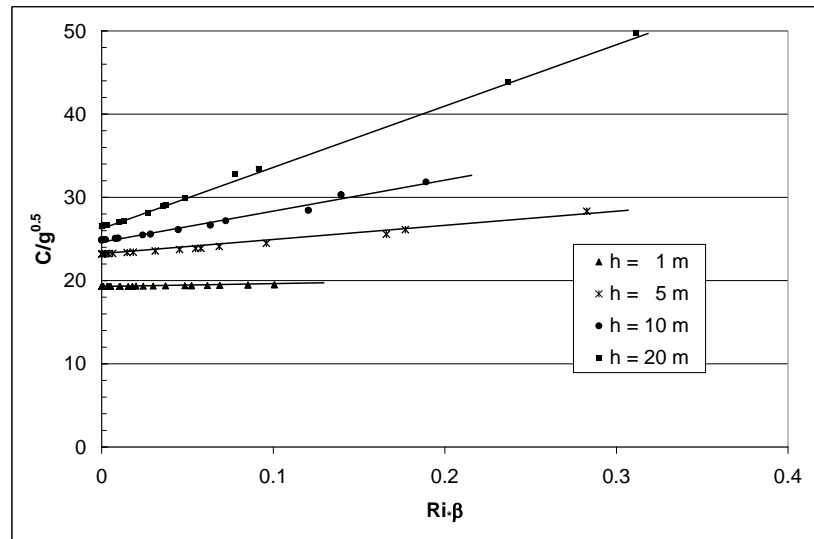


Fig. 3.3: Effective hydraulic drag (Chézy coefficient) as function of the bulk Richardson and Rouse number.

From the implicit equ. (27) we can draw the following conclusions on the effective Chézy number:

1. The effective Chézy coefficient increases, hence the hydraulic drag decreases with increasing water depth.

2. The effective Chézy coefficient increases with suspended sediment concentration c .
3. The effective Chézy coefficient increases with settling velocity, hence with flocculation.

Note that the reduction in effective hydraulic drag is essentially induced by vertical stratification, induced by vertical gradients in the suspended sediment (SPM) concentration. Because of hindered settling effects, the same vertical gradient in SPM concentration can exist at relatively low and relatively high concentrations. Or in other words, low- and high-concentrated mixtures can be kept in suspension with the same kinetic energy (e.g. Section 3.3).

Hence, the effective Chézy coefficient scales with the following dimensionless parameters:

$$\boxed{\frac{C_{eff}}{\sqrt{g}} \propto \mathbf{Ri}_*, \beta} \quad (28)$$

The relation between the effective Chézy coefficient and suspended sediment concentrations (e.g. equ. (26)) is shown in Fig. 3.3. Note that the rivers discussed in this report have water depth of typically 5 – 10 m, hence we expect an increase in the effective Chézy coefficient by 15 – 30 m^{1/2}/s. Only the Elbe is considerably deeper, and the excess Chézy value is therefore expected to be larger as well.

3.3 Hyper-concentrated conditions

The literature contains a variety of definitions on hyper-concentrated conditions. In this section, we present a definition which is relevant for the present study. Winterwerp (2011) argues that the Ems and Loire River are currently in these hyper-concentrated conditions.

In our definition, hyper-concentrated conditions are related to the concept of saturation (e.g. Winterwerp, 2001). Let us assume a straight, prismatic channel with a uniform flow at flow velocity U_1 . First, we analyze the transport of sand in suspension. From all classical literature, and data on sand transport, we know that an equilibrium sand transport is established, with an equilibrium vertical profile in suspended sand concentration, which can be described with a classical Rouse profile. This profile describes a balance between vertical turbulent mixing and settling of the grains by gravity. If the flow velocity U_1 is reduced to U_2 , then a new equilibrium is established immediately, at smaller suspended sand concentrations though. A new equilibrium between vertical turbulent mixing and settling is established, the suspended sand concentration being smaller because turbulent mixing is smaller owing to the decrease in flow velocity. Note that upon deposition from state 1, sand grains form a rigid bed immediately, allowing full turbulent production, at state 2 conditions, though.

In the case of fine suspended sediment, a different picture emerges, owing to the fact that fine sediment consists of flocs with high water content (up to 95%). When the flow velocity decreases from U_1 to U_2 , the fine sediment flocs settle as well, owing to the decrease in turbulent mixing in response to the lower flow velocity. However, these flocs do not form a rigid bed immediately, but a layer of soft fluffy sediment. As a result, turbulence production decrease beyond the value expected at state 2 conditions over a rigid bottom, and more flocs settle, as turbulent mixing drops further. This snowball effect continues till virtually all flocs have settled on the bed: a layer of fluid mud has been formed. These conditions are referred to as saturation, and have been elaborated in detail in Winterwerp (2001).

A similar condition emerges when the flow velocity is kept constant, but the suspended fine sediment concentration slowly increases. At a certain level, referred to as the saturation concentration, vertical turbulent mixing is too small to keep the flocs in suspension, and a fluid mud layer is formed by the snowball effect described above. This is depicted in Fig. 3.4 (e.g. Winterwerp, 2011, 2006). The horizontal axis depicts the volumetric concentration ϕ of the suspended sediment, in case of fine sediment, the volume concentration of the flocs; the vertical axis depicts the flux Richardson number \mathbf{Ri}_f , a parameter describing that part of the kinetic energy of the flow available for mixing.

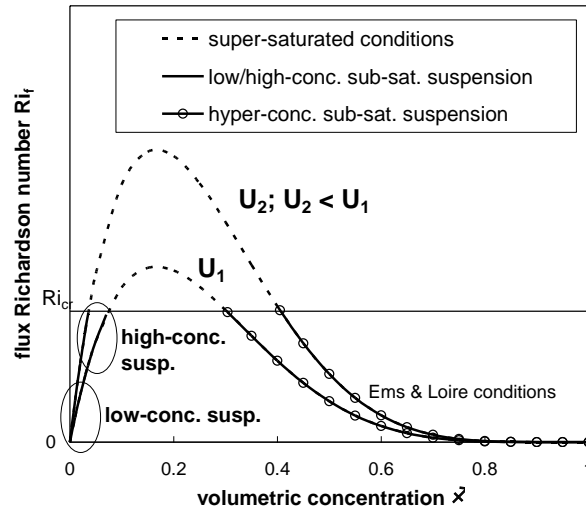


Fig. 3.4: Stability diagram showing saturation and super-saturated conditions (dotted line). At smaller concentrations rivers are in the left branch of the diagram, at higher concentrations, right-branch conditions prevail – these are referred to as hyper-concentrated conditions. The flux Richardson number \mathbf{Ri}_f yields a proxy for the (kinetic) energy required for vertical mixing, and this diagram shows that each value of \mathbf{Ri}_f (at sub-critical conditions) can be obtained with two different volumetric concentrations.

From the above, and from Fig. 3.4 we can conclude that at low suspended sediment concentrations (left branch of Fig. 3.4), an increase in suspended sediment concentration, for instance through erosion of the bed, will ultimately lead to a collapse of the concentration profile, the formation of fluid mud, hence super-saturated conditions. In terms of Fig. 3.4, we follow the stability curve to the right, and up to larger \mathbf{Ri}_f values until a critical value is surpassed. In Section 3.2 we have shown that prior to these conditions, already a profound decrease in effective hydraulic drag may occur.

In the right-hand branch of the stability diagram, we refer to hyper-concentrated conditions. The suspended sediment concentration is so high, that the sediment's settling velocity decreases significantly (up to two orders of magnitude), so that very little turbulent energy/mixing is required to keep the sediment in suspension. Furthermore, we note that if the flow would erode sediment from the bed, we would follow the stability curve to the right, but now to lower \mathbf{Ri}_f values, contrary to the low-concentrated conditions above. This implies that the suspension becomes more stable: “it likes” to erode the bed, reducing the energy to keep the sediment in suspension. This is one reason that hyper-concentrated conditions are so persistent, and that rivers, such as the Ems and the Loire, brought into these hyper-concentrated conditions, are

difficult to train back into conditions more favorable from an environmental point of view. The reader is referred to Bruens et al. (2012) for a full analysis on the stability of these hyper-concentrated conditions, and why they do not consolidate, but remain fluid over such long periods of time.

3.4 A qualitative description of the regime shift in the Ems estuary

Winterwerp (2010) analyzed how the Ems River responded to ongoing deepening. We have no data on the transition of the Ems River from a “normal” turbid river into its current, hyper-concentrated state over time (Fig. 3.2). Therefore, we have developed a conceptual picture for the transition of the river as a result of deepening from its former equilibrium, using our observations described on the previous pages. This picture is summarized in Table 3.1. We start a long time ago from a long-term equilibrium, referred to as phase 0 in Table 3.1, at which up-river directed fine sediment transport induced by gravitational circulation and the various effects of tidal asymmetry balance the down-river transport induced by the river flow. The fine sediments in the Ems River are mainly marine-born, though some sediment may be delivered by the river. Over shorter time periods, accumulation or flushing may occur, as a result of e.g. varying river flows. Under these conditions, the formation of an estuarine turbidity maximum (ETM) is expected near the head of the saline intrusion. Over longer time scales, land formation initiated on vegetated mudflats, may reduce the river’s tidal volume, affecting the long-term morphodynamic equilibrium.

As a response to deepening, net accumulation is expected, restoring equilibrium, Phase 1, Table 3.1. The underlying processes are a decrease in river-induced flushing, as river flow velocities decrease in proportion to the river’s cross section, in conjunction with an augmented net transport by gravitational circulation, as water depth increase (scales with h^2). Deepening would also increase tidal asymmetry in case of reduced intertidal areas (e.g. Chapter 2). Possibly, reduced vertical mixing already starts to play a role, enhancing the trapping efficiency of the river (see below). As the accumulating fine sediments do not form a rigid bed immediately, also turbidity levels increase, as more sediments are available for remobilization, and suspended sediment concentrations in the ETM increase.

A further increase of the river’s depth would increase the amount of remobilizable sediments further, accompanied by a further increase in suspended sediment concentrations. When the riverbed becomes predominantly muddy, profound feed-backs between the various processes are expected through which the river evolves into its present hyper-concentrated state. In this regime, gravitational circulation still plays a role, but its effect is small compared to the dominant contributions of internal tidal asymmetry, with profound differences in vertical mixing during ebb and flood: during ebb, the river is highly stratified by sediment-induced buoyancy destruction.

Winterwerp (2010) suggests that this regime shift may be initiated in the Ems River at depth-averaged concentrations typically of the order of a few 100 mg/l. Then, the trapping efficiency of the river increases rapidly as a result of vertical stratification during ebb, and asymmetry in floc size. The rate at which the river really accumulates fine sediments is determined merely by the supply of these sediments from the Wadden Sea – Dollard estuary, than by internal hydro-sedimentological processes.

We anticipate a second regime shift in the estuary, Phase 3, Table 3.1, when the river starts to develop pronounced occurrences of fluid mud, as observed presently by Schrottke (2008). In that case, fine sediment transport rates are expected to be dominated by the tidal asymmetry of the

peak currents themselves. Now re-entrainment of the fluid mud layers, which scales with U^3 as well, becomes a dominant mechanism (Bruens et al., 2012). Sediment is transported up-river towards the river's head at Herbrum by the large tidal asymmetry, and the entire river becomes highly turbid. As the consolidation rate of fluid mud layers scales with their thickness squared, we expect that the properties of the fluid mud layer are fully determined by the velocities during flood conditions. Note that not much consolidation of the thick fluid mud layers during ebb is expected.

Table 3.1: Summary of Ems River response to its deepening – see text for further explanation; river depth in Phases 2 and 3 are not necessarily larger than in Phase 1. Phase 0 refers to “undisturbed” state of the river.

phase	dominant transport processes		comments
	flood-directed transport	ebb directed transport	
0	“normal” estuary with ETM; equilibrium ^{†)}		long-term balance between ebb and flood transport
	(slack water) tidal asymmetry; gravitational circulation ^{§)}	river-induced flushing	
1	small disturbance; transient state		net import; weak feed back
	(slack water) tidal asymmetry ? enhanced gravitational circ.	reduced river-induced flushing	
2	large disturbance; transient state		large net import; strong feed-back; large trapping
	internal tidal asymmetry: mixing & floc size; limited sediment load & determined by ebb conditions; fairly well-mixed flood; relative unimportant grav. circ.; sediment-induced grav. circ. ?	stratified ebb; fluid mud; small ebb transport	
3	hyper-concentrated estuary; new equilibrium ^{‡)}		large net import; strong feed-back; large trapping
	asymmetry in tidal velocity; internal tidal asymmetry; pronounced fluid mud formation; capacity conditions; transport formula applicable		

^{§)} Including possible effects of internal asymmetry, in particular when the salinity field is stratified,

^{†)} Long-term equilibrium may be disturbed by land formation, reducing estuary's tidal volume,

^{‡)} Without maintenance, estuary may return towards its original state if a rigid bed can be formed.

In summary, we infer that in response to deepening of the Ems River, the sediment load in the river first increases through an increase in the up-river transport by gravitational circulation and a decrease in river-induced flushing. Then, in the second phase of the river's transition towards its hyper-concentrated state, when the concentration in the river attains values of a few 100 mg/l, internal tidal asymmetry becomes dominant because of pronounced interactions between the sediment load, and the turbulent water movement and vertical mixing. We believe that the 1990-survey conditions (e.g. Van Leussen, 1994) fall within this second phase of development. Finally, the load of fine sediment becomes so large that in the final phase of the river's evolution, thick fluid mud layers are formed, and the up-river fine sediment transport is dominated by tidal

asymmetry of the current velocity. The second phase in transition is probably not stable: trapping is so large that a further development towards the final phase may be inevitable; the time scale of this intermediate phase depends mainly on the sediment supply, and may amount to a decade or so, as in the Ems River.

Finally, tidal reflections from the weir at Herbrum are expected to augment the tidal range by a few dm (e.g. Fig. 2.4), further increasing the tidal pumping of mud into the river.

4. Comparison of various estuaries

In this section, we compare properties and evolution of a number of estuaries and tidal rivers:

- Ems – Germany & The Netherlands
- Loire – France
- Elbe – Germany
- Weser – Germany
- Upper Sea Scheldt – Belgium

We have some data available for the Humber (Ouse) and Tamar, both in the UK, the Garonne and Vilaine, both in France, and the Passaic River in the USA. Note that Kuijper presented similar analyses for the Western Scheldt estuary.

In the following, the data of the various rivers are analyzed – a synthesis of this analysis is given in Chapter 5. In this phase of the study we ignore the effects of reflection by a weir, as this is not easily to be accounted for in an analytical approach. Based on the graphs of Fig. 2.4, it is anticipated that the tidal amplitude is under-estimated with the single-wave analytical model by a few decimeter. This implies that a lower friction coefficient (larger Chézy value) is required in calibrating the model to reproduce observed tidal elevations. However, we expect that the relative effect of deepening and fine sediments are still reasonably well predicted.

In a next phase of the study we will account for the effects of reflections on barriers/weirs in the river, but in the current study we discuss the effects of reflections only qualitatively.

The procedure of our data analysis is as follows:

1. We determine the convergence length L_b of the estuary, and its possible variations over time, by plotting the width of the river against its longitudinal co-ordinate.
2. We establish historical variations in (mean) water depth and intertidal area, and compute (variations) in the estuarine convergence number Λ_e .
3. We compute the imaginary wave number k_i between subsequent tidal stations from its definition $a_2 = a_1 \exp\{(x_2 - x_1)k_i\}$, where a_2 = tidal amplitude at $x = x_2$ (etc.), and make k_i dimensionless with L_b .
4. We plot the resulting values of κ_i against Λ_e , yielding one data point for each river stretch in a certain time period.
5. We then fit the analytical model (equ.'s (11)) through the data by tuning the roughness parameter r_* . Note that we assume an infinite long river, but sub-divide the river in subsections with more or less constant water depth.
6. We determine the effective Chézy coefficient C from the fitted r_* -values. For this we use the solution for u from the analytical model (e.g. equ. (41) and (5c)).
7. We plot the variation of C with time identifying possible changes in effective hydraulic drag over time.

Hence, the linear model discussed in Chapter 2 is merely used as a tool to analyze the historical data from the various rivers. By making tidal amplification/damping and river geometry/bathymetry dimensionless, we can compare the various rivers mutually (e.g. Chapter 5).

4.1 The Ems River

The Ems River is about 53 km long from the weir at Herbrum to Emden, flowing through Germany into the Ems-Dollard estuary (Fig. 4.1). This river is renowned for its large suspended sediment concentrations, with values up to 30 – 40 g/l over most of the upper part of the river (e.g. Talke et al., 2009). These high concentrations are found well beyond the region of salinity intrusion, and move to and fro with the tide. Also profound layers of fluid mud are found, in particular around slack water and neap tide (e.g. Schrottke, 2008). Currently, the total mass of suspended solids amounts to about 1 Mton, while yearly about 1.5 Mton of solids is removed from the Ems River by dredging. For further details on the river, the reader is referred to Krebs and Weilbeer (2005).

The Ems River is characterized by a profound tapering, as shown in Fig. 4.2. The overall convergence length of the river amounts to about 19 km, whereas for the stretches between Emden – Leerort $L_b \approx 32$ km, Leerort – Papenburg $L_b \approx 27$ km, and Papenburg – Herbrum $L_b \approx 33$ km. In the following, we refer to these three sections as E-L, L-P and P-H. The apparent discrepancy of the overall convergence length and those of three smaller stretches of the river is attributed to some jig-saw patterns in the $b-x$ curve (e.g. Fig. 4.2). In our analysis, we used the larger values.

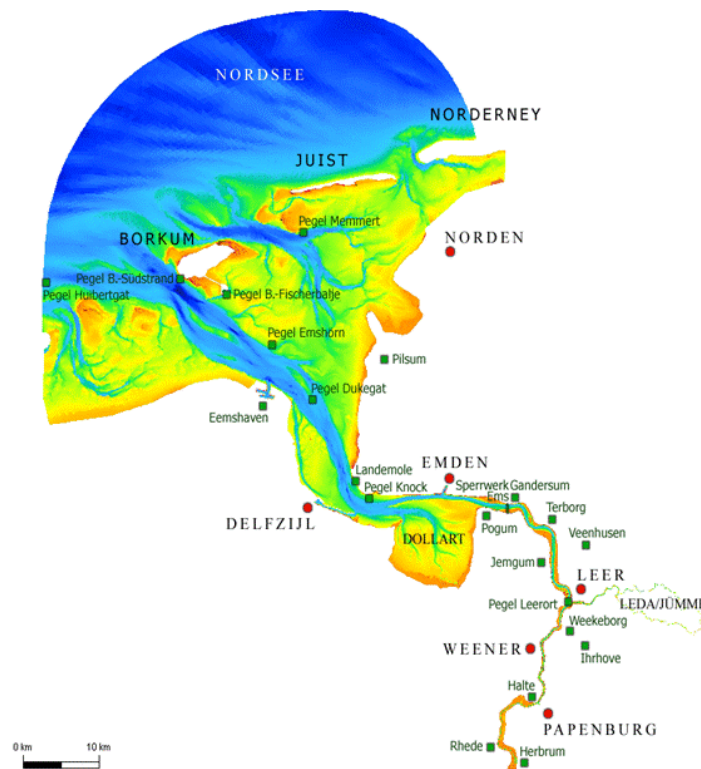


Fig. 4.1: Lay-out of Ems-Dollart estuary and Ems River.

An overview of the various interventions in the river was summarized in Vroom et al. (2012), based on information from Rijkswaterstaat and the Bundesanstalt für Wasserbau. The evolution in depths of the river for the three stretches E-L, L-P and P-H is presented in Fig. 4.3, where the depths have been averaged to obtain mean values for these stretches. Note that after 1940 no reclamation of intertidal area took place, though we anticipate that a large part of the remaining

intertidal areas has been lost in due time owing to sedimentation on these areas (see discussion below). Around 1961, in the upper part of the river (P-H), groins have been constructed, narrowing the river locally.

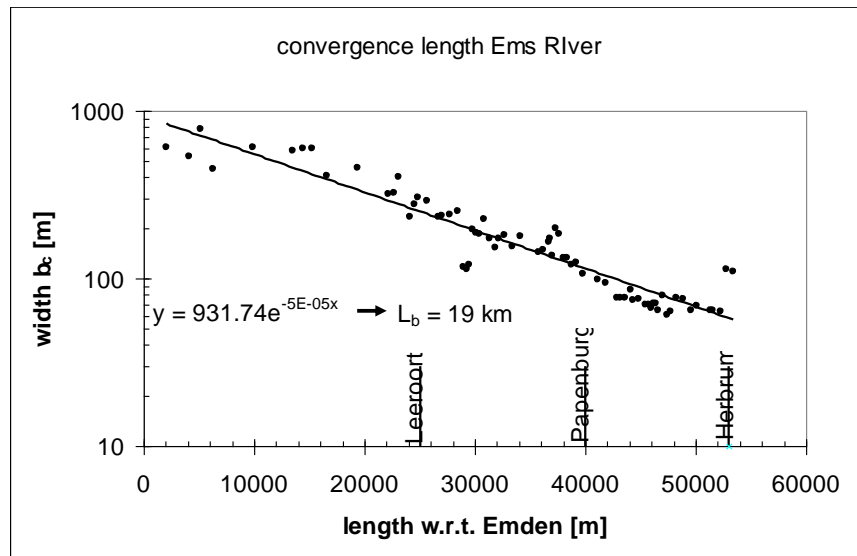


Fig. 4.2: Convergence length of Ems River.

The response of the tidal range to these interventions is presented in Fig. 4.4, in conjunction with an overview of the human interventions (Herrling, 2007). Fig. 4.4 suggests that the response of the tidal range to the various interventions is not instantaneous, but takes considerable time to attain equilibrium – Fig. 4.4 suggests a time scale of at least 20 years. We will address this further below. Finally, it is noted that the tidal range at Herbrum becomes highly irregular as a result of variations in the yearly river flow – this will be elaborated in another study.

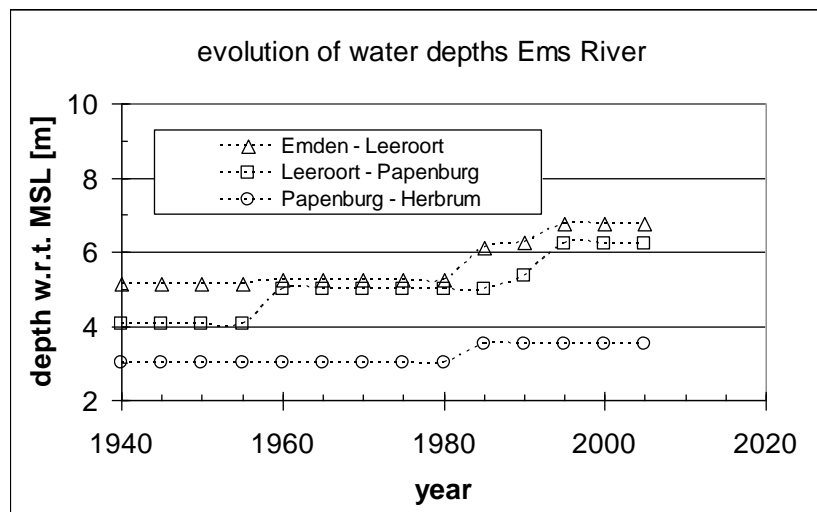


Fig. 4.3: Evolution of mean water depths in Ems River for three trajectories (water depth with respect to mean sea level at Emden).

We note that more regular data are to be expected from harmonic analyses, including the effects of the 18.6 year cycle (see also Chapter 4.5 on the Scheldt data). However, the original data are not in our possession.

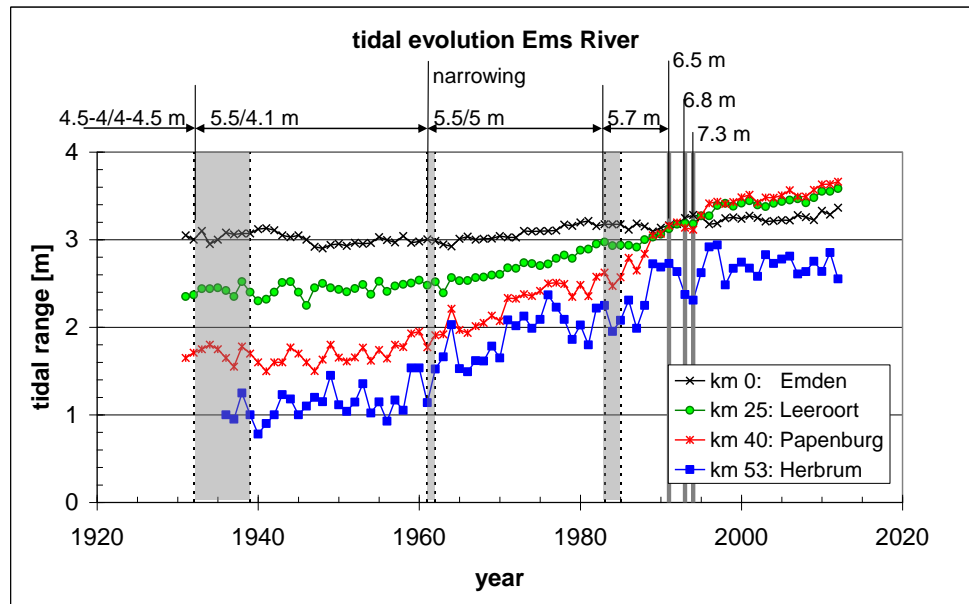


Fig. 4.4: Evolution of measured mean tidal range in Ems River and summary of interventions – 5.5/4.1 m indicates a design depth of 5.5. m over the Emden-Leeroort reach, and 4.5 m over the Leeroort-Papenburg reach; Design depth Papenburg-Herbrum reach was 3 m till 1980, and then 3.5 m (data from BAW, and prior to 1950 by Herrling, 2007).

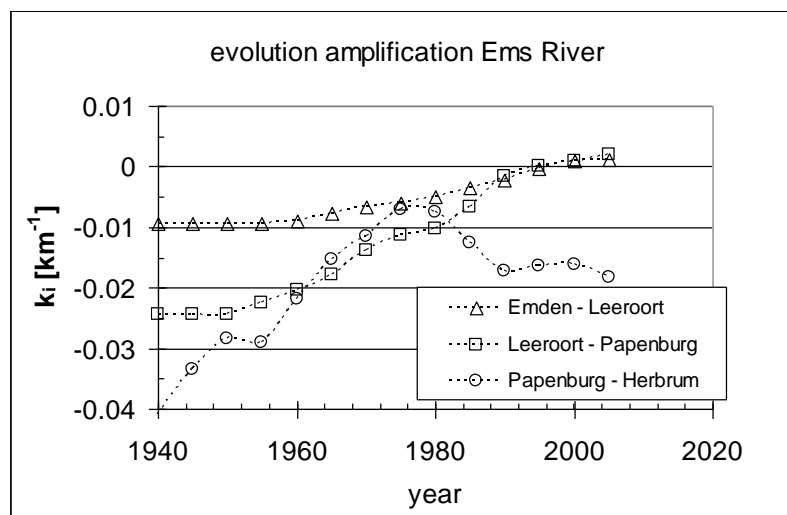


Fig. 4.5: Evolution of imaginary wave number in Ems River; note that in the remainder the data for the trajectory Papenburg – Herbrum have been ignored because of their irregularity.

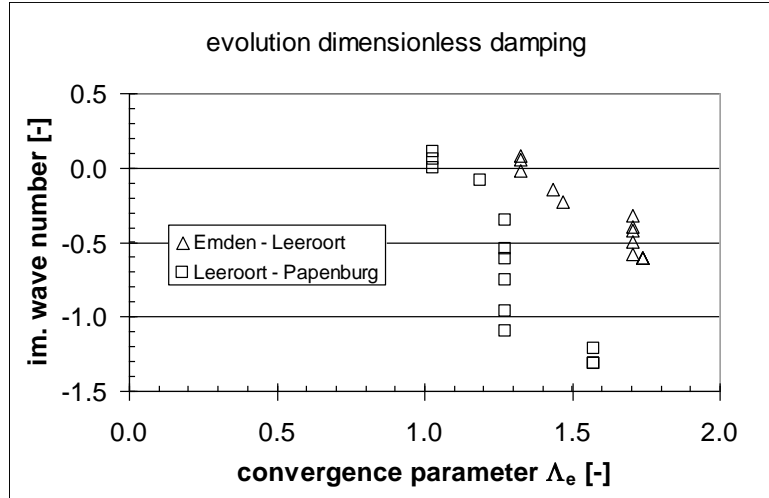


Fig. 4.6: Evolution of dimensionless imaginary wave number κ_i with variations in estuarine convergence number Λ_e .

From Fig. 4.4, the imaginary wave number k_i (amplification factor) was determined. For this purpose, mean values over a period of five subsequent years were determined from the Fig. 4.4-data, and then k_i was determined by dividing the tidal range at Leeroort by that at Emden, etc. The results are presented in Fig. 4.5, showing a regular increase in k_i for the trajectories E-L and L-P. However, for the trajectory P-H, a highly irregular behavior is found. The pattern of this behavior can be entirely changed by using another averaging procedure for the data of Fig. 4.4, or using the tops or troughs of the curve. At present, we are not sure which behavior is representative, and we therefore ignore the behavior of the tide along the trajectory Papenburg – Herbrum. We believe that only a detailed harmonic analysis of the tidal measurements (M2 component) can shed light on the irregular behavior of the Herbrum tidal curve.

Finally it is noted that for both trajectories E-L and L-P the data show that amplification of the tide is observed from 1995 on – before the tidal wave was still damped, though little only.

Next, the imaginary wave number is made dimensionless by the convergence length L_b (e.g. κ_i , equ. 8 & 11) and plotted against the estuarine convergence number Λ_e in Fig. 4.6. Then the linear solution (equ. 13b) is fitted to the data by tuning the roughness parameter r_* , appreciating that the assumptions to attain this linear solution are grossly violated (in particular the tidal range is not small compared to the water depth, and the water depth itself is not constant along the two trajectories under analyses. Yet, the linear solution should allow us to analyze the trends in the data observed in the Ems River.

The results of the calibration are shown in Fig. 4.7, in which the data, presented before in Fig. 4.6 have now been colored to mark the various intervention periods in the river. The 1960 data and earlier for L-P can be fitted with $r_* = 7$, whereas the 1980 data require $r_* = 4$. Note that interventions were carried out in 1960 and 1983 – the response to the 1960 intervention was apparently not yet at equilibrium in 1980.

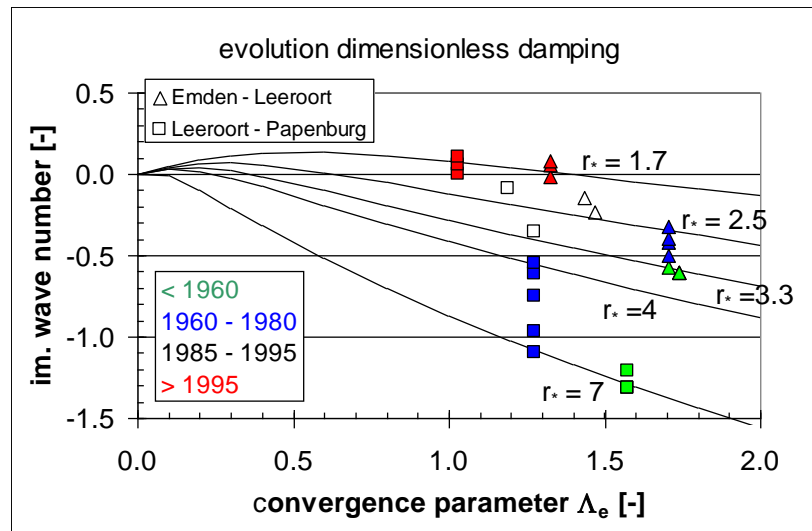


Fig. 4.7: Fits of linear solution to observed data through tuning of roughness parameter in $\kappa_i - \Lambda_e$ diagram.

For a more physical interpretation, the roughness parameter r_* has to be converted; arbitrarily we choose to convert to the Chézy coefficient C . In this conversion we use the observed water depth for the various years, and use the imaginary wave number k_i to determine the flow velocity along the river, assuming that in the 1960s, the peak velocity at Emden was 1 m/s (e.g. equ. 4a). To obtain the variation of C with time, we have fitted the linear solution (as in Fig. 4.7) through all data points by tuning r_* , the results of which are presented in Fig. 4.8.

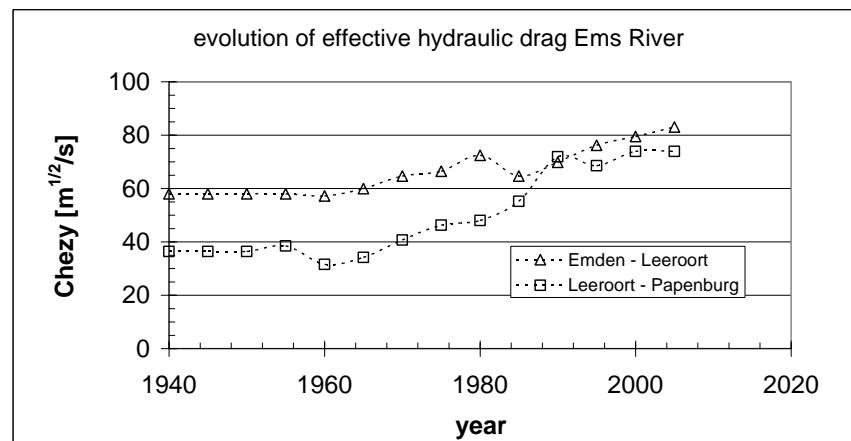


Fig. 4.8: Evolution of effective hydraulic drag (Chézy coefficient) with time.

Fig. 4.8 suggests that up to the 1960s the Ems River was quite rough, with Chézy values in the E-L reach of about $60 \text{ m}^{1/2}/\text{s}$, which is typical for a sandy river bed. Further upstream, in the L-P reach, Chézy values as low as $40 \text{ m}^{1/2}/\text{s}$ are found. We are not certain that these are correct, but if so, they may be indicative for profound steep bed forms (dunes), such as observed for instance in the Elbe and Weser Rivers (e.g. Van Rijn, 1993). The gradual increase in Chézy coefficient between the 1960s and 1980s may then be attributed to a gradual decrease in dune heights and steepness owing to ongoing dredging. However, from the 1990's onward, the Ems River became

more and more infamous for its very high suspended sediment concentrations with hyper-concentrated values after 2000. Today, suspended sediment concentrations measure several 10 g/l, e.g. Talke et al. (2009). The very large values of $C = 80 - 90 \text{ m}^{1/2}/\text{s}$ can be explained by the profound buoyancy-induced damping by the large suspended sediment concentrations. Note that Fig. 4.8 suggests an increase in Chézy values of $15 - 25 \text{ m}^{1/2}/\text{s}$ for the conditions prevailing in the Ems River with water depths between 5 and 10 m.

As we have ignored the effects of tidal reflections against the weir at Herbrum we expect that the Chézy values, in particular for the trajectory Leerort-Papenburg (e.g. Fig. 2.4) are a bit over-estimated, and should be lower by a value of $5 - 10 \text{ m}^{1/2}/\text{s}$.

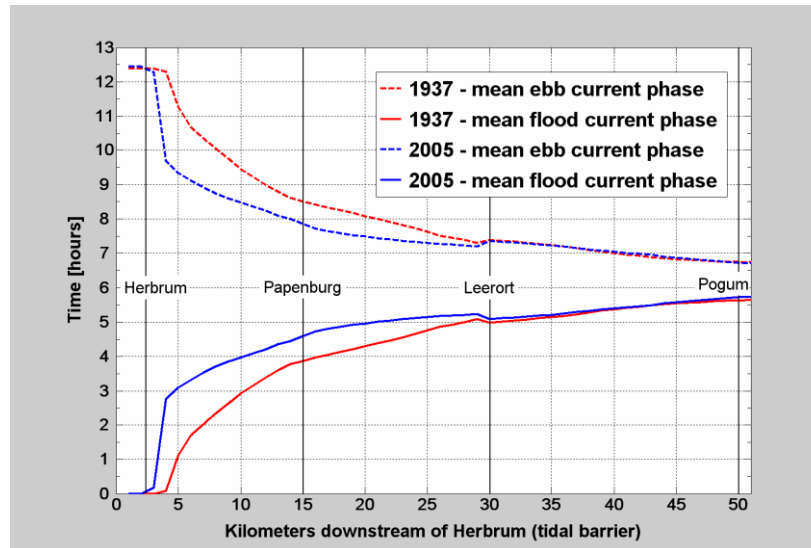


Fig. 4.9: Measured travel time tidal wave along Ems River (Herrling, 2007).

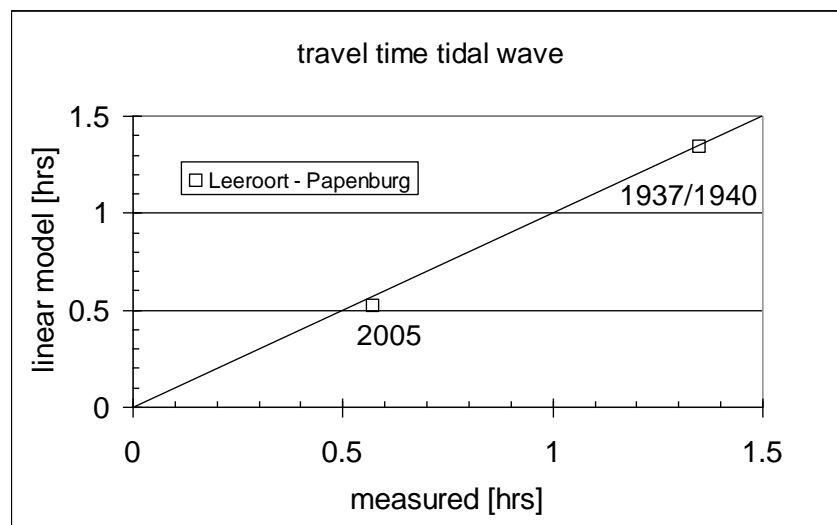


Fig. 4.10: Measured and computed travel time tidal wave along Ems River in 1940 and 2005.

Next the evolution in celerity along the Ems River is elaborated. We start from the data in Fig. 4.9, showing a significant decrease since 1937 in the travel time of the tide upstream of Leerort.

Using the estuarine convergence number Λ_e , and the roughness parameter r_* obtained from calibration of the linear model against the observed evolution in tidal range, the celerity computed with the linear model (equ. 17) can be compared to the data. Fig. 4.10 shows that the linear model predicts the evolution in travel time very well, though only two points in time are available, of course. Fig. 4.9 suggests that this part of the river comes close to synchronous conditions.

Finally, the asymmetry parameter γ (e.g. equ. 18) is determined, using the measured values for water depth and tidal amplitude. The results are presented in Fig. 4.11, showing that over the entire data range, $\gamma > 1$, i.e. flood dominant conditions prevail, as anticipated in Section 2.1 for rivers with little or no intertidal area. The tidal asymmetry remains almost constant for the E-L trajectory of the river, but γ for the L-P trajectory grows continuously after the deepening of the 1960s, exceeding the asymmetry in the E-L range beyond the 1980s. Of course, the tidal asymmetry should be related to (changes) in river flow to get a complete picture of the sediment dynamics in the estuary.

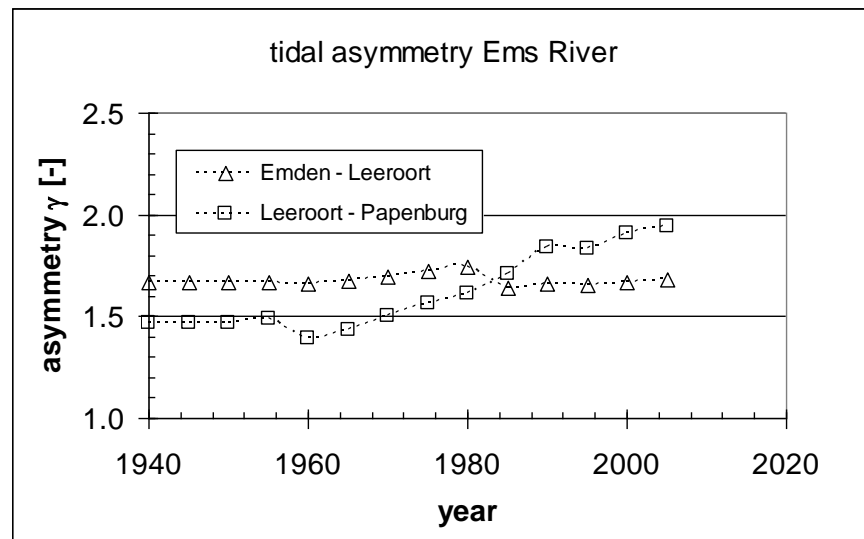


Fig. 4.11: Evolution of tidal asymmetry parameter with time.

4.2 The Loire River

The Loire estuary from St Nazaire to Nantes measures about 53 km. In this report we study the development of the tide in the Loire river from Paimboeuf (at km 14), which is located at the transition between the inner and outer estuary, where the estuary converges strongly, e.g. Fig. 4.12. Hence, we study a stretch of about 40 km. Mean fresh water flow rates range from 400 – 700 m³/s, with maxima up to 5000 m³/s.

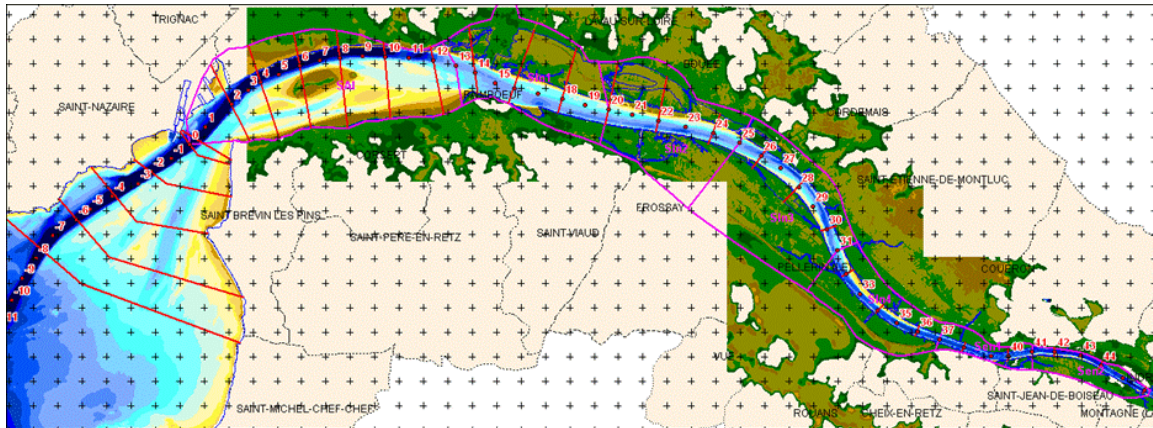


Fig. 4.12: Current plan view of the Loire River; St Nazaire at km 0, Paimboeuf at km 14, Cordemais at km 27, La Martinière at km 37 and Nantes at km 53.

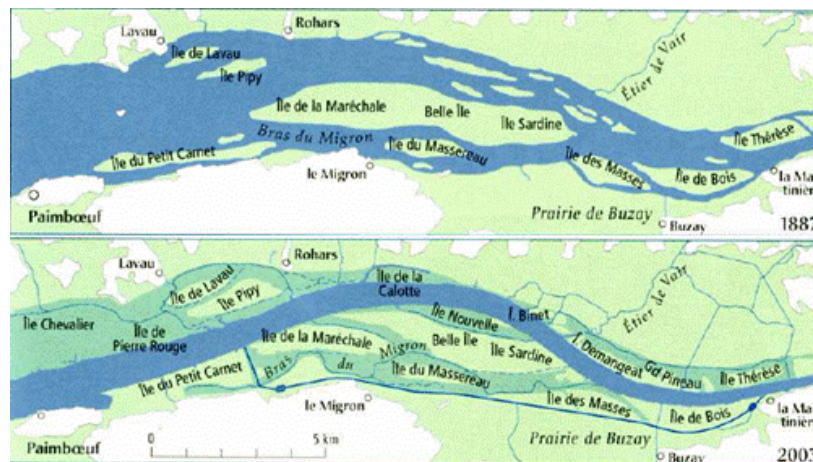


Fig. 4.13: Canalization of the Loire River in 1903 – 1910.

The data discussed below have been collected in a study by Deltares commissioned by GIP (Briere et al., 2012), summarizing reports by Sogreah (2006), in particular Sogreah's report on the historical development of the Loire River.

In the early decades of the 20th century, the Loire River was heavily modified. Fig. 4.13 shows the canalization of a major part of the river, realized in the first decade. Though Fig. 4.13 suggests that modifications were limited to the reaches down-estuary of La Martinière (km 37), canalization and embankments took place up to Nantes. A decade later, e.g. 1910 – 1920 the so-called Bassin Marée has been created by large-scale withdrawal of sand from the river. We were not able to find data on these withdrawals, but Fig. 4.14 suggests that the river bed was affected and lowered well beyond Nantes.

The width of the Loire is plotted against the river length in Fig. 4.15, showing an exponential narrowing with a convergence length of about $L_b = 21$ km. The relatively small width between km 32 and 36 should be attributed to the local presence of groins. Fig. 4.13 suggests that prior to the large scale narrowing of the river early 2000, the convergence length of the river may have been considerably different. As we have no data, we have not altered L_b in our analyses below, but accounted for this narrowing by reducing the relative intertidal area b^* from 2 to 1.1.

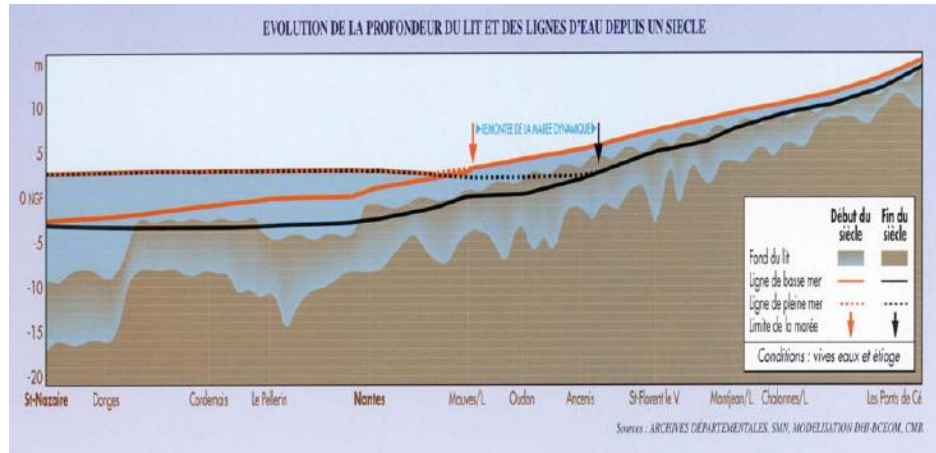


Fig. 4.14: Evolution of the river bed in the Loire River (after Sogreah, 2006).

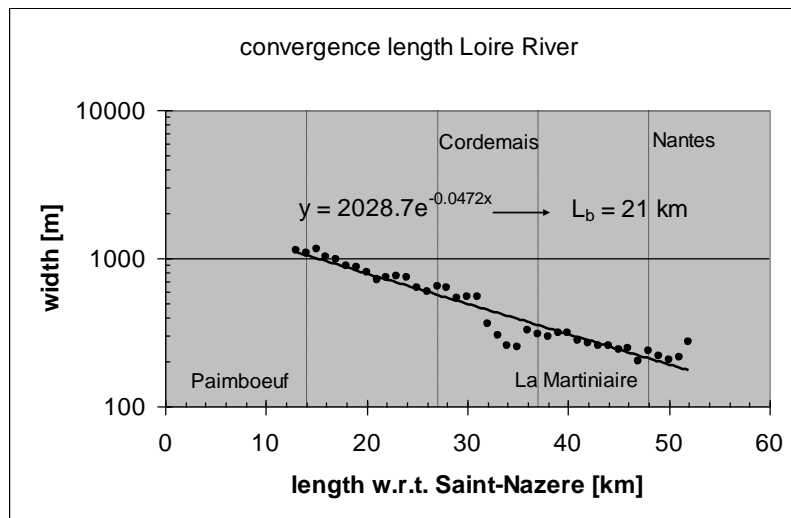


Fig. 4.15: Convergence length of Loire River; the small widths around $x = 32 - 36$ km are related to a series of groins in this stretch of the river.

The evolution in water depth is presented in Fig. 4.16, showing a profound deepening in the early 20th century, and then again in the 1960's (Sogreah, 2006). The early/mid 1900 deepening may have been the by-product of the significant narrowing of the river in the first decade of the 20th century (Fig. 4.13) and the subsequent formation of the Bassin Marée, increasing the river's tidal prism, and not created by dredging. However, we have no further data on these interventions and their implications.

The data received concern values of the thalweg with respect to chart datum CM96, which is about 3.6 m below mean sea level at the mouth of the estuary (St Nazaire). It is estimated that

MSL is about 0.3 m higher at Nantes, and the subsequent slope in MSL along the river has been accounted for in Fig. 4.16. From an analysis of the data of the present bathymetry, it is estimated that the thalweg lies about 1 – 2 m below the mean water depth (cross section divided by river width), e.g. Deltares (2011). In the following we assume that the depth of Fig. 4.16 should be raised by 1 m for the years 1900 – 1947, and with 2 m for the years thereafter – this has been accounted for in the analyses below.

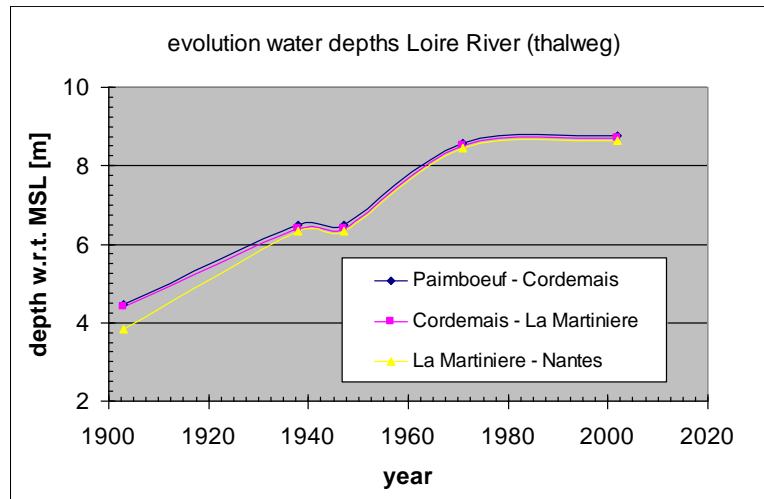


Fig. 4.16: Evolution of water depth (thalweg) with respect to local mean water level (data convergence: chart datum CM96 is 3.6 m below MSL at St Nazaire)..

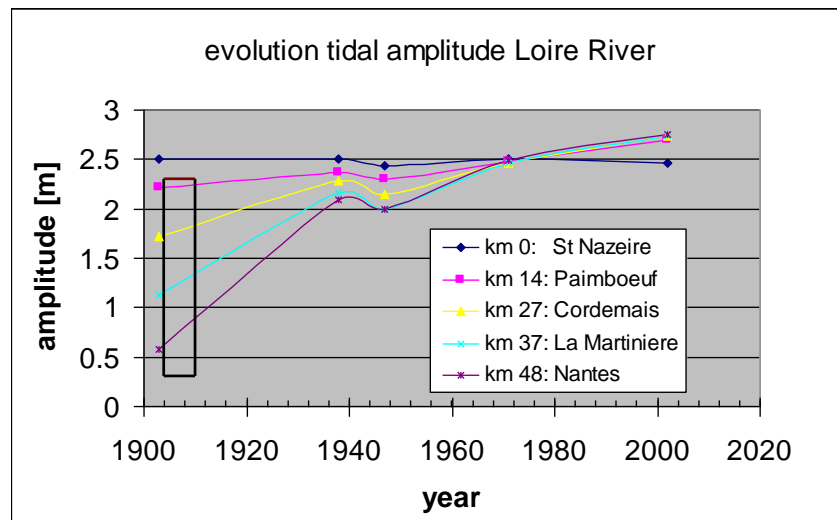


Fig. 4.17: Evolution of the tidal amplitude along the Loire River; the black box represents the period of river narrowing (e.g. Fig. 4.13).

Note that the data of Fig. 4.17 are not very accurate, nor complete, so the analysis in this section is not so accurate, in particular the developments later in the 20th century – more detailed data have been requested.

The measured evolution in tidal amplitude is presented in Fig. 4.17, showing huge amplifications of the tide in the first half of the 20th century. Though at a smaller rate, the tidal amplitude continues to increase after the 1950s; at Nantes for instance by 0.7 m. In the following we focus

on the inner river (e.g. up-estuary of Paimboeuf) and subdivide the river further to the four tidal stations along the river (Paimboeuf – Cordemais; Cordemais – La Martiniere; La Martiniere – Nantes, e.g. stretches of 13, 10 and 11 km respectively).

From the data of Fig. 4.17 the evolution of the imaginary wave number can be established, the results of which are shown in Fig. 4.18. Huge changes occurred in the early 20th century, no doubt because of the canalization of the river in that period. From 1940 onwards, $k_i \approx 0$, i.e. the tide is no longer damped in the Loire river. Note that signal is very strong and therefore consistent in the early 20th century, but thereafter becomes a bit erratic. We believe that this is due to inaccuracies of the data in general, and to ignoring the effects of the 18.6 year cycle (e.g. section 4.5).

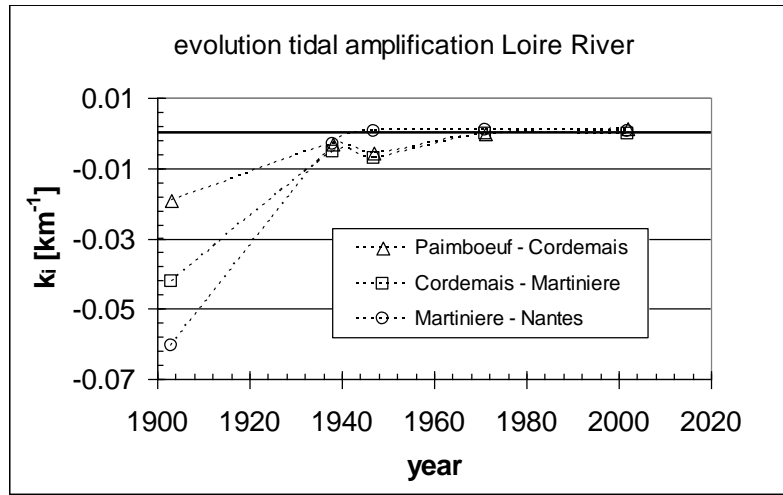


Fig. 4.18: Evolution of the imaginary wave number, based on the tidal data of Fig. 4.17.

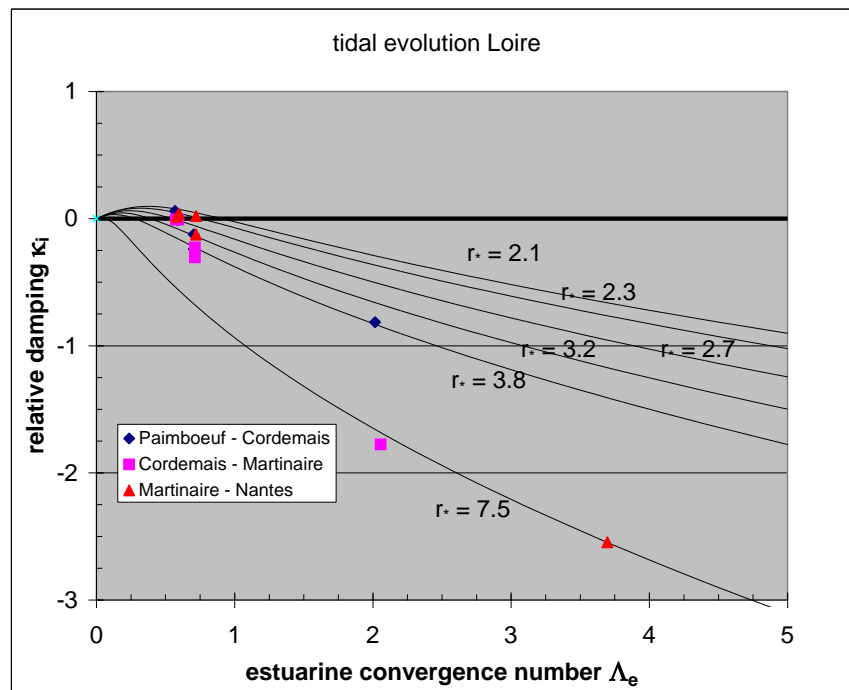


Fig. 4.19a: Tidal amplification as function of convergence number

Next, the imaginary wave numbers of Fig. 4.18 have been made dimensionless with the convergence length and plotted against the estuary convergence number Λ_e (equ. 8), the results of which are shown in Fig. 4.19a. Time evolution is diagonally from the left lower corner to the right upper corner of the figure. If we focus on the data beyond 1940 (omitting the three data points with $\Lambda_e > 2$), we obtain Fig. 4.19b.

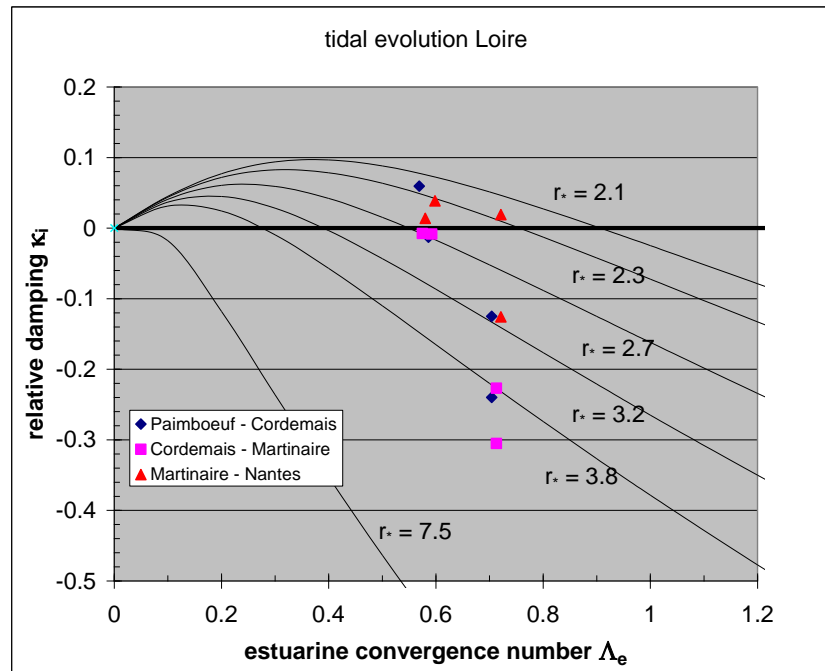


Fig. 4.19b: Tidal amplification as function of convergence number

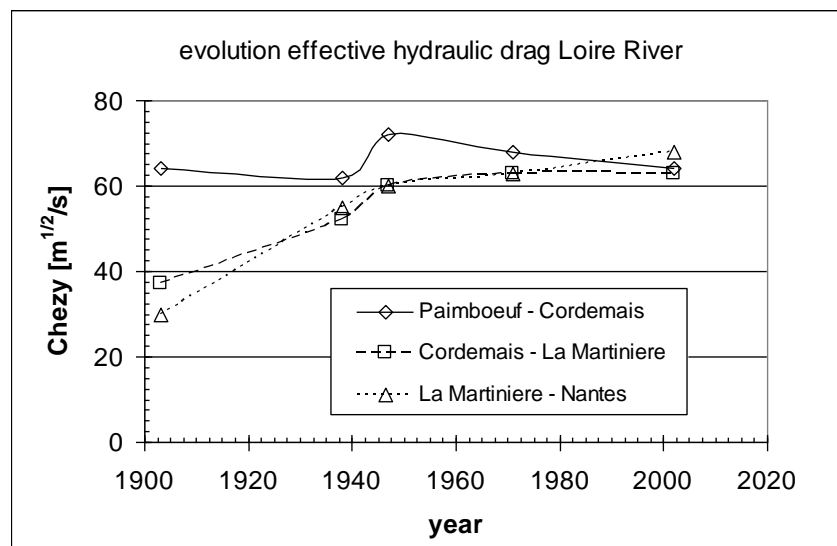


Fig. 4.20: Evolution of effective hydraulic drag Loire estuary – note that because of low accuracy of the tidal data, the error in this graph is relatively large.

Then, the linear model for an infinitely long tidal river (equ. 11) is fitted to the measured tidal damping by tuning the effective dimensionless roughness coefficient r^* to the data, e.g. Fig. 4.19a and 4.19b.

From the fitted r^* -values the effective Chézy coefficient can be obtained (equ. 8), using the observed (corrected) water depths and estimated flow velocities – for the latter, we assume that $U = 1$ m/s at the mouth of the river, and changes along the river in line with the imaginary wave number).

Fig. 4.20 shows the variation in Chézy coefficient throughout the 20th century for the three river stretches in the Loire. The Chézy coefficient in the first part of the estuary (Paimboeuf – Cordemais) has basically remained constant over time at a value between 60 and 70 $\text{m}^{1/2}/\text{s}$. However, in the upper two sections, the Chézy coefficient has increased from around 30 – 40 $\text{m}^{1/2}/\text{s}$ till 60 – 70 $\text{m}^{1/2}/\text{s}$. The major changes took place in the period before 1940, when the estuary was considerably narrowed. Note that the higher values are not very high, in particular not for a very muddy system as the Loire – fluid mud is general observed between Cordemais and Nantes (Sogreah, 2007). However, the historic data are too inaccurate to provide a better analysis of the historic development of the Loire River.

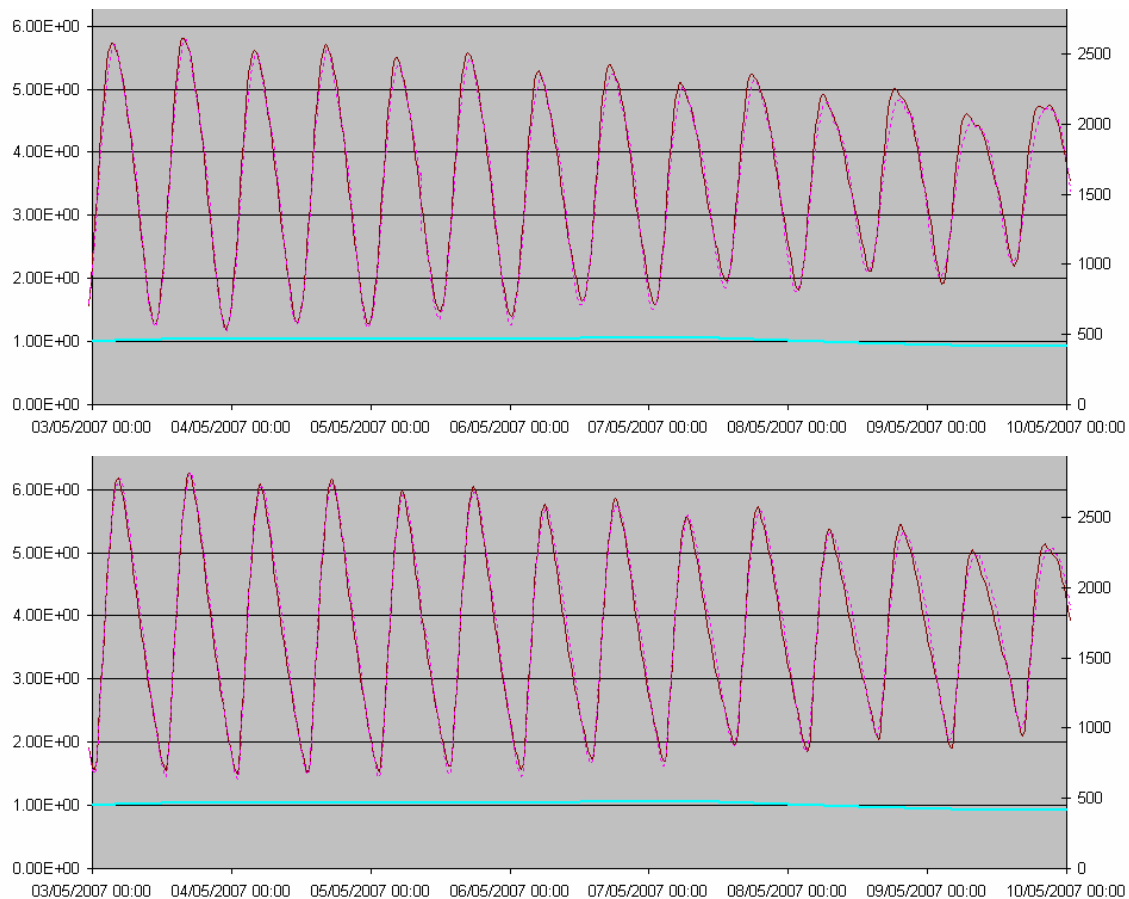


Fig. 4.21: Computed (Sogreah, 2006) tidal amplitude (vertical axis) at Donges (upper panel, km 11) and Chantenay (lower panel, km 51) showing development of steepening of the rising tide.

Because of inaccuracies in the available tidal data it is not possible to obtain proper trends in the γ -parameter with the analytical model. However, all information reveals that the tide in the Loire

has become highly asymmetrical. Whereas the tide in the mouth of the Loire River (observations at Donge, e.g. Sogreah, 2006) is almost symmetrical, near Nantes rising tide takes place in about 4 hours, and falling tide is about 50% longer. These observations are corroborated by numerical simulations by Sogreah (2006), results of which are presented in Fig. 4.21.

Note that the asymmetry in flow velocity is largely affected by the fresh water river flow, which may be large. Hence, the effects of tidal asymmetry (both in peak velocity and internal mixing, e.g. section 3.1) may be overruled by the effects of the river flow, inducing ebb dominance, flushing mud from the system.

Sogreah, 2006) reports full flushing of the fluid mud from the river at prolonged (>12 days) high river flows, e.g. around $2000 \text{ m}^3/\text{s}$, conditions which may not occur each year.

4.3 The Elbe River

The Elbe River originates in the Karkonosze mountains of the Czech Republic and flows through Germany over 630 km passing the city of Hamburg (largest German seaport) at about 110 km from the mouth at Cuxhaven (North Sea). The mean annual fresh water discharge is about $700 \text{ m}^3/\text{s}$ with a variation range of 200 to $3600 \text{ m}^3/\text{s}$. The mouth of the estuary is characterized by a narrow deep channel and a very wide tidal flood plain up to 2 m above LAT (Hakensand, Medem sand, Norder Grunde), see also Admiralty Chart No. 3261. The total width of the mouth is about 15 km. The width of the deep channel is in the range of 1500 to 3000 m. The area below LAT of the deep channel at the mouth is in the range of about 20000 to 40000 m^2 . Fig. 4.22 shows a plan view of the river.

Fig. 4.23 presents the evolution of the tidal range along the Elbe River, as presented by Weilbeer and Klöpper (2011), showing a considerable amplification of the tide upstream of $\text{kmr} \sim 670/680$ after the 1970's. Initially, i.e. in the beginning of the century, the tide was damped over the entire estuary.

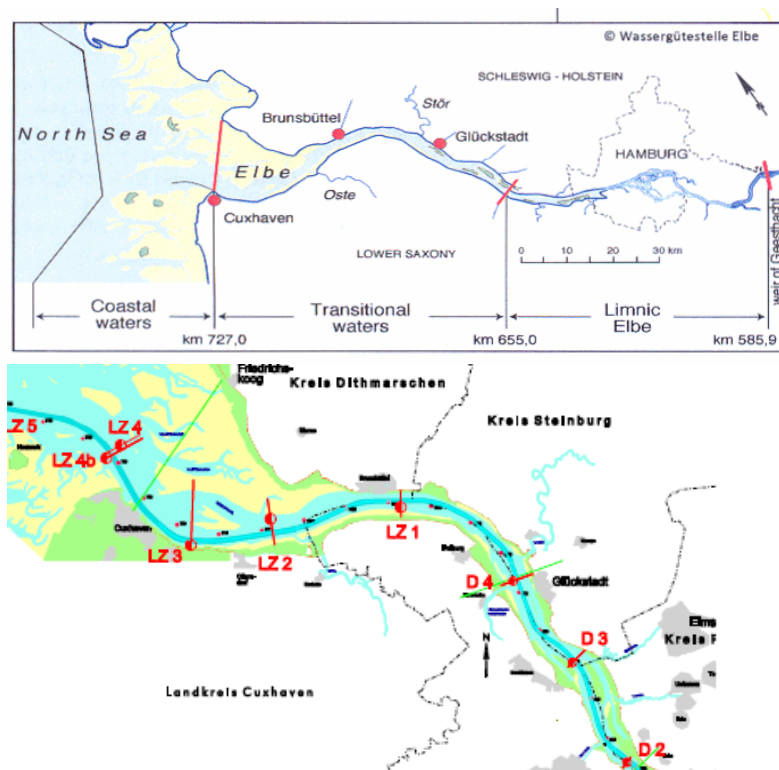


Fig. 4.22: Plan view of lower Elbe river from Hamburg ($\text{kmr} \sim 620$) to Cuxhafen ($\text{kmr} 724$) and kmr – co-ordinates along the river.

Fig. 4.23 suggests a discontinuity in tidal response around $\text{kmr} 680$. This is further substantiated by the longitudinal variation in flow carrying cross section, presented in Fig. 4.24, showing a substantial kink in this variation. In fact, the cross section in the outer part of the estuary is almost constant, whereas the inner part follows a more exponential distribution. It is postulated that this fairly uncommon distribution is the result of human interventions, in particular with respect to embanking and reclamation.

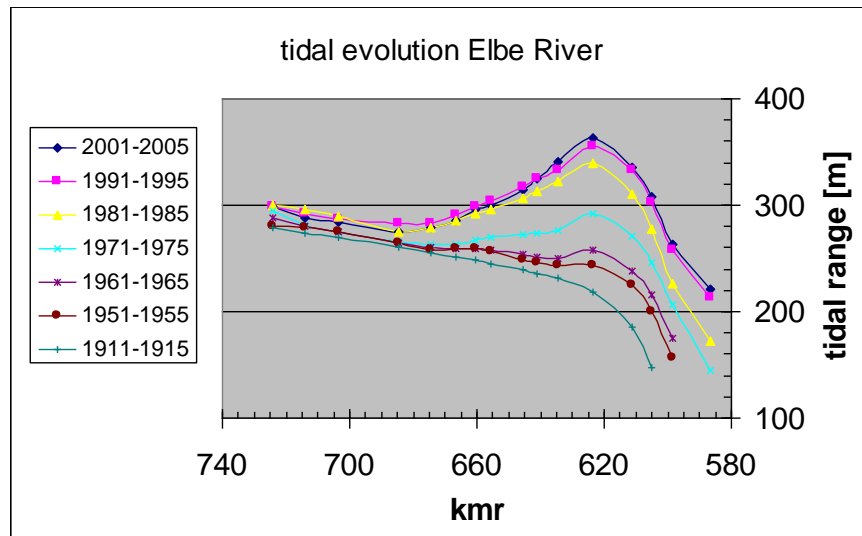


Fig. 4.23: Tidal amplification as function along Elbe River (after Weilbeer and Klöpper, 2011)

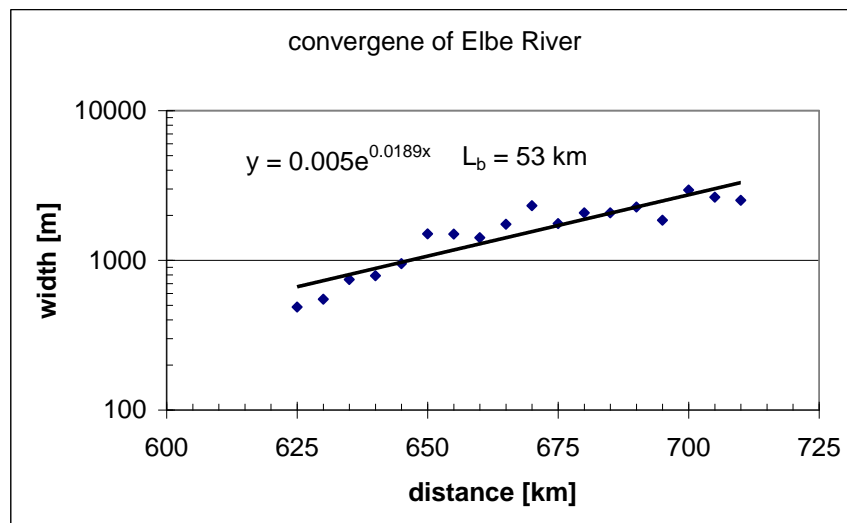


Fig. 4.24: Longitudinal variation of flow-carrying cross section with discontinuity at kmr 670 (after Portal Tidelbe, 1999). The overall convergence length measures 53 km.

In the following, we distinguish between the inner and outer estuary, with their transition around kmr 680. Because of a lack of sufficiently detailed data, we treat the outer and inner estuary as two different, but homogeneous parts of the river. Then, based on the data of Fig. 4.23, the variation in the imaginary wave number k_i can be assessed for the two river parts, as shown in Fig. 4.25. Fig. 4.25 also contains information on the design depth of the fairway in the Elbe River, and the years in which the deepening were realized. Note that we do not have data before 1940, though the Portal Tidelbe (chapter 3.3 Veränderungen am Flusz) states that in 1859 the fairway was deepened to -5.9 m, whereas from 1910 a depth of 8 – 10 m have been maintained.

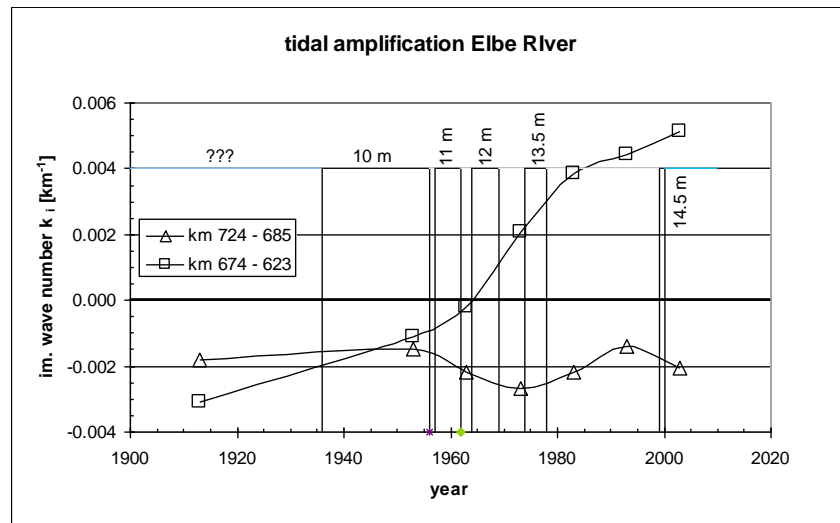


Fig. 4.25: Variation of imaginary wave number k_i ($a(x) = a_0 \exp\{k_i x\}$) in outer and inner estuary and time windows with targeted fairway design depths.

In our analyses below, we use the design depths within the time windows as indicated in Fig. 4.25, and use k_i values within these windows by interpolation. Note that if all cross sections would have been available, our analyses could be carried out from tidal station to tidal station.

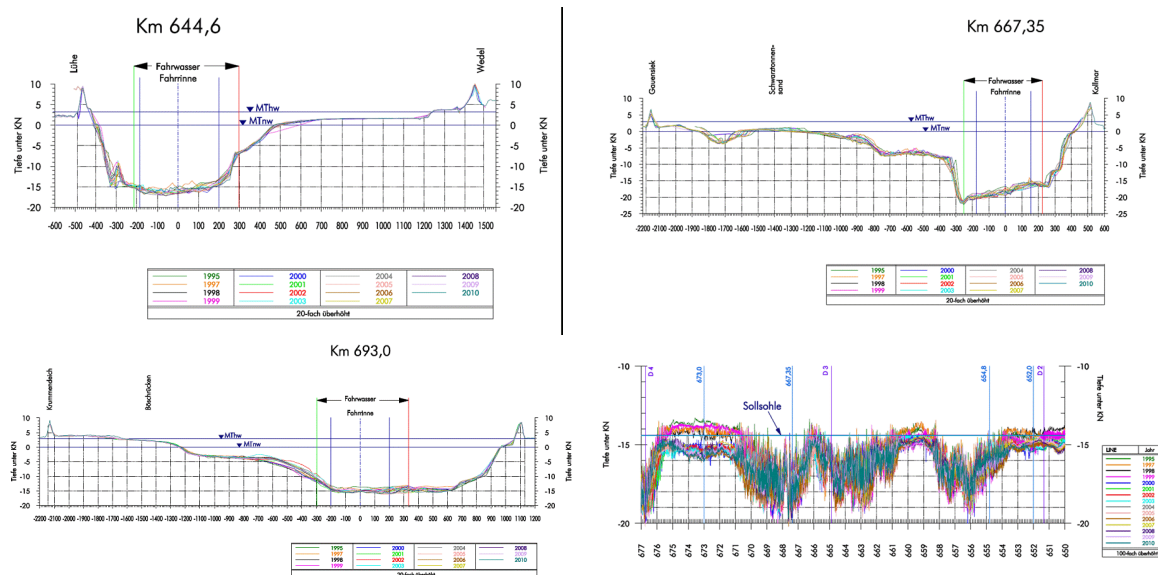


Fig. 4.26: Examples of cross sections in the Elbe River and one longitudinal section (between kmr 650 and 677) (after Portal Tideelbe, 1999)

Fig's 4.24 and 4.26 show that the river's cross section increases in seaward direction. Remember that in our analysis it is not the water depth itself that plays a role, but the flow-carrying cross section divided by the total width (e.g. A_c/b_{tot}) is important. Deepening of the fairway in the inner estuary therefore has a larger effect on the total cross section than in the outer estuary. We have used the available cross sections to compute changes in these cross sections in response to deepening of the fairway. Then, if we assume that the width of the flow-carrying cross section did

not change over time, we can construct the evolution in mean depth for the outer and inner estuary, e.g. Fig. 4.27.

Fig. 4.27 also depicts the development of the depth of the fairway showing a profound step in depth near around Hamburg, in particular in later years (e.g. Kappenberg and Fanger, 2007).

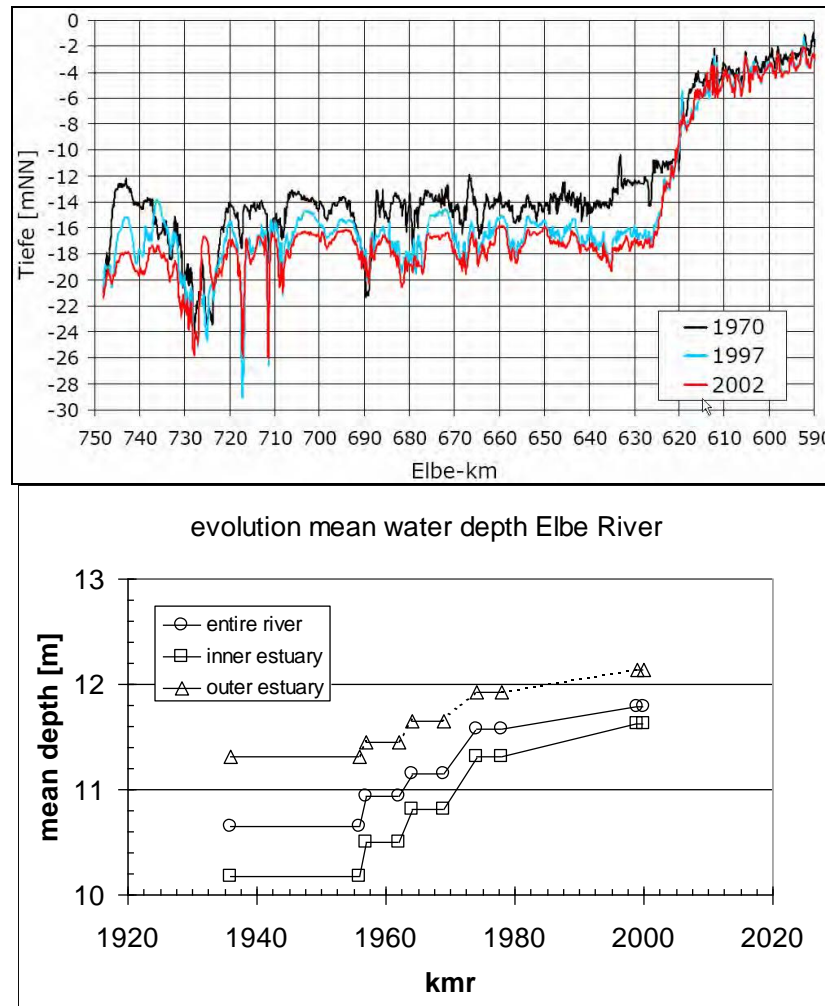


Fig. 4.27: Evolution of mean water depth along Elbe River. Fairway (upper panel) and mean depth in outer and inner estuary.

Fig. 4.28 shows the longitudinal variation in width of the flow-carrying cross section along the Elbe River, based on data provided by BAW (2012). The mean convergence length amounts to about 53 km (Fig. 4.24), though the data show large scatter. However, as suggested by Fig. 4.24, and the data of Fig. 4.28, the convergence length in the outer estuary is much larger than in the inner estuary – in the following we will use two different lengths, i.e. 93 and 30 km in the outer and inner estuary, respectively. In the inner estuary, the intertidal area seems to amount to about 20% and in the outer estuary about 60% of the width of the flow-carrying cross section (e.g. $b^* = 1.2$ and 1.6 , respectively). Note that from an inspection of Google Earth images, these numbers are likely to be on the high side. A detailed analysis of the river's hypsometry is required to obtain more accurate data. Moreover, we have no information on how the intertidal area changed over time.

Because of the large scatter in the data of Fig. 4.24, the convergence length of the inner and outer estuary are fairly sensitive to the location of the kind in L_b ; a few km further up-estuary or down-estuary makes a considerable difference. However, L_b for inner and outer estuary are quite different, and the overall conclusions of the analysis in this section appear to be not too dependent on the choice of the location of L_b -kink (results of sensitivity analyses not presented here).

Using the various parameters, the time-variations in imaginary wave number k_i can be made dimensionless with the convergence length L_b , and plotted against time-variations in river bathymetry, i.e. the estuarine convergence number Λ_e . The results are shown in Fig. 4.29. Note that variations in the outer estuary are fairly small, owing to the limited interventions with respect to cross sectional area. The variations in the inner estuary are much larger, though, and in agreement with the evolution of the tide presented in Fig. 4.23.

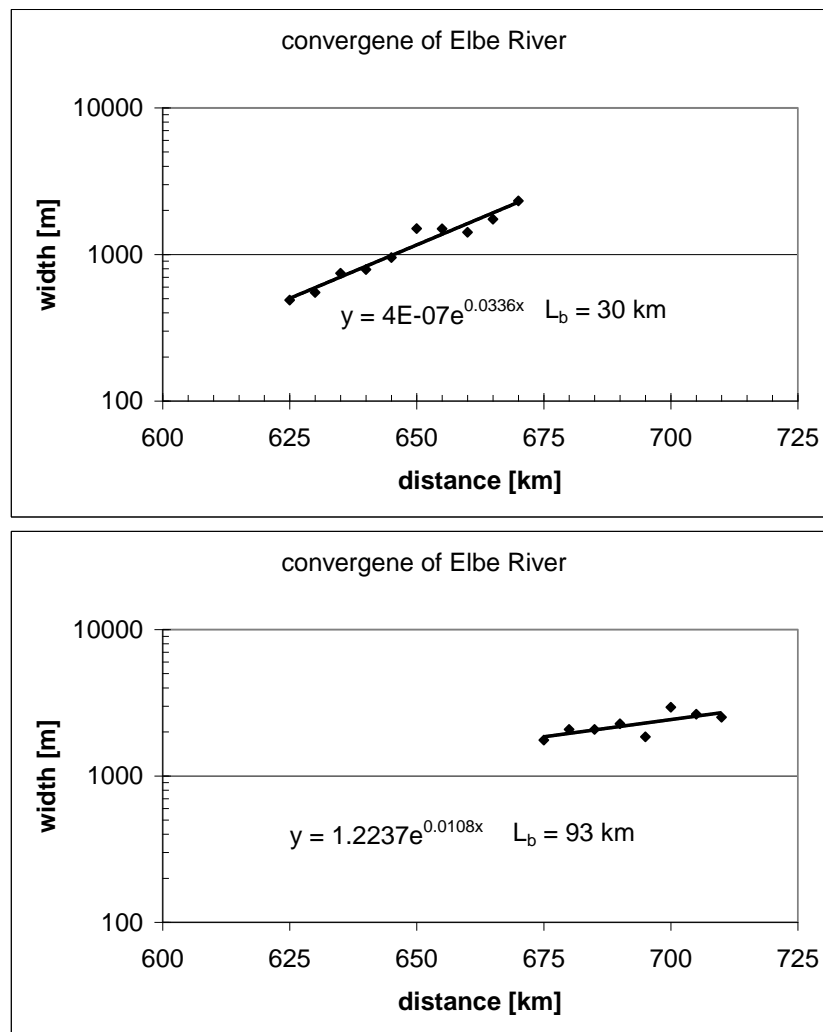


Fig. 4.28: Total width and width of flow-carrying cross section of Elbe River; the intertidal area in the outer estuary amounts to about 50% and in the inner estuary to about 30% (data BAW).

Next, the analytical solution to the linear tidal model has been added to Fig. 4.29, and again the dimensionless roughness parameter r_* is used as a calibration parameter. The results show that,

for the given L_b and h values, the data in the inner estuary can be described with roughness values ranging from $r_* = 2.8$ for the pre-1950 situation to $r_* = 0.9$ for the post-2000 conditions. Data for the outer estuary can be described with roughness values close to $r_* = 0.9$.

Note that smaller variations over time in r_* for the inner estuary are possible only when we assume either one of the following possibilities, or a combination of these:

- much smaller values of L_b (half or so) – this is not a very likely assumption,
- profound changes over time in convergence length L_b
- profound changes over time in intertidal area.

As said, we presume that both the convergence length and intertidal area have changed over time by reclamation works and natural sedimentation.

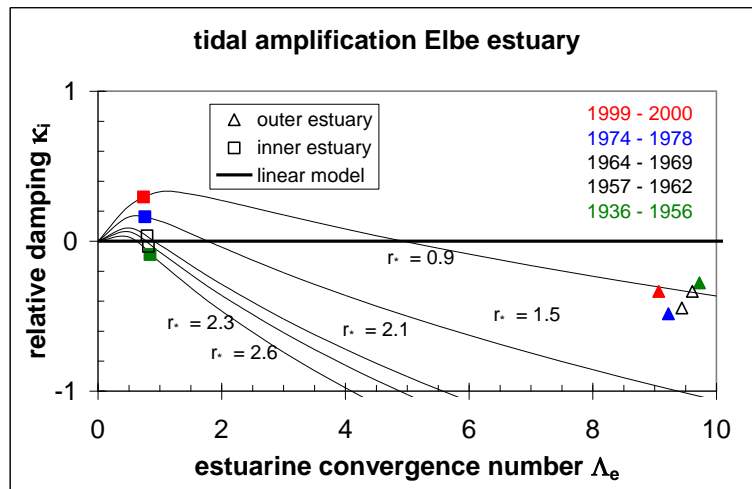


Fig. 4.29: Evolution of dimensionless tidal damping in Elbe River; the five data points and lines for the inner estuary represent the various fairway depths within the five time windows inserted in the graph (e.g. Fig. 4.25).

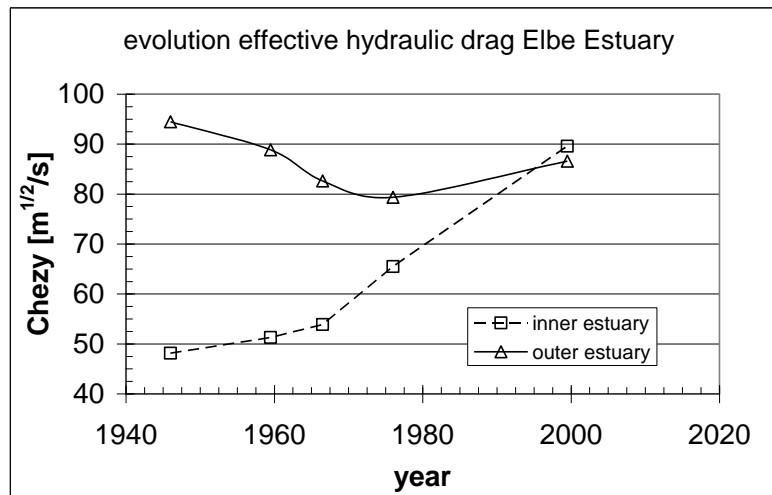


Fig. 4.30: Variation in effective hydraulic drag along the Elbe River as a result of human interventions.

From the dimensionless roughness parameter r_s , a Chézy coefficient C can be established, assuming that the damping in flow velocity is identical to the damping in tidal amplitude (as is assumed in our linear model). Fig. 4.30 shows that in the outer estuary C remains around $80 \text{ m}^{1/2}/\text{s}$ over time. However, in the inner estuary the results suggest that over time, the river becomes very smooth, up to $C \approx 90 \text{ m}^{1/2}/\text{s}$ in the 2000s.

The high Chézy-values in the outer estuary are in agreement with the high SPM-values in this part of the river, and the very muddy intertidal areas (e.g. Fig. 4.31).

Another effect which may have reduced the effective hydraulic drag is the continuous off-topping of the bed forms in the Elbe River by maintenance dredging. The longitudinal profile of the river in the lower right panel of Fig. 4.26 reveals considerable bed forms of a few meter height. Such bed forms were already described by Nasner (1974), reporting dune heights of 1 – 3 m, at lengths of 50 – 100 m, hence fairly steep. Such steep bed forms induce large effective hydraulic drag (e.g. Van Rijn, 1990). These bed forms have decreased by about 1 dm or so, and the reduction in effective hydraulic drag should therefore have been fairly limited.

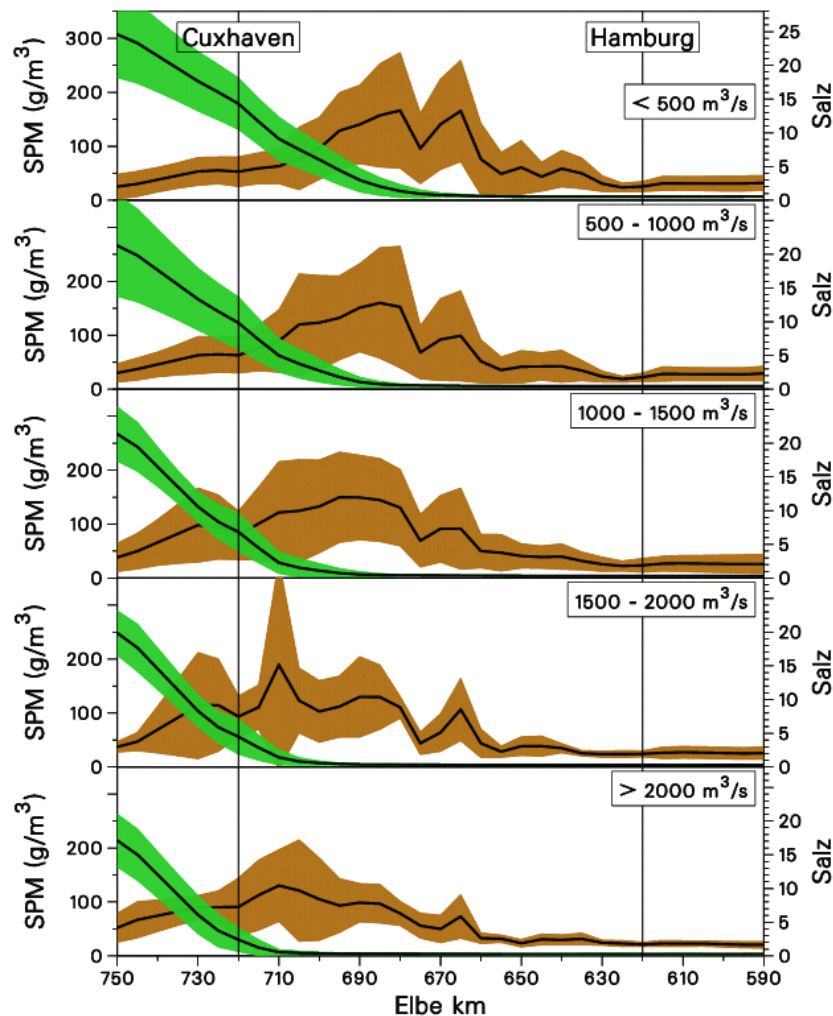


Fig. 4.31: Variation in SPM-concentrations and salinity intrusion as a function of river flow (after Kappenberg and Fanger, 2007). Down-estuary of kmr 670/680, SPM values are high, in agreement with high Chézy-values; up-estuary, SPM-values are low.

Finally, it has to be noted that in our analytical, linear model, the effect of reflections of the tidal wave have not been included. End of the 1950's, the Geesthacht weir was erected, hence arresting the tidal limit at about kmr 585. Furthermore, a distinct step in bed level around the port of Hamburg developed over time, as hardly any deepening took place up-estuary of Hamburg (Boelich and Strotmann, 2008). This is depicted in Fig. 4.27. A zero-order assessment of this step in bed level was made by assuming full reflection at kmr 619 (Hamburg). Furthermore, the analysis of the data suggest that in the course of the 1970s, the convergence of the inner estuary has been decreased by river works. Therefore, we present results for $L_b = 30$ km and 40 km, e.g. Fig. 4.32. All simulations have been carried out with $r = 0.003$ m/s (sandy riverbed).

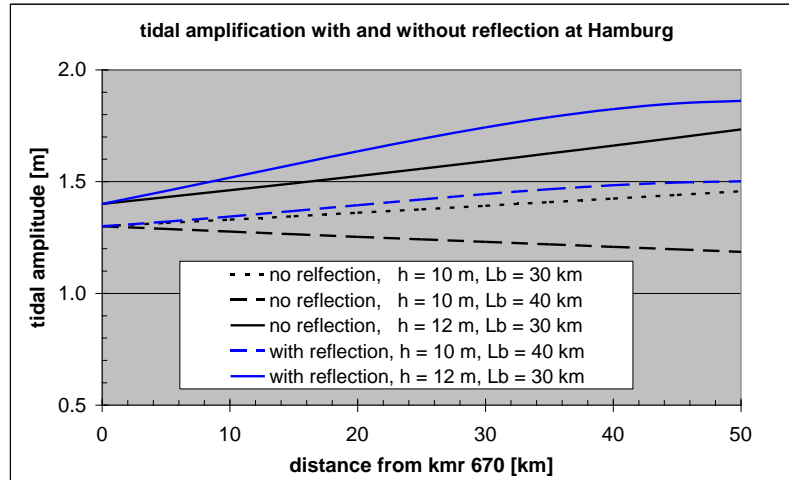


Fig. 4.32: Computation of tidal amplitude for pre-1970 conditions ($L_b = 40$ km, broken line) and post-1970 conditions ($L_b = 30$ km, full line).

From Fig. 4.32, the following conclusions can be drawn:

- The amplification in the upper Elbe estuary is very sensitive to the convergence length L_b – for $L_b = 30$ km, the linear model (only incoming wave) predicts amplification, whereas for $L_b = 40$ km, damping is predicted.
- For full reflection at kmr 619, the tide always amplifies – increasing the convergence length does not have too much influence (results not shown). Only a large increase in roughness (the r -parameter) reduces the amplification considerably.
- The effect of amplification increases by a few dm's upon deepening of the Elbe.

From these observations we may conclude that the increase in effective bed roughness in the upper estuary (Fig. 4.30) is probably overestimated, as part of the amplification should be attributed to reflections. However, it is not likely that full reflection takes place at Hamburg. Moreover, these results suggest that the amplification of the tide in the (upper-)Elbe is quite sensitive to the bathymetry and geometry of the river.

Next, the travel time of high water between Cuxhafen and Hetlingen (kmr 647, e.g. Fig. 4.33 upper panel) is computed using equ. (17). Computed and measured travel time are compared in Fig. 4.33, showing that the linear model underpredicts the observed travel time by about 10%. Analysis of the sensitivity of the travel time to model parameters showed that the travel time is sensitive in particular to the convergence length, more than to the effective roughness. Hence, this is another indication that the geometrical features of the Elbe are not known sufficiently well.

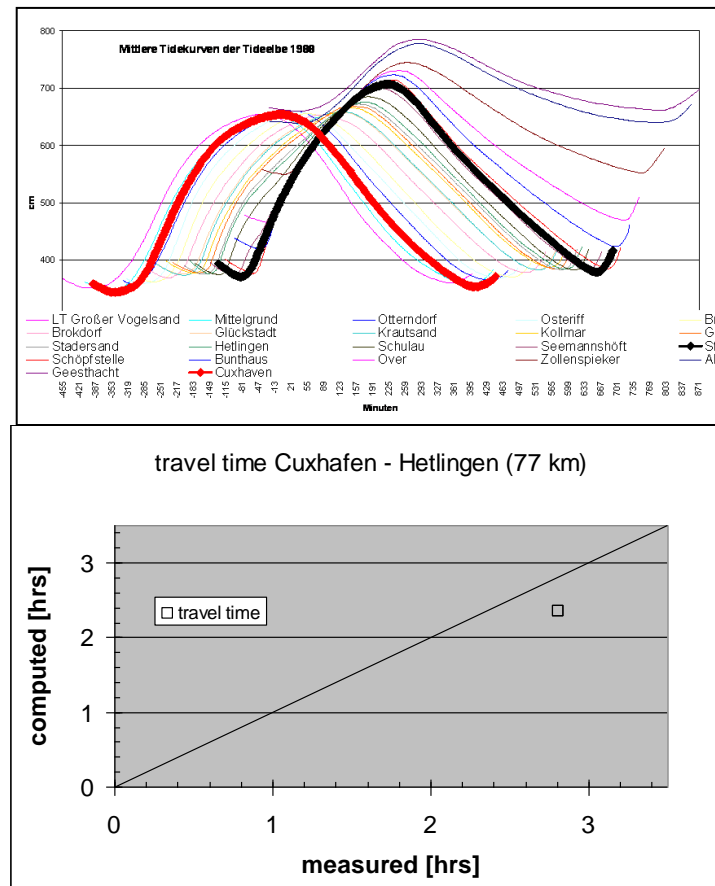


Fig. 4.33: Travel time high water in Elbe River; upper panel: observations in 1988; lower panel: prediction by linear model

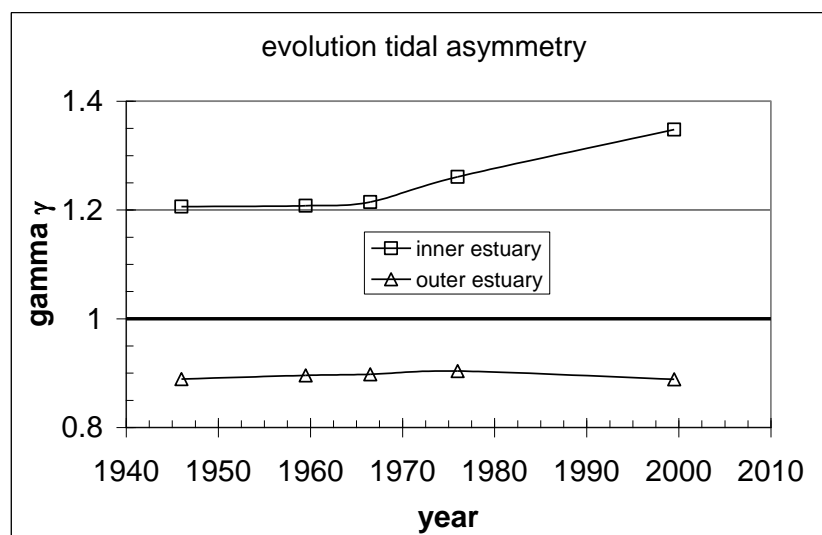


Fig. 4.34: Temporal variations in tidal asymmetry parameter γ in inner and outer estuary.

Finally, variations in tidal asymmetry have been assessed from variations in the γ -parameter, i.e. the ratio of the wave celerity at high and at low water, in which the actually measured variations

in tidal amplitude have been used, in conjunction with the values for river depth h , convergence length L_b , roughness r^* and intertidal area b^* , established and used above. Fig. 4.34 suggests that the outer estuary remained ebb-dominant over time, whereas the inner estuary remained flood dominant over time. These conclusions are more or less sustained with measurements of the current velocity in Fig. 4.35, showing that in the outer estuary, the flow is slightly flood dominant, but in the inner estuary flood-dominance is more pronounced. Note that the underestimation of flood dominance (in the outer estuary) is likely the result of erroneous values (too large) for the intertidal area b^* - see also Boelich and Strotmann (2008).

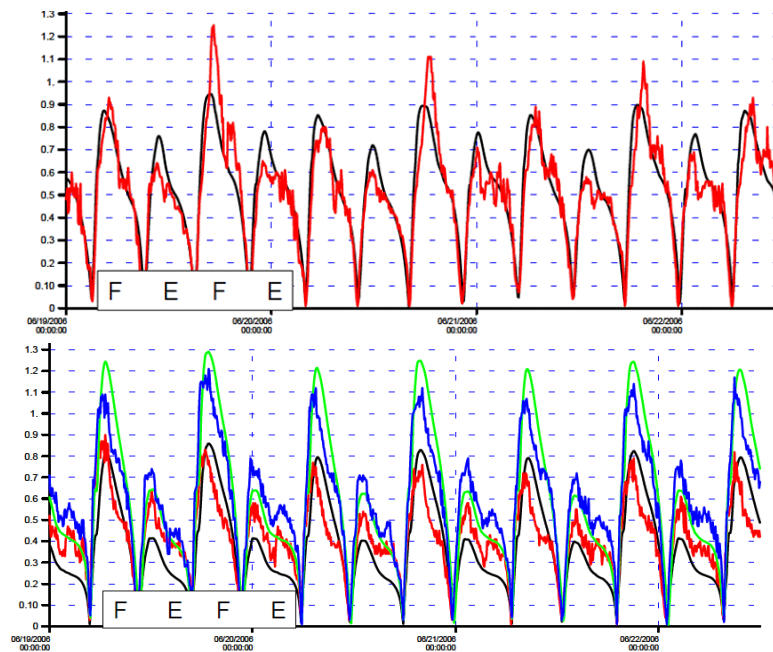


Fig. 4.35: Measured tidal asymmetry along Elbe River; upper panel: near Brunsbuttel; lower panel: near Schulau (after BAW, 2011)

It is to be noted that the flood dominance in the inner estuary follows a subtle interplay from a decrease in γ by increased river depths, and an increase by tidal amplification. This would imply that if the river were sub-divided into more sub-sections, we would expect a larger increase in flood-dominance further upstream, near the port of Hamburg. As the riverine turbidity maximum (RTM) is governed by tidal asymmetry and river-induced flushing, this would imply that:

- the ETM moves upstream with decreasing river flow – indeed it has been observed that dredging needs in the Port of Hamburg increase in years with low river flows (Haar, 1994).
- over time, the ETM would have moved in upstream direction – unfortunately, we have no information to confirm.

Our analysis of the data on the Elbe River suggest that:

1. The tide in the lower estuary (kmr 720 – 670) is largely influenced by a large intertidal area, large convergence length and small effective hydraulic drag. Tidal amplification over time remained relatively small.
2. The analysis with the linear model (infinitely long river) suggests a sharp increase in Chézy coefficient in the inner estuary after 1970, suggesting a sharp increase in SPM in

- the river. This is, however, not in agreement with the SPM data, which show relatively low SPM-concentrations in this part of the river.
3. The Elbe river depicts a large step in water depth around Hamburg, which becomes more pronounced over time (with deepening of the river). This step should induce reflections of the tidal wave. Our model simulations, however, suggest that this can be only a partial reflection.
 4. We have no data on the convergence of the river prior to 1970. However, the analysis with the linear model suggests that the river's convergence has increased (Lb decreased).
 5. The analyses indicate that the tidal propagation in the upper estuary is very sensitive to the geometry and bathymetry of the river. This was confirmed by Weilbeer (2013). This sensitivity itself suggest an important effect of reflections of the tidal wave, either at the step in bed level around Hamburg, or otherwise.

However, these conclusions are based on a limited series of data, and further substantiation is possible only upon further analysis. We recommend the following:

- Make harmonic analyses of the historical tidal data at the various tidal stations along the river (analysis should be done on M2 and M4 tidal component).
- Make a proper analysis of the historic development of the river's cross sections, preferably in the form of hypsometric curves.
- Make a detailed analysis of the development of convergence length and intertidal areas.
- Analyze changes in bed forms, in particular variations in the steepness of dunes.
- Analyze the changes in tidal amplitude in relation to geometrical changes along the river, focusing on all sub-sections defined by the existing tidal stations.
- Apply a (one-dimensional) numerical model to study the response of deepening, reclamations, the step in bed level, Geesthacht weir and reduction in effective hydraulic drag in a non-linear model, including possible reflections of the tidal wave.

4.4 The Weser estuary

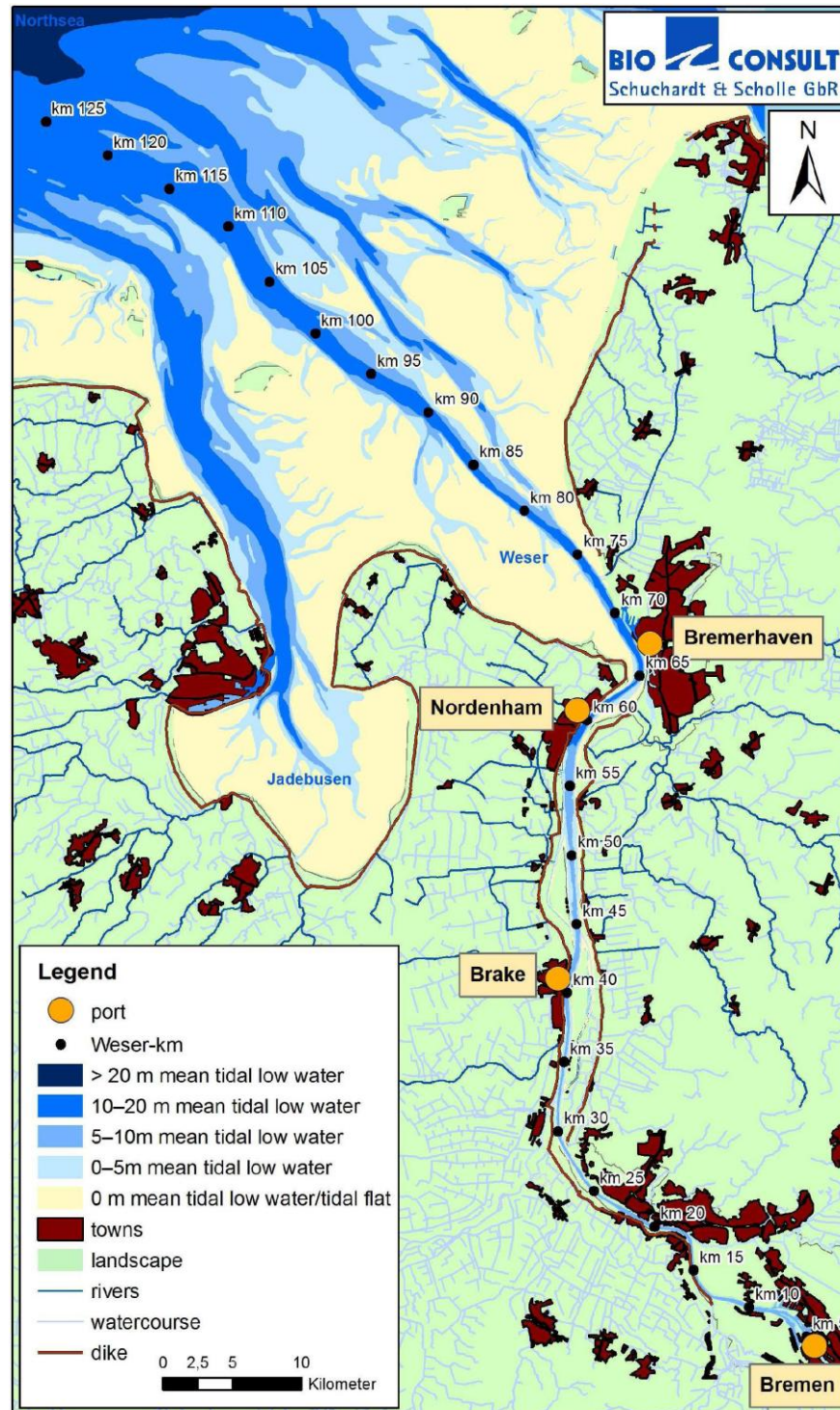


Fig. 4.36: Overview of Weser estuary

We are in the process of acquiring data for the Weser River for an analysis similar to elsewhere in this report. Hence, no results yet, though the enormous deepening of the river in the 20th century

suggests problems similar to the other rivers analyzed in Chapter 4 – indeed the graph of Fig. 4.35 confirms this expectation.

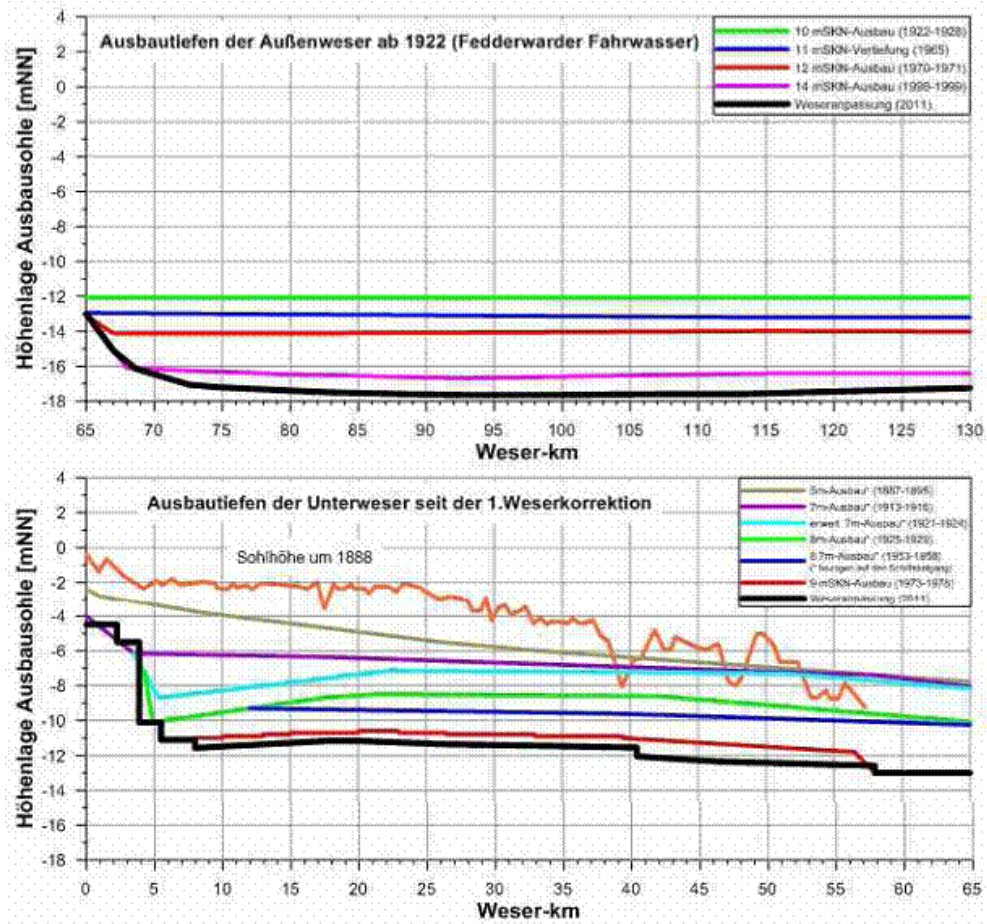


Fig. 4.37: Evolution of water depth along Weser River.

The data are from B. Schuchardt and S. Beilfuss (2012).

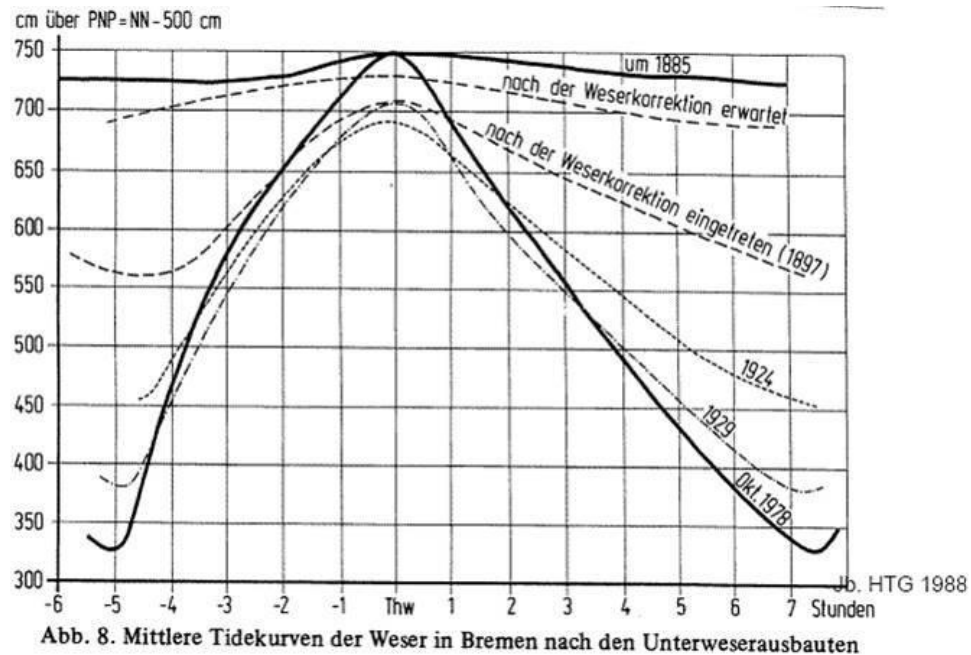


Abb. 8. Mittlere Tidekurven der Weser in Bremen nach den Unterweserausbauten

Fig. 4.38: Example of tidal amplification in Bremen over time

Currently, we have no further data available, and we cannot analyze the developments in the Weser River. Yet, the amplifications are so large that we decided to include the results in this report.

4.5 The Upper Sea Scheldt River (Boven Zeeschelde)

Fig. 4.39 shows an overview of the Scheldt estuary from its mouth near Flushing (Vlissingen) to Ghent with indication of the various tidal stations treated in this report (see also Table 4.1, e.g. IMDC, 2012). Further details, including the km-indications are given in Fig. 4.40.

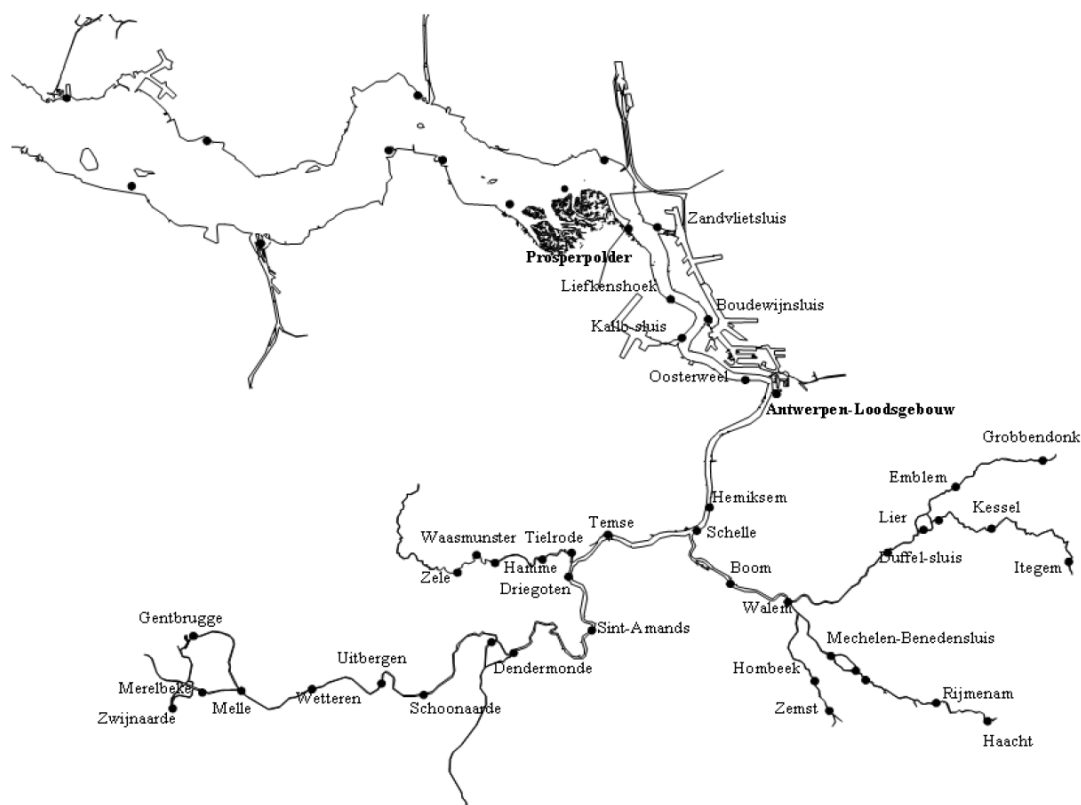


Fig. 4.39: The Scheldt estuary from Flushing to Ghent with the various tidal stations.

Table 4.1: Summary of tidal stations along Sea Scheldt

Name	km from Schelle	km from Vlissingen
Schelle	0	91.2
Temse	7.5	98.7
Tielrode	11.9	103.1
Sint Amands	17.8	108.8
Dendermonde	30.6	121.8
Schoonaarde	41.7	132.6
Uitbergen	47.0	138.2
Wetteren	53.8	145.6
Melle	60.0	150.8

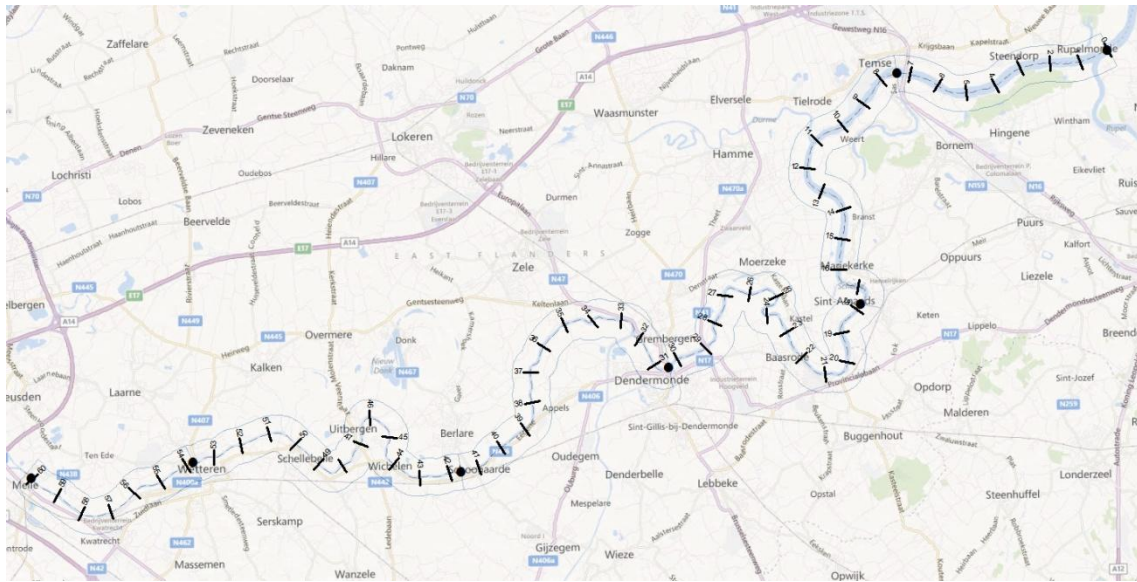


Fig. 4.40: Overview of Upper Sea Scheldt (Boven Zeeschelde) from Schelle (upper right corner) to Melle (lower left corner).

Tidal data for the entire Scheldt estuary are available from before 1900. Kuijper (2012) corrected these data for the 18.6 year cycle, the results of which are shown in Fig. 4.41a. In the following, we focus on the Upper Sea Scheldt, i.e. up-estuary from Schelle. For an analysis of the time evolution of the entire estuary, the reader is referred to Kuijper (2012, Western Scheldt) and Plancke (2012, for Sea Scheldt). To allow further analysis, missing data points have been filled in by interpolation from the available time and spatial series, e.g. Fig. 4.41b.³⁾

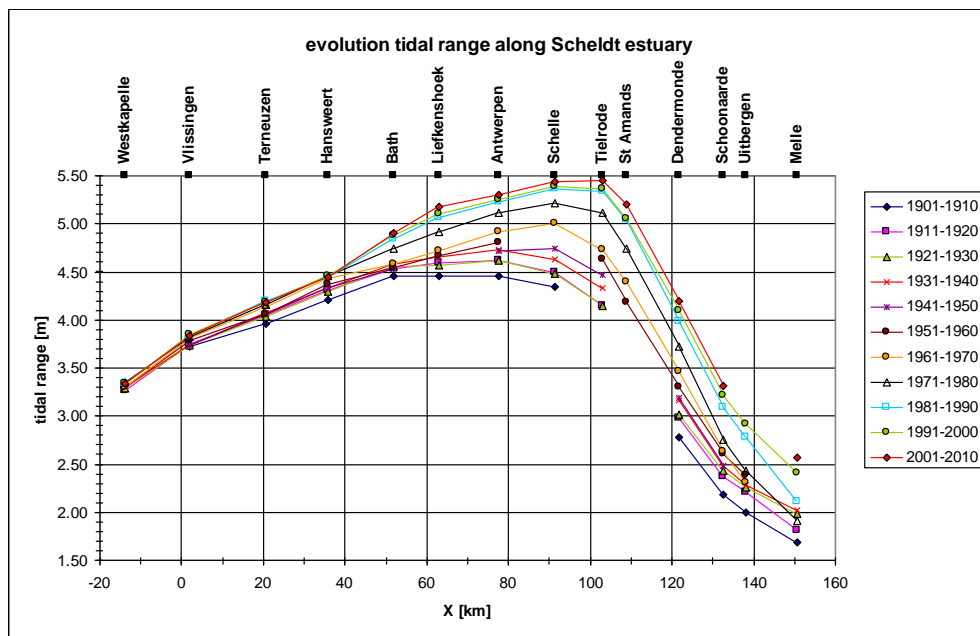


Fig. 4.41a: Evolution of tidal range along Scheldt estuary corrected for 18.6 year cycle.

³⁾ Note that no consistent analyses could be made using the original data, obtained by averaging and grouping over decades – clear trends in tidal amplification and reflection could not be obtained.

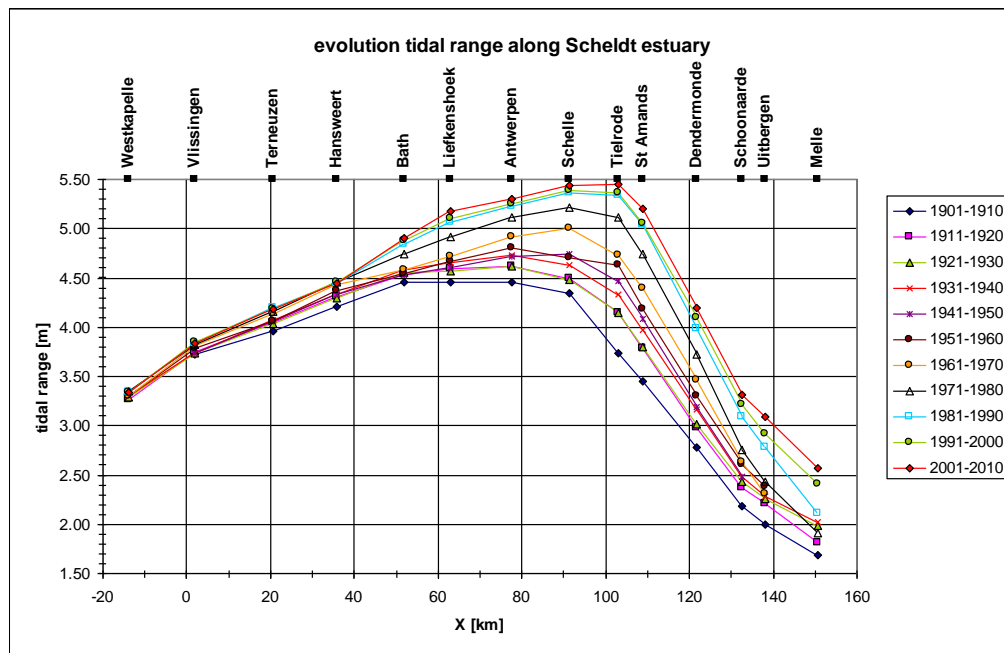


Fig. 4.41b: Same as Fig. 4.41a, but missing data added by interpolation..

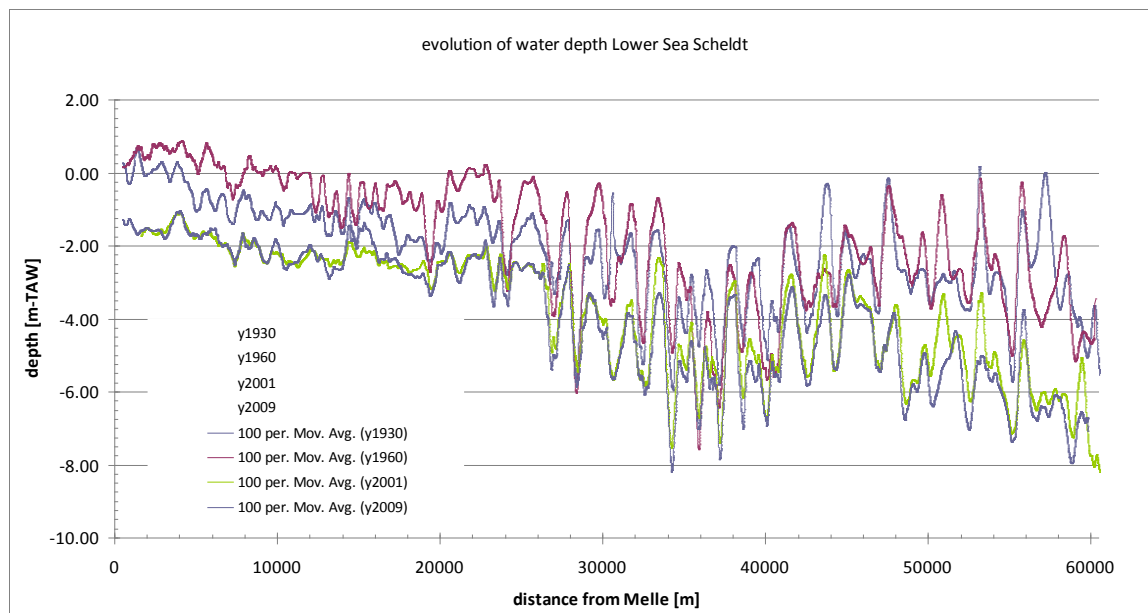


Fig. 4.42: Evolution of water depth Upper Sea Scheldt w.r.t. TAW chart datum .

Van Braeckel et al. (2006) summarize modifications in the Scheldt estuary. The majority of the engineering works in the Upper Sea Scheldt took place before 1900, e.g. rectifications of the river and embanking intertidal areas. In the early 1900s (1900 – 1930) parts of the river were normalized, and later rectifications took place in the Durme. In the 1970s, the river deepened by 1.5 – 2 m, e.g. Fig. 4.42, though no engineering works are reported. Possibly, this deepening was the morphodynamic response to engineering works further down-estuary, such as sand-mining and deepening and widening of Western-Scheldt and/or Lower Sea Scheldt. Also deepening and

widening of the Scheldt estuary down-estuary of Antwerp in the second half of the 20th century, and early 21st century had an effect on the tidal evolution, as discussed below (see also Kuijper, 2012).

The evolution of the water depth in the Upper Sea Scheldt is further elaborated in Fig. 4.43 showing the water depth with respect to local mean water level, based on data from IMDC (2012). The water depth in Fig. 4.43 is obtained from dividing the flow-carrying cross section by the width of the river, and then averaging over the river sections in between the tidal stations.

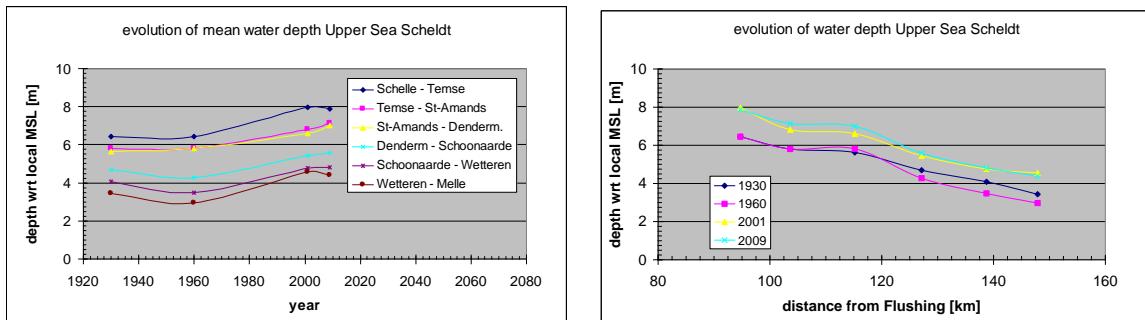


Fig. 4.43: Evolution of mean water depth between the various tidal stations along the Upper Sea Scheldt.

At the head of the estuary, around Ghent, a number of engineering works were carried out between 1950 and 1970. These works consisted of the creation of a new channel of about 4 km length with a shipping lock for access to Ghent. Between around 1960 – 1970 the Upper Sea Scheldt became deeper, and the old northern arm of the Upper Sea Scheldt has silted up largely.

The old Scheldt branch measured about 8.4 km from Melle tidal station to the weir in Ghent, whereas the new branch measures about 7.2 km.



Fig. 4.44: Overview engineering works at head of Upper Sea Scheldt (Meersschaut, pers. com).

The convergence length of the Upper Sea Scheldt is plotted in Fig. 4.45, showing an exponential behavior with a mean value of about 31 km, and little variation since 1930. Note that the river rectifications in the late 19th century must have reduced this convergence length by about 5 km.

Fig. 4.45 suggests a kink in the river's convergence between Dendermonde and Schoonaarde, and the data have therefore been replotted in Fig. 4.46 showing a significant discontinuity in L_b . However, no clear time signal can be identified.

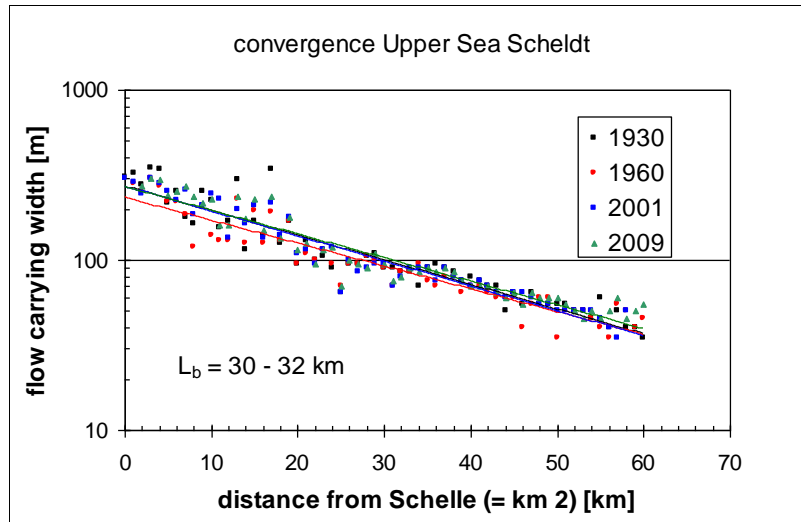


Fig. 4.45: Convergence length of Upper Sea Scheldt shows little variation since 1930.

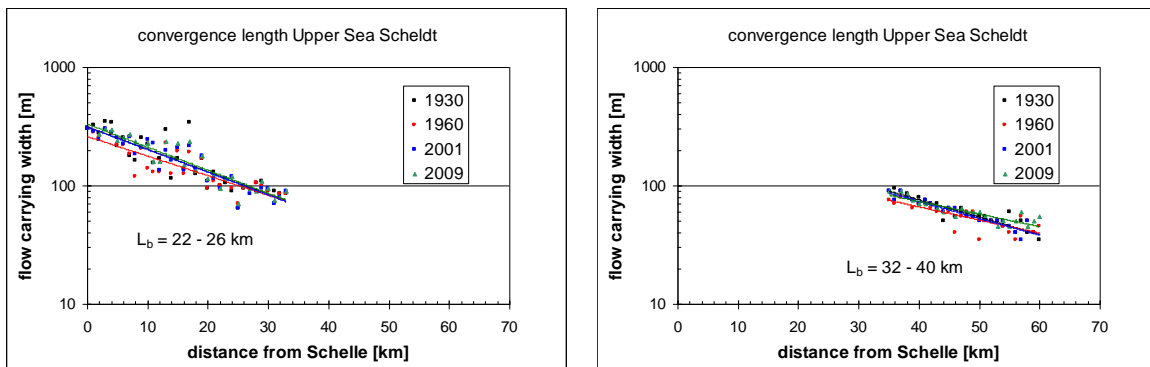


Fig. 4.46: Convergence length of Upper Sea Scheldt for lower part (up to km 34) and upper part (from km 34); km 34 is halfway Dendermonde and Schoonaarde.

Fig. 4.47 presents the total width of the Sea Scheldt River and its flow carrying width, again for the lower and upper reaches. The total width is defined as the width of the river at the edges of its salt marshes. Hence, this total width is expected to be a bit too large, as in our tidal analysis, the mean high water level is relevant (see comment below). From a linear fit, we define a mean value for b_* for the upper and lower reaches.

Fig. 4.47 shows a continuous decrease in b_* since 1850, in particular between 1850 and 1930 in the upper reaches of the river. Note also that in the lower reaches, b_* increases in upstream direction, whereas in the upper reaches b_* decreases in upstream direction (apart from the 1850-data). This difference in trend may have a similar cause as discontinuity in convergence length, discussed above.

It should be noted that, because of its definition with respect to the edges of the salt marshes, the values in b^* in Fig. 4.47 are likely to be an over-estimation of the actual values, which should be related to the river's width at mean high water. Moreover, it is likely that this over-estimation is larger in recent years, because of siltation on intertidal mud flats and subsequent development of vegetation owing to the high suspended sediment concentrations in the river. Visual inspection by the author of this report suggests that in 2012 a large part of intertidal area has been lost in favor of salt marshes.

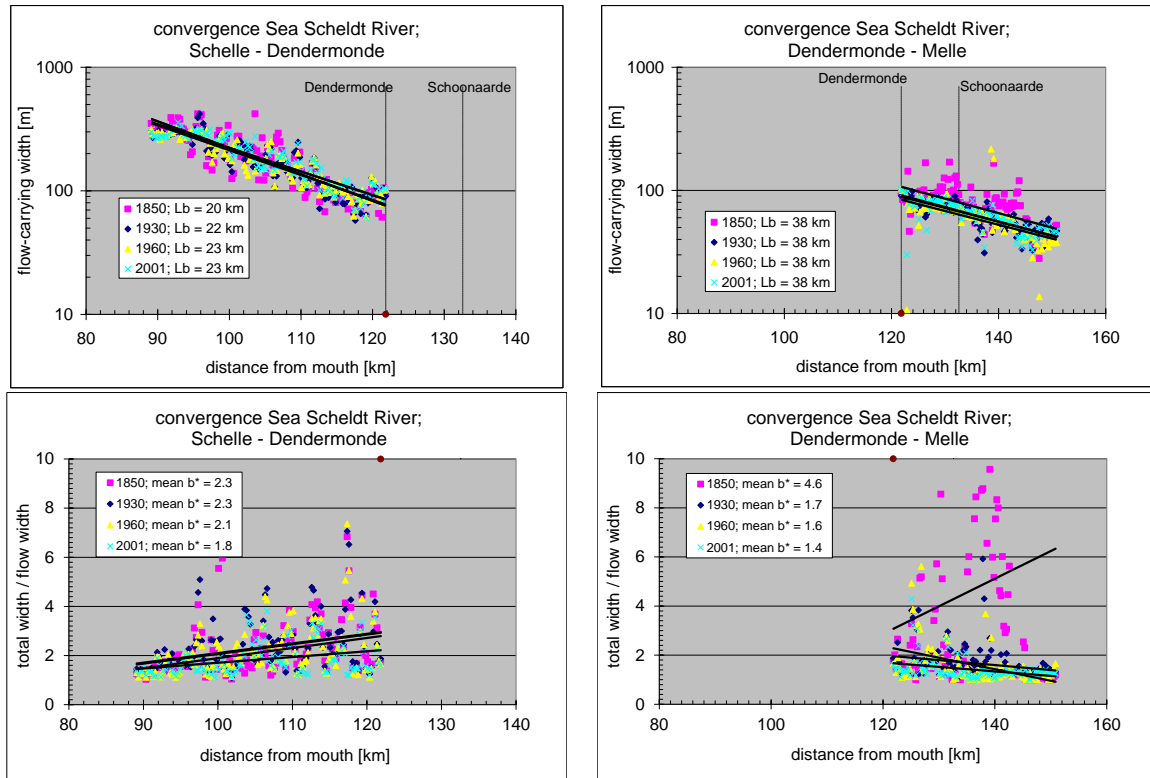


Fig. 4.47: Convergence length of flow carrying width (upper panel) and ratio total width over flow-carrying width (lower panel) of lower reach of Sea Scheldt (Schelle – Dendermonde) and upper reach (Dendermonde – Melle) since 1850.

Fig. 4.48 presents the imaginary wave number as derived from the measured tidal data of Fig. 4.41b, in which missing data points in the original data (e.g. Fig. 4.41a) have been added upon interpolation. Fig. 4.48 shows a number of important trends:

- From Schelle to halfway Dendermonde-Schoonaarde, the damping of the tidal wave increases (k ; more negative), and beyond ~km 125, the damping decreases again.
- In general, the damping along most part of the river has decreased over time.
- Close to Schelle, the tidal wave is no longer damped in the early 21st century.

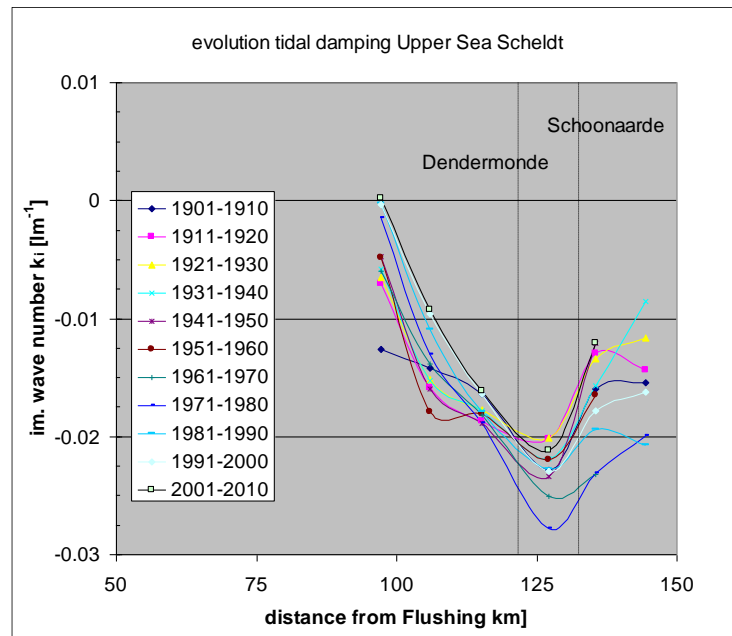


Fig. 4.48: Evolution of imaginary wave number along Upper Sea Scheldt, based on the data of Fig. 4.41b.

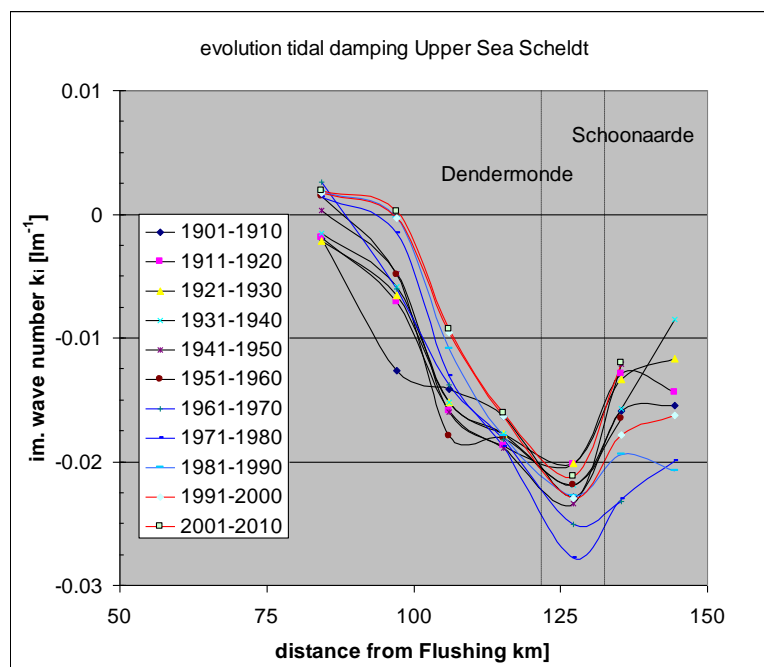


Fig. 4.49: Evolution of the imaginary wave number with time, and grouped for data from before 1960, after 2000, and in between. Time-mean values of data <1960 (black lines) yield $k_{i,old}$

Fig. 4.43 shows a profound deepening of the Upper Sea Scheldt between 1960 and 2001 (other information suggests that this happened between 1960 and 1970). Therefore, the evolution of the imaginary wave number k_i has been replotted in Fig. 4.49, where the data have been grouped in series before 1960 (black lines), after 2000 (red lines, and in between. Up to

Dendermonde/Schoonaarde, k_i has increased with $\sim 0.005 \text{ km}^{-1}$, further up-estuary, the trends are less obvious.

Next, the imaginary wave number before 1960 has been averaged over time, yielding a time-mean variation of k_i with distance, referred to as $k_{i,old}$. Let us next assume that the increase in tidal amplitude at Antwerp is due only to deepening/widening of the Western Scheldt and the Sea Scheldt in the vicinity of Antwerp, i.e. all river stretches down-estuary of Schelle. Then we can “predict” the tidal evolution up-estuary of Antwerp, using the measured evolution of the tidal range at Antwerp, and using $k_{i,old}$. This prognostic tidal evolution is presented in Fig. 4.50, in conjunction with the actual measured evolution, suggesting that the measured amplification from Schelle till Dendermonde/Schoonaarde should be ascribed for about 30% to down-estuary modifications of the Scheldt estuary, and for about 70% to changes in local bathymetry as discussed in Fig 4.43. The anomalous behavior up-estuary of Dendermonde/Schoonaarde is discussed below.

The change in longitudinal trend of the imaginary wave number beyond Dendermonde/Schoonaarde in Fig. 4.49 is remarkable. To explain this trend, we have computed the tidal amplitude over the river beyond Sint Amands without a weir and with a weir 8 km up-estuary of Melle. We have assumed a constant convergence length and a mean depth of 4.5 m. The results are presented in Fig. 4.51 in the form of the difference in imaginary wave number Δk_i between the configuration with and without weir, reproducing the reverse in trend of Fig. 4.49, and an increase by about 0.005 km^{-1} , which is about a factor two too small. Note that these results are not sensitive to the convergence length L_b , but highly sensitive to the water depth – the latter varies considerably over the last part of the river, whereas no information is available on the sections up-estuary of Melle. The results of Fig. 4.51 are therefore only indicative of effect of tidal reflections on the tidal evolution,

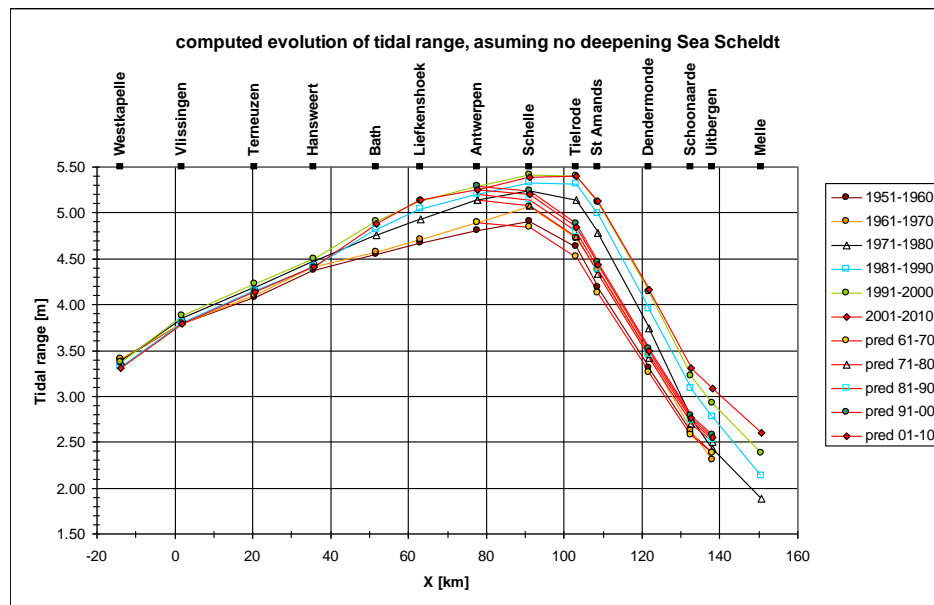


Fig. 4.50: Prognostic tidal evolution along the Upper Sea Scheldt, based on the lower values of the imaginary wave number of Fig. 4.49 (e.g. $k_{i,old}$).

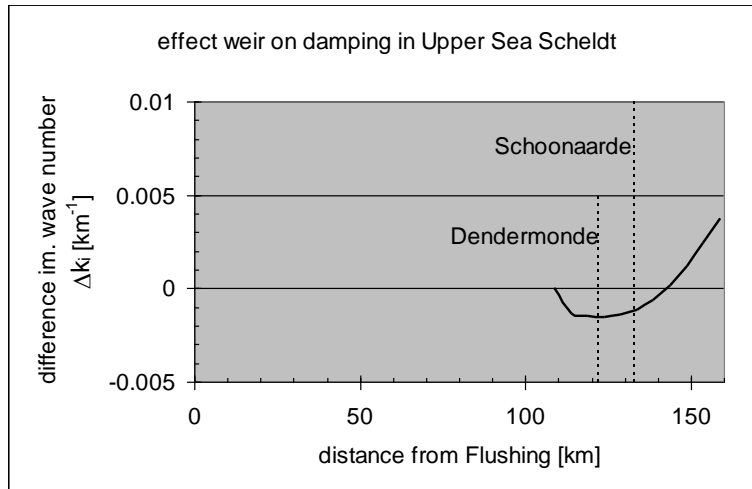


Fig. 4.51: Estimate of effect of weir on tidal damping in upper reaches of Upper Sea Scheldt.

Next, the imaginary wave numbers of Fig. 4.49 are made dimensionless with the convergence length of the Upper Sea Scheldt (e.g. equ. 8), where data up-estuary of Schoonaarde are omitted, as these are affected too much by tidal reflection. The dimensionless damping is plotted against the estuarine convergence number Λ_e in Fig. 4.52, showing a not too systematic trend with time. Data from before the large deepening in the Upper Sea Scheldt (<1960), data beyond 1990 and data in between have been marked with different colors. In particular, the data for the trajectory Dendermonde – Schoonaarde are a bit erratic (results not shown), most likely because of the effects of tidal reflection, and therefore not further included in our analysis.

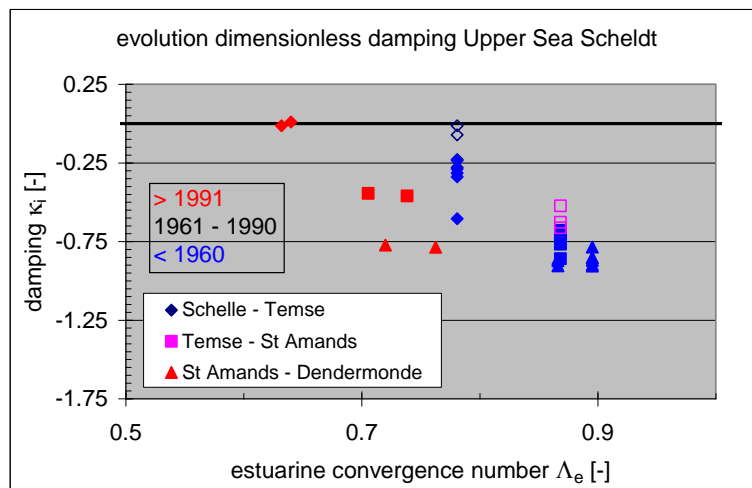


Fig. 4.52: Evolution of dimensionless imaginary wave number κ_i with variations in estuarine convergence number Λ_e .

Next, the linear model for an infinitely long tidal river (equ. 11) is fitted through the data by tuning the roughness parameter r_* , the results of which are presented in Fig. 4.53, showing variations in r_* from 9 to about 3.

To compute the effective hydraulic drag from the fitted r_* -values, we need to make an assumption on the flow velocity in the Upper Sea Scheldt. For this, we have used computational

results from the Delft3D model of the Western Scheldt, which show that the velocity amplitudes at Antwerp are about 10% larger than at Flushing, for the current bathymetry. We assume that the tidal velocities at Flushing have not changed much throughout the 20th century, and we assume further that the evolution of the tidal velocities along the Scheldt estuary over time follow the measured variations in tidal range, i.e. can be assessed from the imaginary wave number of Fig. 4.49. Then, by tuning r^* fitting equ. (11) through the dimensionless data, and using the estimated flow velocity and measured water depth, the effective Chézy coefficient can be established. The variation of C with time along the lower part of the Upper Sea Scheldt is presented in Fig. 4.54. All Chézy values are a bit low, which may be attributed to the fact that in the linear model many physical features in the river (bends, bed forms, bank irregularities, local variations in river topography and bathymetry, etc.) are missing. Also, estimates of the flow velocity are rather crude, though errors in this estimate occur only under the root of the solution to C (equ. 8).

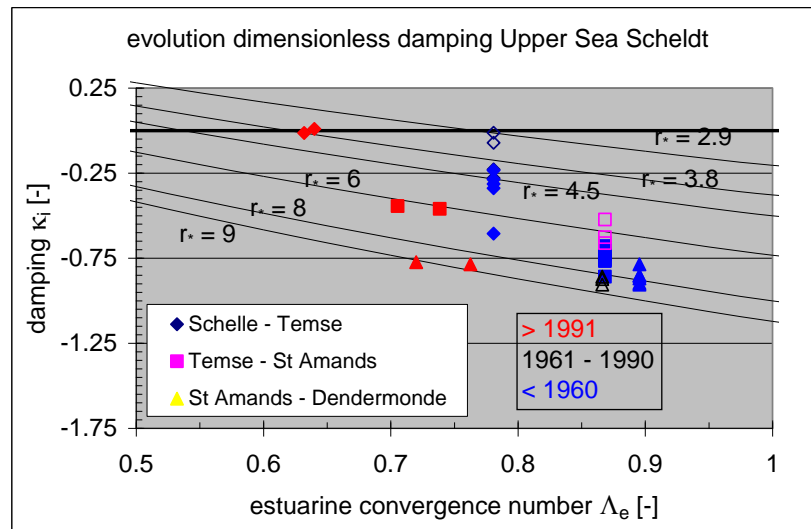


Fig. 4.53: Fits of linear solution trough observations tuning the roughness parameter r^* in the κ_i – Λ_e diagram.

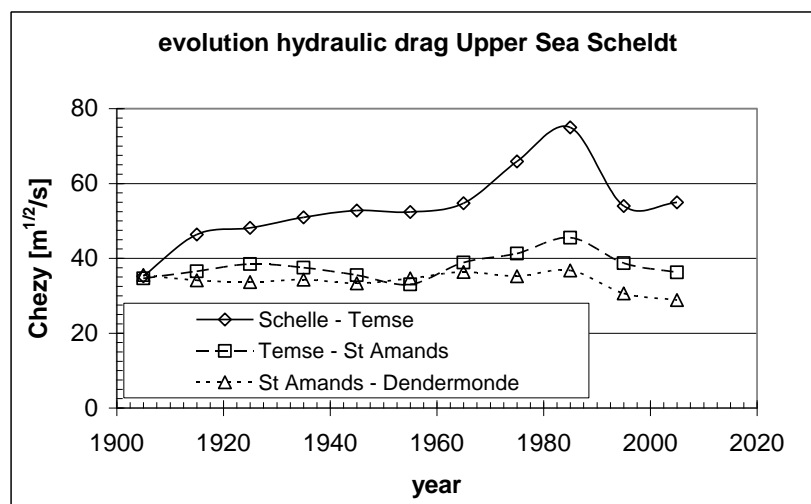


Fig. 4.54: Evolution of effective hydraulic drag (Chézy coefficient) with time,

Yet Fig. 4.54 suggests that the Chézy coefficient, hence effective hydraulic drag, did not change for the river stretch St Amands – Dendermonde, but increased considerably, in particular over the first part Schelle – Temse. If this reduction in drag would have been caused by high suspended sediment concentrations, this analysis suggests that values in SPM have been large for many decades, which, in conjunction with further deepening (e.g. Fig. 3.3) may explain the increase in C . The anomalous behavior between 1970 – 1990 is not understood, but may be misleading, as topographic/bathymetric data over that period is missing, and had to be manufactured by interpolation from other decades (see also bed level data of Fig. 4.43).

Fig. 4.55 presents measured data on tidal asymmetry, in the form of the ratio of the period of rising tide and falling tide, showing flood dominance over the entire river, Plancke et al. (2012). It is observed that flood dominance increases in upstream direction, as expected, as water depth decreases in upstream direction. We note that the river fresh water flow is relatively small, hence does only slightly affect the duration of flood and ebb period.

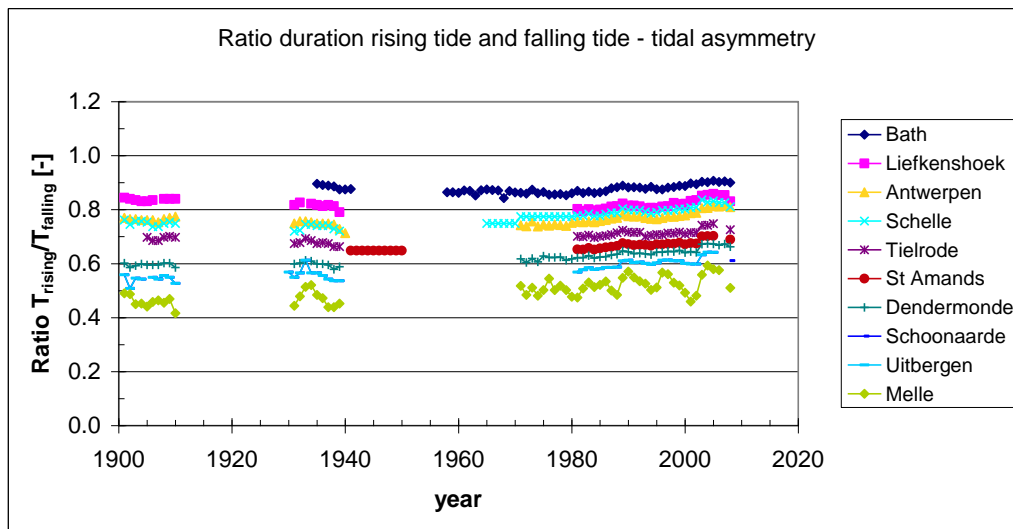


Fig. 4.55: Observed tidal asymmetry in Sea Scheldt.

However, it is remarkable that the asymmetry changes little over time, except may be for Schelle, given the large increase in tidal amplitude. This discrepancy can be explained from two developments:

1. In particular in the upper reaches, the water depth has increased largely in a relative sense. Larger water depth would decrease tidal asymmetry, counteracting the effects of a larger tidal range.
2. Probably more important is the development of tidal asymmetry in the Western Scheldt, e.g. Fig. 4.55, which serves as “boundary conditions” for the Upper Sea Scheldt. Hence, further to local generation of overtides in the Upper Sea Scheldt, tidal asymmetry is “imported” from the down-estuary reaches of the estuary, i.e. the Western Scheldt.

It is beyond the present study to evaluate the evolution of tidal asymmetry in the Western Scheldt, but the behavior of the asymmetry at Hansweert is remarkable, suggesting that its asymmetry tends to re-establish the conditions at the beginning of the 20th century.

5. Summary and conclusions

This report describes an analysis of the historical development of the tide in a number of European estuaries in relation to the human interventions (deepening, narrowing, rectifications, ...) carried out during the last century. The rationale behind this study is a fear that the Upper Sea Scheldt (Belgium, river stretch between Schelle and Ghent) may develop into a hyper-turbid system, such as the Ems and Loire rivers. This study is set up as follows:

1. Data of various tidal rivers have been collected. This was not always successful, and at the moment this report was written, more or less reliable/accurate data are available from the Ems, Elbe, Loire and Upper Sea Scheldt.
2. An analytical model has been derived, computing tidal propagation in estuaries.
3. This analytical model was then used to assess in a conceptual way the response of tidal rivers to human interventions.
4. Finally, that model has been used to analyze the measured historical development of the tide in the four rivers mentioned under 1.

This section summarizes the generic findings of this study, comparing the behavior of the various rivers; the conclusions with special focus on the Upper Sea Scheldt (Boven Zeeschelde) are given in the Dutch Samenvatting above.

In our analysis, two physical mechanisms are implicitly accounted for:

- I. The effective hydraulic drag in a (tidal) river decreases and the friction length increases when the water column becomes stratified. Such stratification occurs at depth-averaged concentrations of fine suspended sediment of a few 100 mg/l. Winterwerp et al. (2009) quantified this effect in a semi-analytical way. This work suggests that the increase in Chézy coefficient, for the rivers treated in this report, would amount to 15 – 30 m^{1/2}/s – this increase is linearly proportional with the absolute water depth.
- II. In an estuary, two turbidity maxima (ETM, estuarine turbidity maximum) may occur. The first maximum, ETM1, the classic one referred to in all text books on estuaries, is the result of a balance between river-induced flushing and up-estuary transport of fine sediment by estuarine circulation (induced by the longitudinal salinity gradients), and possibly some tidal asymmetry. This ETM1 is found in all “normal” estuaries near the estuary’s mouth at the head of the salinity intrusion.

However, a second may be formed further up-estuary, which is governed by a balance between river-induced flushing and up-estuary transport by tidal asymmetry (both peak velocities and vertical mixing, i.e. internal asymmetry).

As a result of large changes in the river (deepening, human interventions), such a second ETM2 can develop in a river previously characterized by an ETM1. Because ETM1 and ETM2 are driven by different physical processes, and because both ETM’s are fairly stable, we can refer to a regime shift when such a second ETM2 develops. These two regimes are sketched in Fig. 5.1.

The analytical model consists of the analytical solution of the one-dimensional shallow water equations, i.e. continuity and momentum equations, describing the water movement in tidal rivers. Note that the effects of river flow cannot be taken into account. These equations have been linearized by omitting within the momentum equation the advection term, and by making the friction term linear in the velocity. The solution to this set of equations is given in the form of a wave number as a function of the estuarine convergence number, introduced in this report, and the effective hydraulic drag. The wave number consists of a real part, reflecting the tidal wave length, and an imaginary part, reflecting the damping or amplification of the tide in the estuary. The plan form shape of the estuary (e.g. width, intertidal area), and its depth are given by the

estuarine convergence number. We assume that the width of the estuary converges in an exponential way, an assumption almost always met in alluvial estuaries. The solution of the analytical model is given in dimensionless numbers allowing mutual comparison of rivers of rather different size. The analytical solution describes the behavior of an incoming tidal wave, and its reflection, if relevant. In this study, the reflected wave is ignored in most cases, as the underlying equations cannot be solved anymore analytically in case of non-constant depths along the river. Note that an analytical solution is not possible either, when the water depth varies arbitrarily along the river.

We also determined the celerity of the tidal wave through the estuary, and the phase difference between water level and flow velocity, as well as a proxy for the tidal asymmetry from the analytical model. In the major part of the work we assume an infinitely long river, unless stated otherwise.

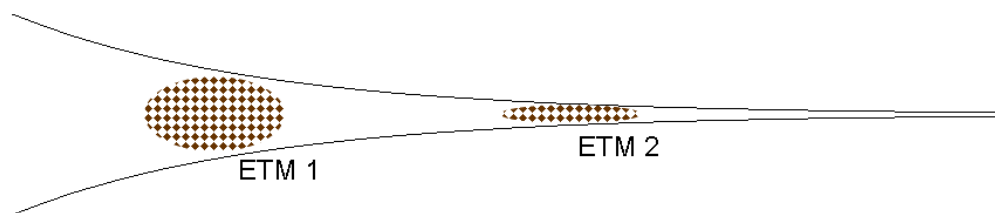


Fig. 5.1: Sketch of Estuarine Turbidity Maximum (ETM); ETM is characterized by a balance between river-induced flushing and estuarine circulation (and some tidal asymmetry), and ETM2 by a balance between the effects of river-induced flushing and tidal asymmetry.

The analytical model is used in two ways:

- I. Changes in tidal range (amplitude) and tidal asymmetry are computed as a function of hypothetical changes in the surface of intertidal area, the convergence length of the estuary, its depth, and the effective hydraulic drag. This provides a conceptual picture on the river's response to deepening and narrowing.
- II. The measured historical evolution in tidal range is evaluated and linked to the historical changes in the shape and bathymetry of the estuary:
 - For all time periods available, the damping/amplification of the tide along a stretch of the river, bordered by two neighboring tidal stations, is computed in the form of the (dimensionless) imaginary wave number.
 - The data on historical interventions in the rivers (deepening, narrowing, etc.) are summarized in the estuarine convergence number – this number increases with increasing water depth, increasing convergence of the river's plan form and decreasing intertidal area.
 - The historical development of the imaginary wave number is plotted against the evolution of the estuarine convergence number. Each data point in that diagram is obtained from actual observations, and represents one river stretch over a specific period of time.
 - The analytical model is fitted through these data points by tuning the roughness parameter of the model. Hence, the historical evolution in effective hydraulic roughness is established.
 - Finally, the historical changes in tidal asymmetry are assessed on the basis of actual observations or with the analytical model.

The response of a tidal river to deepening and narrowing, as computed with the analytical model, is presented in Fig. 5.2 and 5.10. It is assumed that the estuary is infinitely long, that the initial suspended sediment concentrations are low, and that the riverbed is sandy. Furthermore, it is assumed that intertidal areas are present along the entire length of the river – the width of the intertidal area equals the width of the flow-carrying section. The relative tidal amplitude at 60 km from the mouth increases monotonously with depth, as shown by the black line in Fig. 5.2.

Without intertidal area, for instance upon embanking or reclamation, the increase in tidal amplitude is somewhat larger, e.g. the blue line in Fig. 5.2.

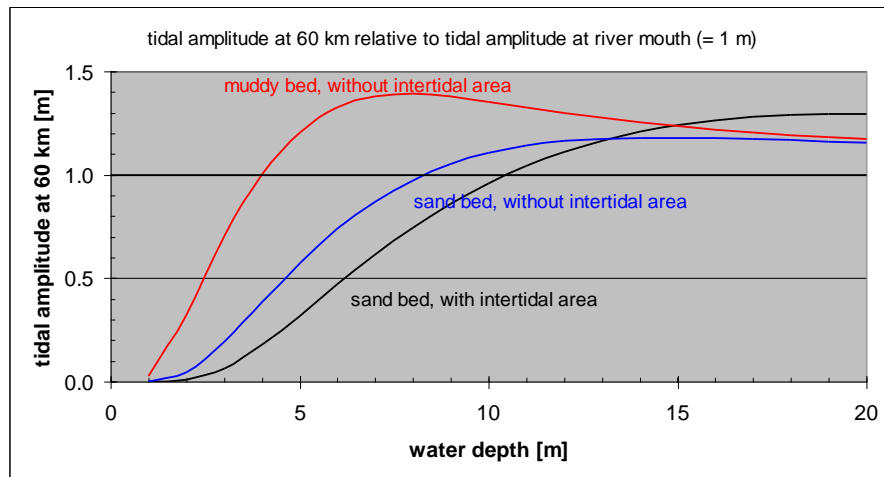


Fig. 5.2: Response of tidal amplitude as function of the presence of an intertidal area and mud in the water column, or on the River bed.

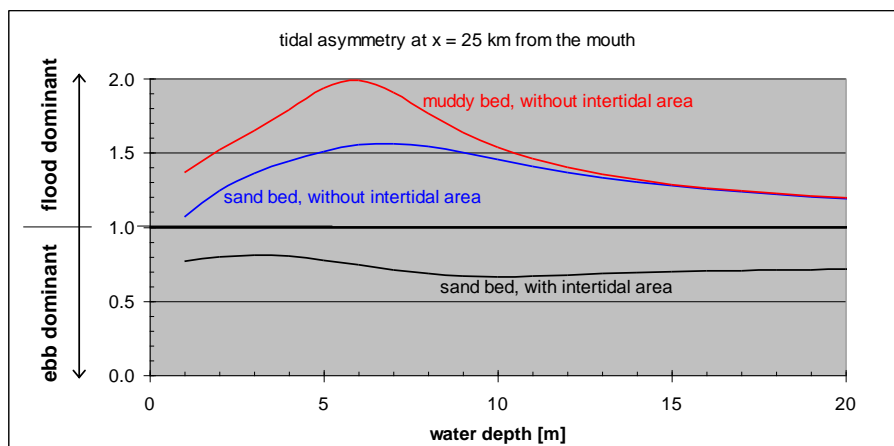


Fig. 5.3: Response of tidal asymmetry (γ -parameter) as function of the presence of an intertidal area and mud in the water column, or on the River bed.

A more important response of the river, however, is presented in Fig. 5.3. With intertidal area, the tide is always ebb-dominant, i.e. time-averaged transports of fine sediment are directed down-estuary (black line Fig. 5.3). Note that we do not address the role of a possibly externally generated tidal asymmetry. After loss of the intertidal area, the system becomes flood-dominant. This implies that mud is pumped into the estuary and/or that riverine mud accumulates within the estuary. Upon deepening, also the flushing capacity of the river decreases. The conditions for an

ETM2 (Fig. 5.1) are being created. With increasing suspended sediment concentration the effective hydraulic drag decreases (Chézy coefficient increases), in response of which the tide is further amplified (red line in Fig. 5.2). This then results in an increase in flood-dominance of the system (red line Fig. 5.3), enhancing suspended sediment concentrations and decreasing the effective hydraulic drag further. This positive feed-back loop induces a snowball effect.

This snowball effect is sketched in Fig. 5.4. One could argue that the loss of intertidal area has reduced the resilience of the river – with intertidal area, the tide will be amplified upon deepening of the river, but the system remains ebb-dominant, and the dangerous decrease in hydraulic drag is not initiated, and ETM2 conditions are not generated.

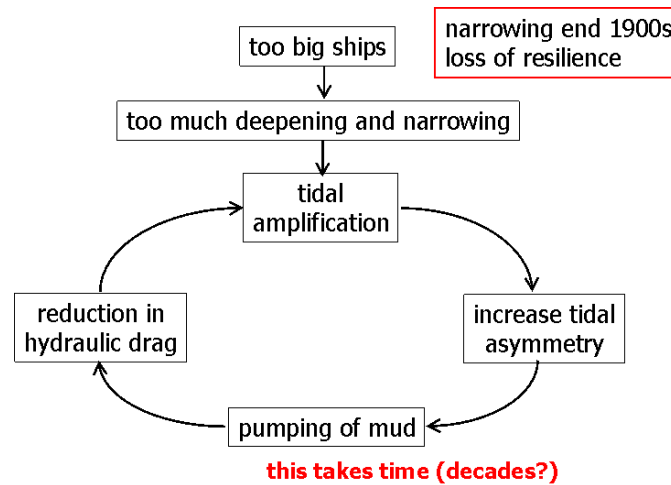


Fig. 5.4: The feed-back loop (snowball effect) for deepening of low-resilient estuaries.

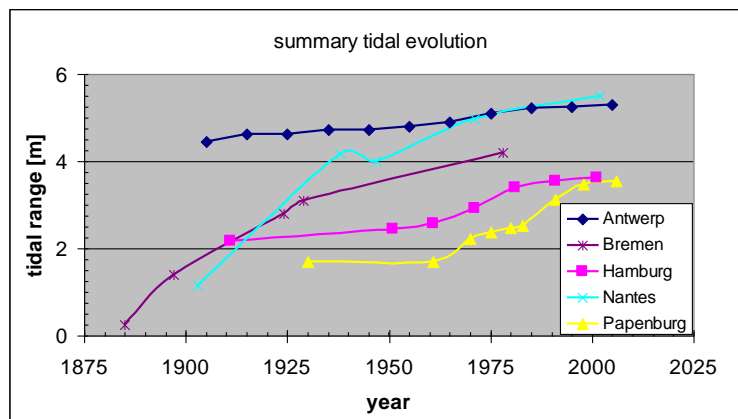


Fig. 5.5: Summary of tidal amplification in the 19th century in a number of European ports.

Whether ETM2 conditions actually will occur, and the time span over which this would happen, is dependent on the amount of fine sediment (mud) available. The time between the creation of “favorable” conditions and the actual occurrence of an ETM2 (hyper-turbid conditions) can be long, up to decades. The loss in intertidal area (loss of resilience) took place mainly in the late 19th and early 20th century throughout Europe, whereas profound deepening took place in the second half of the 20th century. The loss of intertidal area affects the resilience of the river in two ways:

1. Loss of intertidal area increases the tidal amplitude upon deepening and induces flood-dominant conditions (the latter effect is the more important),

- Loss of intertidal area causes a loss of accommodation space for the sedimentation of fine sediment – fine sediments brought into the system owing to the river’s flood-dominance can only remain within the water column, as a result of which the effective hydraulic roughness decreases, and the snowball effect of Fig. 5.4 can be initiated.

In this report the tidal evolution of four rivers has been analyzed, as these are the rivers from which sufficient (historic) data were available. This evolution can be summarized with the evolution of the tidal range at the major ports within these rivers – the accessibility of these ports has been the driving force behind the deepening. The results are presented in Fig. 5.5, showing increases in tidal range varying from 1 to 4 m. Note that all rivers have evolved to tidal conditions known as macro-tidal.

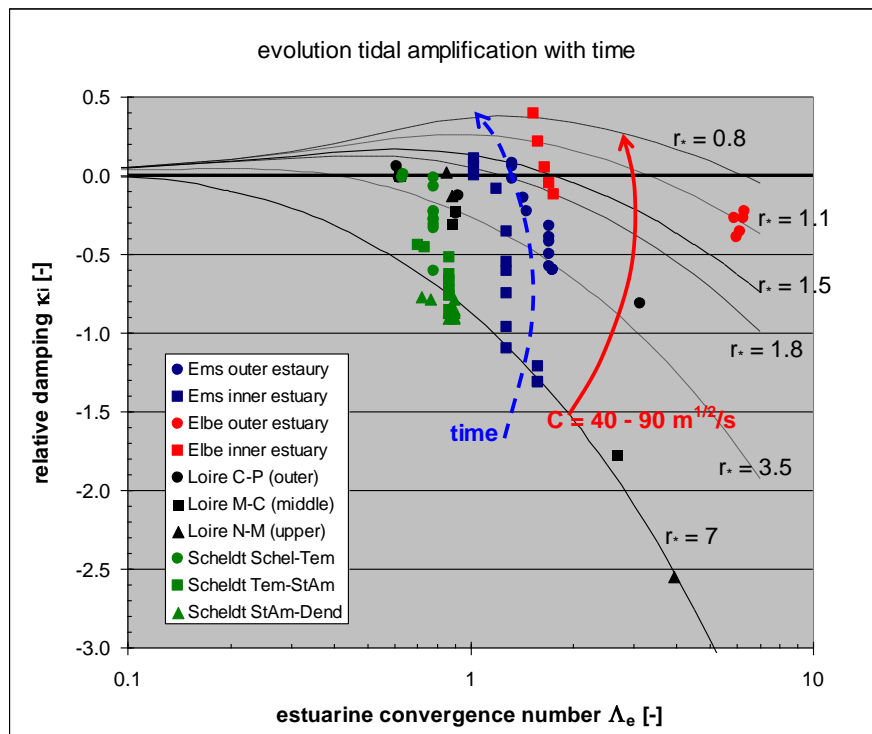


Fig. 5.6: Comparison of historic evolution of dimensionless damping coefficient and estuarine convergence number for four European rivers. Both time and Chézy coefficient follow a diagonal from the lower right to the upper left; $\kappa_i > 0$ implies amplification of the tide.

Fig. 5.6 summarizes the calibration of the analytical model by fitting the roughness parameter r^* through the various data points, presented in the dimensionless forms of the relative damping κ_i and the estuarine convergence number Λ_e . All rivers show an increase in r^* with time, i.e. when the rivers are more and more deepened.

This decrease in effective hydraulic drag is further illustrated with the evolution of the computed Chézy coefficient for the four rivers and the various reaches of the river which could be identified. This evolution is presented in Fig. 5.7, showing that the majority of the river reaches have experienced a considerable increase in Chézy coefficient, by about 15 – 30 $\text{m}^{1/2}/\text{s}$ – it is anticipated that the majority of this increase is due to increased levels of suspended sediment concentration. The larger increase has been established for the upper part of the Elbe River. This can be explained by the larger depth of that river, as predicted by the semi-analytical relation on

the dependency of the effective hydraulic drag on suspended fine sediment concentrations. The large Chézy-values found for the inner Elbe estuary are not related to high SPM-concentrations – these have not been measured in this part of the river. However, our analysis suggests that the inner Elbe is close to resonance conditions, hence very sensitive to small changes in bathymetry. This resonance cannot be accounted for by the analytical model. Hence the tidal amplification induced by resonance is captured by a very low friction coefficient, which therefore is likely to be erroneous.

It is noted that all rivers show profound flood-dominant conditions – this follows from both the analytical model, as from observations on flow velocities and/or the duration of rising vs falling tide.

The computed increase in Chézy coefficient has been summarized in Fig. 5.15, together with some data made available by prof. Townend (Thames, Mersey and Severn) and data from the Gironde (Villaret et al., 2011) and the Western Scheldt ((Kuijper and Lescinski, 2012). From the red data points we know that the river experiences serious problems with high concentrations of fine sediment, whereas no excess Chézy values have been established for the green points – here the river still behaves “normal”. Fig. 5.15 suggests that a diagonal line can be drawn in that graph representing the tipping point/zone for the establishment of hyper-turbid conditions. However, unless this shift in behavior is further supported by additional data and/or research, the reddish line in Fig. 5.15 remains fairly speculative. Prandle (2003) found a similar decrease in friction factor for muddy systems, but he related the friction coefficient f to the mud content of the bed; data in his paper are incomplete to add to the current analysis.

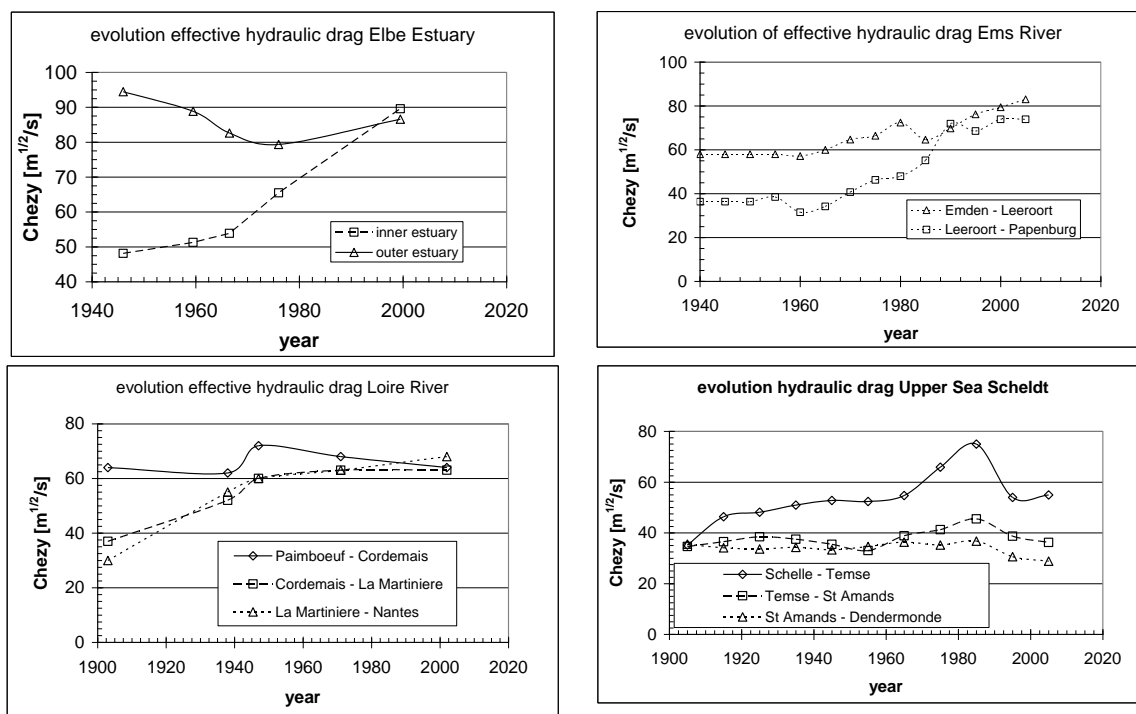


Fig. 5.7: Summary of evolution of computed Chézy coefficient with time for four European rivers.

We have not yet been able to quantify the tipping point for the response of the estuaries to human interventions, e.g. narrowing and deepening. However, a change in effective hydraulic drag may be a useful indicator. This drag can be obtained from an analysis of tidal data, as in this report, or

from the use of numerical hydraulic models, in which the (effective) roughness coefficient is tuned in the calibration of the model.

Fig. 5.8 suggests that this is indeed a versatile way forward, but currently we have four data point only, if we assume that the Ems, Loire and Elbe river have passed the tipping point, and the Upper Sea Scheldt not.

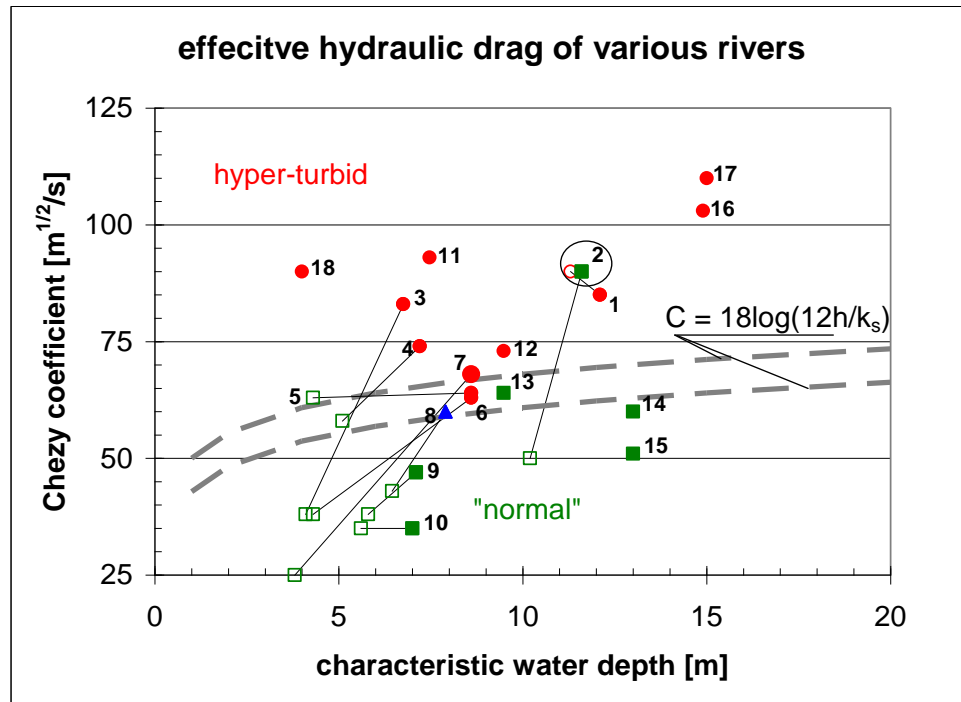


Fig. 5.8: Comparison of effective hydraulic drag in some rivers as a function of water depth. The C - h relation is based on $k_s = 2$ and 5 cm, arbitrary values. Red symbols depict hyper-turbid conditions, green symbols "normal conditions, and blue symbols possibly transitional systems; open symbols reflect historical data. 1: Elbe-outer; 2: Elbe-inner; 3: Ems/E-L; 4: Ems/L-P; 5: Loire/P-C; 6: Loire/C-laM; 7: Loire/LaM-N; 8: Scheldt/S-T; 9: Scheldt/T-StA; 10: Scheldt/StA-D; 11: Thames; 12: Severn-inner; 13: Severn-outer; 14: Western Scheldt; 15: Gironde-outer; 16: Gironde-inner (Villaret et al., 2011); 17: Yangtze estuary; 18: Vilaine (Vested et al., 2013). Note that data on Elbe-inner may be spurious because of tidal reflections, as discussed in Section 2. Furthermore it is presumed that the turbidity maximum in the Loire River used to be located in the outer Loire (pt 5).

This argument is further sustained by Table 5.1 in which a series of natural macro-tidal estuaries and heavily engineered systems are given. This table suggests that macro-tidal conditions and abundant availability of fine sediments are necessary conditions for initiation of the regime shifts described above. It seems therefore useful to gather data on the (effective) hydraulic drag of the rivers in Table 5.1, and add these to Fig. 5.8.

A final observation relates to the effects of climate change. With increasing sea level, water depths increase, which induce similar effects as a deepening of the river. However, the major impact is most likely a further squeezing of the river, reducing intertidal areas further, thereby reducing the resilience of the system.

Table 5.1: Comparison of natural, macro-tidal rivers with (very) high suspended sediment concentrations and heavily engineered estuaries. This table suggests that by engineering estuaries too much, their regime is shifted from the left column to the right column.

deepened and narrowed		natural macro-tidal rivers	
Ems (Germany)	+++	Amazon mouth (Brazil)	+++
Elbe (Germany)	++	Alligator River (Australia)	++
Garonne (France)	++	Bay of Fundy (Canada)	+++
Loire (France)	+++	Bay Saint Malo (France)	+++
Ouse (UK)	++	Jiaojiang River (China)	++
Seine (France)	+ / ++	Mersey (UK)	+++
Trent (UK)	++	Severn River (UK)	+++
Vilaine (France)	++		
Weser (Germany)	+ / ++		
Western Schelde	+		
Upper Sea Scheldt	++		

+++ hyper-turbid conditions
+ “normal” estuarine conditions

6. Recommendations

The analysis of historical data of four rivers with a linear, analytical model has revealed a profound positive feed-back between the tidal properties and suspended fine sediment. This analysis also suggest the existence of a tipping point, beyond which a tidal river evolves more or less autonomously to a hyper-turbid state – such a tipping point could be passed upon extensive engineering works (deepening, narrowing, ...) in a tidal river. However, this tipping point could not be quantified, nor was it possible to define indicators identifying the passage of a tipping point. Possibly this tipping point can be identified from a thorough stability analysis of the governing equations. This, however, requires a major study, and for the time being we propose to try and quantify the tipping point in a more empirical way. For that, the following activities are required:

1. Collect historical tidal data from more rivers, preferably in a variety of states, i.e. from hyper-turbid to “normal”. These data should be analyzed in a way similar to the method followed in the current report. Moreover, the analysis of the Loire can be improved if more accurate data become available.
2. The analysis in the current report should be confronted with (historical) data on suspended sediment concentration and/or maintenance dredging volumes to substantiate the conclusions on mud-induced decreases in effective hydraulic drag.
3. Collect data/numbers from numerical models calibrated to simulate the tidal propagation in large tidal rivers properly. Unexpectedly low values for the effective hydraulic drag may indicate large suspended sediment concentrations. The calibrated values of the roughness values can be added to our diagram on excess Chézy values to substantiate that diagram further.
4. The amplification in some of the rivers in general, and within the upper part of the Elbe river (up to Hamburg) seem to be affected considerably by wave reflections and/or resonance. Because of the large effect of tidal amplification on tidal asymmetry, hence on the fine sediment dynamics, it is recommended to study the reflections of tidal waves in these estuaries further.
5. Set up numerical hydrodynamic models of the various rivers – it is anticipated that one-dimensional models (SOBEK) are sufficient for the analyses required:
 - The effects of longitudinal variations in bathymetry (depth, intertidal area) can be studied in a more realistic way.
 - The effect of the construction of weirs cannot be studied properly with the analytical model, but is easily addressed with a numerical model.
 - The effects of river flow cannot be studied with the analytical model, but is easily addressed with a numerical model.
 - A numerical model will also provide more sound information on the tidal asymmetry, whereas with the analytical model, only a proxi can be established.

The computational results from the one-dimensional model can be analyzed in the same way as in the current report, tuning the effective roughness coefficient to calibrate the model.

6. Both the analytical and numerical model can be used, assessing the efficiency of mitigating measures, such as those suggested for the Scheldt River.
7. It is recommended to study the causes of the deepening of the Upper Sea Scheldt in the 1970's – this should be done with a morphodynamic model, including Lower Sea Scheldt, and possibly (part of) the Western Scheldt.

Acknowledgements

This work was carried within the framework of the LTV-project, which is the acronym for Long-Term Vision of Scheldt estuary with respect to Safety, Accessibility and Nature, in which the following sub-projects are integrated: Maintaining fairways Scheldt estuary, Permits for disposal of dredged sediments and the so-called KPP (knowledge of primary processes) program of Rijkswaterstaat. The study was financed by the Flemish “Afdeling Maritieme Toegang” and the Dutch Ministry of Infrastructure and Environment, Rijkswaterstaat, Waterdienst and Directorate Zeeland.

The results in this report are based on a large number of data from a variety of sources. Some data sets were available at Deltares in reports, or in digital form from studies carried out earlier. Other data have been prepared and made available especially for this project. I would like to thank the following people for their support and supply of data: Dr. Alexander van Braeckel (INBO, Brussels), ir. Gijsbert van Holland (IMDC) and Frederik Roose (Flemish Government) for Scheldt data, Dr Frank Kösters (BAW Hamburg) for data on the Ems, Elbe and Weser rivers, dr. Luc Hamm (Sogreah) for data on the Loire, and dr. Harro Heijer, Dr. Frank Koesters and dr. Jens Jürgens (BAW) for data on the Ems, Weser and Elbe river; and Prof. Ian Townend for data on the Thames and Severn estuaries.

I would like to thank the reviewers dr. Henk Schuttelaars (Delft University of Technology) and prof. dr. Tom de Mulder (University of Ghent, Belgium).

References

- BAW, 2012. Data received from Dr. Frank Koesters and dr. Jens Jürgens on Ems and Elbe.
- Boelich M.J. and T. Strotmann, 2008. The Elbe estuary. Source unknown.
- Briere, C., J. Crebas, A. Becker and J.C. Winterwerp, 2012. Analyse de la morphologie du chenal de Nantes et étude de sa restauration - Phase 3 : Etude de l'impact d'une intervention à l'amont de Nantes sur les caractéristiques de la marée. Deltares report 1201695 (in French).
- Bruens, A.W., J.C. Winterwerp, C. Kranenburg, 2012. "Physical and numerical modeling of the entrainment by a high-concentrated mud suspension", ASCE, Journal of Hydraulic Engineering, in press, doi:10.1061/(ASCE)HY.1943-7900.0000545.
- Chandramohan, P.V., 1989. Density currents and siltation – with particular reference to Cochin. IHE, Master Thesis, Delft, The Netherlands.
- Deltares, 2011. Analyse de la morphologie du chenal de Nantes et étude de sa restauration - Phase 1 : Evolutions passées et fonctionnement actuel. Report 1201695-001.
- Dankers, P.J.T., J.C. Winterwerp, 2007. "Hindered settling of mud flocs: Theory and validation. Continental Shelf Research, 27, 1893-1907.
- Dronkers, J. (1986). Tide-induced residual transport of fine sediments. In Van de Kreeke, J.: Physics of Shallow Estuaries and Bays, 228-244, Springer, Berlin.
- Dronkers, J., 2005. Dynamics of coastal systems. Advanced Series on Ocean Engineering – Vol 25. World Scientific.
- Dyer, K. R. 1997, Estuaries: a physical introduction. Chichester, England. John Wiley and Sons.
- Friedrichs, C., 2010. Barotropic tides in channelized estuaries. in A. Valle Levinson, Contemporary Issues in Estuarine Physics. Cambridge University Press, 27 – 61.
- Haar, T., 1994. Wirkung der Stromungsumlenkwand am Kohl fleet. Strom- und Hafengebäude, Hamburg, Gewässerkundlich Studie Nr. 13.
- Jay, D.A. and Musiak, J.D., 1996. Internal tide asymmetry in channels: origins and consequences. In: Pattiaratchi C (ed) Mixing processes in estuaries and coastal seas. American and Geophysical Union Coastal and Estuarine Sciences Monograph, 219-258.
- Herrling, G., 2007. Changes of the Hydrodynamic Regime due to Historical Pressures on Estuarine Geomorphology; the Example of the Ems-Dollard Estuary. Research project: INTERREG IIB North Sea project HARBASINS; Work package 4: „Hydro-morphological impacts and pressures“ Lower Saxony Water Management, Coastal Defense and Nature Conservation Agency, Coastal Research station.
- IMDC, 2012. Analyse bodemgegevens Boven Zeeschelde. Note I/NO/11387/12.226/VBA.
- Kappenberg, J. and H.-U. Fanger, 2007. Sedimenttransportgeschehen in der tidebeeinflussten Elbe, der Deutschen Bucht und in der Nordsee. GKSS-Forschungszentrum Geesthacht GmbH – Geesthacht, Report 2007/20.
- Krebs M. and H. Weilbeer, 2005. Ems-Dollard Estuary. Die Küste 74, 252-262.
- Kuijper, K. and J. Lescinski, 2012. LTV O&M thema veiligheid (theme safety) – sub project 1: data analyses and hypotheses Western Scheldt. Deltares report 1204405.
- Nasner, H., 1974. Über das Verhalten von Transportkörpern im Tidegebiet. Mitteilungen Franzius Institut, Heft 40. Hannover, Germany.
- Kuijper, Kees, Jamie Lescinski, 2012, LTV Veiligheid en Toegankelijkheid. Sub project B: Data analysis Western Scheldt. Report 1204405. Deltares.
- Plancke, Y., T. Maximova, S. Ides, P. Peeters, E. Taverniers, F. Mostaert, 2012, Werkgroep O&M - Projectgroep Veiligheid. Sub project 1: Data analysis and hypothesis - Upper Sea Scheldt. Report WL2012R756_05_rev4_0. Flanders Hydraulics Research.
- Prandle, D., 2003. Relationships between Tidal Dynamics and Bathymetry in Strongly Convergent Estuaries. Journal of Physical Oceanography, 33, pp 2738-2750.
- Prandle, D., 2004. How tides and river flows determine estuarine bathymetries. Progress in Oceanography, 61, 1–26.

- Postma, H., 1961. Transport and accumulation of suspended matter in the Dutch Wadden Sea. *Netherlands Journal of Sea Research* 1, 148-190.
- Schijf, J.B. and J.C. Schönfeld, 1953. Theoretical considerations on the motion of salt and fresh water. *Proceedings Minnesota International Hydraulics Convention*. Minnesota.
- Schrottke, K. and Bartholomä, A., 2008. Detaillierte Einblicke in die ästuarine Schwebstoffdynamik mittels hochauflösender Hydroakustik. Tagungsband zum Seminar Ultraschall in der Hydrometrie: neue Technik; neuer Nutzen; FgHW / DWA, Koblenz, June 2008, 75-82.
- Schuchardt, B. and S. Beilfuss, 2012. Sediment management strategies in the Weser estuary. Bio Consult, report 08.10.2012, prepared for NLWKN Oldenburg.
- Sogreah, 2006. Expertise et connaissance du système estuarien de Loire – Tome 1: Analyse historique, Report 1711457R2 (in French).
- Talke, S.A., De Swart, H.E. and De Jonge, V.N., 2009. An idealized model and systematic process study on oxygen depletion in highly turbid estuaries. *Estuaries and coasts*, 32 (4), 602-620.
- Van Braeckel, A., Piesschaert, F. en van den Bergh, E., 2006. Historische analyse van de Zeeschelde en haar getijgebonden zijrivieren. 19e eeuw tot heden. INBO report INBO.R.2006.29
- Van Rijn, L.C., 1990. Principles of sediment transport in Rivers, Estuaries and Coastal Seas. Aqua Publications.
- Van Rijn, L.C., 2011. Comparison hydrodynamics and salinity of tide estuaries; Elbe, Humber, Schelde and Weser. *Deltares Report* 1203583-000.
- Van Straaten, L.M.J.U. and Ph. H. Kuenen, 1958. Tidal action as a cause of clay accumulation. *Journal of Sedimentary Petrology*, 28 (4) 406-413.
- Van Straaten, L.M.J.U. and Ph. H. Kuenen, 1957. Accumulation of fine grained sediments in the Dutch Wadden Sea. *Geologie en mijnbouw* 19, 329-354.
- Villaret, C., N. Huybrechts, A.G. Davies and O. Way, 2011. Effect of bed roughness prediction on morphodynamic modelling: Application to the Dee estuary (UK) and to the Gironde estuary (France). 34th IAHR World Congress, Brisbane, Australia, pp 1149-1156, ISBN 978-0-85825-868-6,
- Vroom, J., H. van den Boogaard and B. van Maren, 2012. Mud dynamics in the Eems-Dollard, research phase 2 – Analysis of existing data. *Deltares, report* 1205711-001.
- Weilbeer H. and M. Klöpffer, Bundesanstalt für Wasserbau, 2011. Model Validation and System Studies for Hydrodynamics, Salt and Sediment Transport in the Elbe Estuary - Basic Information for the River Engineering and Sediment Management. Draft Report A39550310069.
- Weilbeer, H., 2013. Personal communication.
- Winterwerp, J.C., 2001. Stratification effects by cohesive and non-cohesive sediment. *Journal of Geophysical Research*, 106 (C10) 22559-22574.
- Winterwerp, J.C., 2002. Scaling parameters for high-concentrated mud suspensions. in: Elsevier, *Proceedings in Marine Science*, No 5; Proceedings of the 6th International Conference on Nearshore and Estuarine Cohesive Sediment Transport, INTERCOH-2000, ed. J.C. Winterwerp & C. Kranenburg, 171-186.
- Winterwerp, J.C., Z.B. Wang, T. van der Kaaij, K. Verelst, A.C. Bijnsma, Y. Meersschaut, M. Sas, 2006. Secondary currents by weak salinity gradients in estuaries. *Ocean Dynamics*, 56, 284-294.
- Winterwerp, J.C., 2006. Stratification effects by fine suspended sediment at low, medium and very high concentrations. *Geophysical Research*, 111 (C05012) 1-11.
- Winterwerp, J.C., M. Lely and Qing He, 2009. Sediment-induced buoyancy destruction and drag reduction in estuaries. *Ocean Dynamics*, 59 (5) 781-791.

Winterwerp, J.C., 2011. Fine sediment transport by tidal asymmetry in the high-concentrated Ems River. *Ocean Dynamics*, 61 (2-3) 203-216, DOI:10.1007/s10236-010-0332-0.

De eventuele referentie naar het data-analyserapport voor de Beneden-Zeeschelde is:
Wasser- und Schifffahrtverwaltung des Bundes. Zentrales Datenmanagement der WSD Nord - Portal Tideelbe, 1999; see also http://www.portaltideelbe.de/Projekte/FRA1999/-Beweissicherung/Ergebnispraesentation/profile_elbe/index.html.

Nomenclature

symbol	unit	description
A_c	m^2	flow-carrying cross section
a	m	tidal amplitude
a_0	m	tidal amplitude in river mouth
a^+	m	tidal amplitude of incoming wave
a^-	m	tidal amplitude of reflecting wave
b	m	river width
b_c	m	width flow-carrying cross section
b_t	m	total width
b^*	m	dimensionless width (equ. 8)
Δb	m	width intertidal area
C	$m^{1/2}/s$	(effective) Chézy coefficient
C_0	$m^{1/2}/s$	Chézy coefficient for neutral conditions
C_{SPM}	$m^{1/2}/s$	Chézy coefficient induced by suspended fine sediment
c	m/s	wave celerity
c	kg/m^3	mass concentrations suspended sediment
c_D	-	drag coefficient
F	kg/m	total fine sediment transport rate per unit width, integrated over tidal period
F_a	kg/m	F by tidal asymmetry
F_g	kg/m	F by estuarine (gravitational) circulation
F_l	kg/m	F by lag effects (scour lag and settling lag)
F_p	kg/m	F by tidal pumping – in this report referred to as F_a
F_r	kg/m	F by residual flow (river flow and Stokes' rectification)
F_s	kg/m	F by Stokes' drift
F_v	kg/m	F by asymmetry in vertical mixing (internal asymmetry)
g	m/s^2	gravitational acceleration
h	m	water depth (mean water level – bed level)
k	m^{-1}	wave number: $k = k_r + i k_i$
k_r	m^{-1}	real wave number: $k_r = 2\pi/\lambda$
k_i	m^{-1}	imaginary wave number
L_b	m	estuarine convergence length
L^*	m	non-dimensional estuarine convergence length (equ. 8)
P	kg/ms	production/erosion of fine sediment per unit width
Ri_f	-	flux Richardson number
Ri^*	-	bulk Richardson number
r	m/s	linear friction coefficient
r^*	-	non-dimensional linear friction coefficient (equ. 8)
S	kg/ms	sedimentation of fine sediment per unit width
t		time
T		tidal period
U	m/s	amplitude flow velocity
U_0	m/s	amplitude flow velocity in river mouth

U^+	m/s	amplitude flow velocity of incoming wave
U^-	m/s	amplitude flow velocity of reflecting wave
u	m/s	flow velocity
u_*	m/s	shear velocity
x	m	longitudinal coordinate (positive up-estuary)
β	-	Rouse number
Γ	-	dimensionless parameter in tidal asymmetry proxi (equ. 20a)
γ	-	proxi for tidal asymmetry
η	m	instantaneous water level
κ	-	dimensionless complex wave number: $\kappa = \kappa_r + i \kappa_i$ (equ. 8)
κ_r	-	dimensionless real wave number
κ_i	-	dimensionless imaginary wave number
κ^+	-	dimensionless complex wave number incoming wave
κ^-	-	dimensionless complex wave number reflecting wave
Λ_e	-	(dimensionless) estuarine convergence number (equ. 8)
l	m	length of estuary in case of weir
λ	m	length tidal wave
ω	s ⁻¹	tidal frequency: $\omega = 2\pi/T$
ϕ	rad	phase angle between tidal water level and flow velocity
